Three-dimensional Acoustic Scattering from Arctic Ice Protuberances

Tarun K. Kapoor

B.S., Naval Architecture, I.I.T., Madras (1989)

Submitted to the Department of Ocean Engineering
in partial fulfillment of the requirements for the degree of

Doctor of Philosophy

at the

Massachusetts Institute of Technology

June 1995

Author .....
Department of Ocean Engineering
May 5, 1995

Certified by .....
Professor Henrik Schmidt
Department of Ocean Engineering
Thesis Supervisor

Accepted by .....
Professor A. Douglas Carmichael
Chairman, Departmental Graduate Committee

Three-dimensional Acoustic Scattering from Arctic Ice Protuberances

Tarun K. Kapoor

Submitted to the Department of Ocean Engineering on May 5, 1995,
in partial fulfillment of the requirements for the degree of
Doctor of Philosophy

Abstract

This thesis investigates the three-dimensional mid-frequency ($ka \sim O(1)$) acoustic scatter from large-scale features under the Arctic ice cover using an analytical model and experimental data. A theoretical model is developed which contains all the relevant physics of three-dimensional scatter. I derive the analytical solution for scattering from a sphere attached to a thin, infinite, fluid-loaded elastic plate. This idealized environmental model provides an understanding of the underlying physics of 3D scattering, and is shown to be strongly frequency dependent. The analysis demonstrates that the attachment of the plate to the sphere manifests itself in the scattered field in a frequency selective manner. Moreover, it is also shown that the relative amplitudes of excitation of flexural and in-plane (compressional and shear) modes in the ice plate depend on both frequency and angle of incidence of the acoustic field.

Using the results from my theoretical investigation, I evaluate the scattering characteristics of discrete large-scale features, or "hot spots", under the ice by analyzing field data from CEAREX89 reverberation experiments. This analysis involves the identification and isolation of protuberances under the ice, and subsequent evaluation of their spatial scattering characteristics. I use a two-step Matched Field Processing algorithm to solve this complex multi-parameter estimation problem. Using adaptive array processing techniques, I obtain high resolution reverberation estimates. This study also re-emphasizes the frequency selectivity of 3D scatter.

Finally, I compare results from the experimental investigations and the analytical model. Comparisons in scattering levels between these two studies were not possible since the experimental data consists of contributions from multiple scatterers. This was primarily due to the available experimental geometry. For certain frequency bands, where scatter from a distinct feature is very prominent, there is some qualitative agreement between analytical predictions and experimental data. However, within the enclaves of the available data, it was not possible to conclusively corroborate theoretical solutions with field data.

Thesis Supervisor : Henrik Schmidt
Title : Professor, Department of Ocean Engineering

Acknowledgments

First of all, I would like to thank my advisor Henrik for his indefatigable support and encouragement. You were always very helpful and found time to discuss matters related to research, right down to the basic issues. I enjoyed the informal structure of our student-advisor rapport, and the very approachable nature of your working style. Your constant excitement and interest in my work kept me motivated to produce my best. You were available for guidance whenever the need arose. Henrik, you possess all the qualities of an ideal graduate student advisor. I was fortunate to have you as my advisor, and I am sure I must have been regarded with envy by others.

Secondly, I would like to express my gratitude to the members of my Committee - Rob Fricke, Tim Stanton and Yueping Guo, for meticulously going over the draft of my thesis and providing invaluable suggestions. Rob, I wish you the best in securing a tenured position at MIT. You are a great teacher and I thoroughly enjoyed your style of lecturing. I am also particularly indebted to Yueping for the numerous discussions on issues related to theoretical modeling. You were always available for talking things over whenever I had some questions. It was great having you around, and I am sure the graduate students are going to miss you. I wish you the best in your future endeavors, and hope you have fun with your family in California.

I am grateful to the Office of Naval Research for funding this research program. I would also like to express my sincere appreciation to Prof. Ira Dyer for providing me with a Research Assistantship for the first three years of my study at MIT. I would also like to acknowledge the support of Prof. Wierzbicki for taking me on as a Teaching Assistant for two semesters. It was an enjoyable experience teaching Structural Mechanics. I was fortunate to have had the opportunity of working with Prof. Leo Felsen during my early years at MIT. Leo, I learnt a lot from you, and you helped me develop an appreciation for analytical methods.

There are numerous people to whom I am obligated because of their association with the CEAREX experiments. I would like to express my thanks to Prof. Baggeroer

(Chief Scientist, CEAREX89) and Keith von der Heydt of Woods Hole. I am also very grateful to Eddie Scheer of WHOI for his tremendous help in acquiring the data from the optical disks. He was always available at very short notice. I am also appreciative of the efforts of Tom Hayward of NRL for providing me with the reverberation data from the vertical line arrays. I am greatly indebted to Marilyn, Denise, Sabina, Taci and Isela for taking care of everything. Sabina, I cannot imagine what the Acoustics group would do without you. You are so concerned about the students and are always looking out for them. It is no surprise that everyone likes you so much.

I will fondly cherish the memories of the time spent in the office upstairs. The folks of 5-435 made work an enjoyable experience. The spirit of camaraderie and the amicable atmosphere made life so much easier. Everyone was eager to help one another. How I can ever forget the coffee-and-ice-creams, the lunches at 12:20PM, coffee at 2:30PM, the music, the darts, ····· the list goes on.

There are quite a few with whom I have shared some of the most wonderful times of my graduate student life. Many have long since graduated and are doing extremely well in their professional careers - Chick, Dave, Gopal, Kevin and Dan. Others like Joe and Matt, with whom I spent six years together, were more than just office-mates; we were (and still are) buddies. We had a great time together - we worked and we partied. I will dearly treasure all the good old times.

I deeply appreciate all the help from Peter. He had the answers to all my computer related questions, especially when it came to thesis crunch time. Brian could always be counted upon to help whenever the need arose. Even though I have known Michael (Klaus) and Vince (Lupi) for a rather short time, it feels like forever. Although, Kai's visit to MIT was short, it was a fun-filled nine months. Yes, we did "in been" to many places together. We had some great philosophical discussions about research, life, careers, and what have you. There was never a time when Jeongho did not have a good story to tell. There are others who were more than just acquaintances - Bill, Caterina, Diane, Ken, Lisa, Mark, Pierre and Thanasis.

I hold a very special place for Karen in my heart. Constantly encouraging and

concerned about my welfare, you are more than just a good friend. I wish you and Matt all that you ever dreamed for. I have spent a memorable six years in the company of some of my good friends outside work - Kim, Pramod and Vivek Kapoor. There are others whom I could count upon for anything - Raghav, Sharmila and Vivek Mohindra. I know that we have a strong bond of friendship which will not dwindle with time. I am at a complete loss of words to express my appreciation for my sister Ketu who has also been a great friend. Your amiable disposition and warm personality have meant a lot to me. Whenever things looked down, I knew I could always turn to you for support. I will forever be indebted to you for everything.

Finally, I wish to thank my parents for their love, guidance, and constant encouragement. Words will never be able to express what I feel in my heart. You have been my role models and my source of inspiration, and now it is my turn to make you proud. I deeply appreciate my brothers - Kewal, Ajit and Anand, and sisters-in-law - Alka, Madhu and Asha, for all their good wishes. In spite of being far away, there was never a moment when you were not concerned about my well-being. You have done a lot for me over the years. I thank you from the bottom of my heart for all your love, support and encouragement.

"Where there is much desire to learn, there of necessity will be much arguing, much writing, many opinions; for opinion in good men is but knowledge in the making."

- John Milton

Contents

List of Figures

List of Tables

Chapter 1

Introduction

1.1 The Arctic Ocean Environment

The Arctic Ocean has historically been important for both economical and political reasons. It is an abundant reservoir of natural resources like minerals, oil and natural gas. Recently, it has found use in monitoring global climate change as demonstrated by the joint US-Russian long-range propagation experiment in the Arctic [1, 2]. The main idea behind that effort was to determine the feasibility of detecting global climate change by measuring the temperature of the Arctic Ocean. The prediction of this change involves monitoring the time it takes sound to travel thousands of miles. As sound travels faster in warmer water, shorter travel times observed over long periods of time would be an indicator of global warming.

Since the early 1960s, i.e., during the Cold War era, the Arctic Ocean has also been of strategic importance. During this period there was substantial interest in understanding issues related to long-range submarine detection and identification. This is a particularly difficult problem because of the complex nature of the boundaries of the waveguide and the presence of various sources of noise, both natural and man-made. Examples of man-made sources of noise include radiation from ship machinery and submarines, while natural sources include the cracking of ice due to environmental

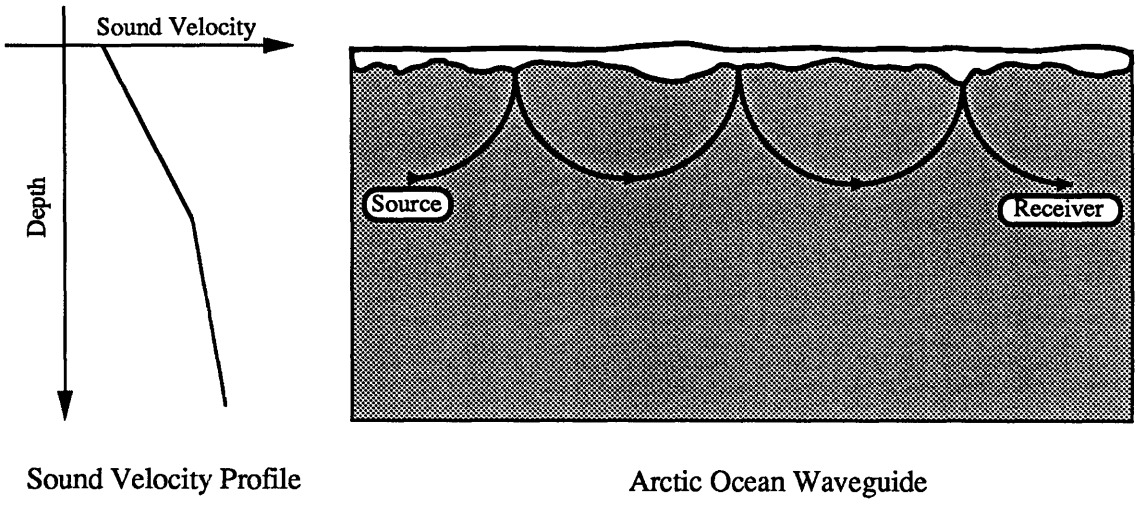

Figure 1-1: Characteristic Arctic Ocean sound velocity profile and corresponding propagation paths in the waveguide. The upward refracting SVP causes sound to repeatedly interact with the ice cover, distorting both amplitude and phase.

forces, and sounds from marine mammals. In contrast to signal propagation in the open deep oceans, the problem in the Arctic Ocean waveguide is further complicated by the presence of a 3.0 m thick floating ice-sheet. Much of the recent work has been devoted to developing an understanding of scattering of sound waves from the underside of this rough elastic interface.

It is natural to wonder why this is an important issue when considering propagation of sound in the Arctic Ocean. The reason being that any long-range propagation model must include the effects of interaction of the signal with the underside of the ice cover, as it alters both its amplitude and phase. This arises due to the upward refracting nature of the Sound Velocity Profile (SVP) in the Arctic Ocean waveguide which makes any signal propagating over long distances repeatedly interact with the ice canopy as shown in Fig. 1-1. At each interaction, the signal is partly reflected and scattered, with simultaneous excitation of elastic waves in the ice plate. One therefore needs to develop a good understanding of this interaction between the acoustic waves and the rough interface to realistically model propagation in the Arctic Ocean waveguide.

1.2 Thesis Problem and Related Previous Work

The goal of this thesis is to improve our understanding of low frequency scattering of acoustic waves from the ice canopy in the Arctic Ocean. The Arctic ice cover contains a wide spectrum of roughness extending from the minute deviations from the plane surface hardly visible to the naked eye, to protuberances whose dimensions are greater than the wavelengths of the acoustic signals typically used for long-range propagation in the Arctic Ocean ($f < 100Hz$). A lot of work has been done in the literature on scattering from rough surfaces. A good reference on wave scattering from rough surfaces is the review paper by Ogilvy [3] which discusses the different approaches, and their corresponding limitations for analyzing scattering. One can attempt to understand the physics of scattering of sound from a multi-scale rough surface like the Arctic ice canopy, by conveniently subdividing its roughness spectrum into three main categories. Assuming λ to be the wavelength of the acoustic signal, k its corresponding wavenumber, and a to be the characteristic dimension of the scale of roughness, we have the following three distinct regimes of roughness -

- Small scale (or very low frequency limit) : $ka << 1$
- Intermediate scale (or mid-frequency range) : $ka \sim O(1)$
- Large scale (or very high frequency limit) : $ka >> 1$

There is a plethora of analytical tools available for the analysis of scattering from small and large scales of roughness. Scattering from small scales of roughness can be accurately addressed using the Method of Small Perturbation (MSP). A good example of this approach is the recent work of Kuperman and Schmidt [4, 5]. This method, which is valid for small scales of roughness and slope, applies a self-consistent perturbation of the boundary conditions at the rough interface. The scattered field is shown to be driven by the mean or coherent field. It is important to note that inherent in this method is the capability to include the elasticity of the rough boundary.

One of the many possible ways of understanding scattering from relatively smooth, large scale features is via the Kirchoff approach, or the tangent plane method [6], which includes the capability of modeling scattering from elastic interfaces. This method assumes that sound reflects locally at each point on the surface as if from an infinite plane tangent to the rough surface at the point under consideration, i.e., the surface should appear flat relative to the acoustic wavelength. In other words, the Kirchoff approximation is valid when the condition $k\rho \sin^3 \theta >> 1$ is satisfied, where θ is the local grazing angle, and ρ is the local radius of curvature. The properties of the infinite plane are assumed to be same as those of the rough surface. This method works well for scattering in directions close to the directions of specular reflection. However, as discussed by Lepage [7], the Kirchoff method fails at shallow grazing angles where the backscatter is over-estimated even for moderately rough surfaces. In the case of penetrable boundaries, there is an additional constraint on the transmitted field which must also satisfy the criteria stated above. This means that the transmitted field must not propagate at zero grazing angles. Therefore, when the acoustic wave is incident at an angle corresponding to the critical grazing angle of the penetrable boundary, strong discrepancies arise between the results from the Kirchoff formulation and the exact solutions.

Finally, there is the intermediate regime, when the dimensions of the scatterer are comparable with the wavelength of the acoustic waves, where no such traditional analytical tools apply. This is the regime ($ka \sim O(1)$) which is much less understood, and there is considerable effort underway to further our knowledge of physics of the scattering phenomena. One of the earliest attempts by researchers in this field was to model these features as, for example, a hemispherical protuberance on an infinite plane. This is the classic Burke-Twersky approach [8, 9] or the *boss* model approach, where the rough surface is modeled as a random array of scatterers of simple geometric shapes. Chu and Stanton [10] have found reasonable agreement between the Burke-Twersky theory and high frequency laboratory measurements of sound scattered by a continuously rough pressure-release surface. However, the main drawback of the *boss* model is that it ignores the elasticity of the rough surface, and provides no insight

into the physical processes, and wave mechanisms involved in the scattering of sound by the ice.

More recently, with the availability of faster and more sophisticated computers, some researchers have devoted their efforts on the computational approach which may basically be divided into the following two types -

- Boundary Element Method (BEM) formulation of the boundary conditions surrounding the facet.
- Finite Difference (FD) approach which solves the elastodynamic equations numerically.

Both the BEM and FD, although computationally very intensive, allow for arbitrary scales of roughness and slope, and can be used to model scattering from a single isolated feature. A good 2D example of the BEM approach is the recent paper by Gerstoft and Schmidt [11], which combines Schmidt's Global Matrix approach with a boundary element formulation of the boundary conditions on a contour surrounding the facet. Regarding the FD approach, a contemporary example is the recent work of Fricke [12, 13] who implemented a 2D version of the FD approach to model scattering from isolated features like ice keels. He was able to demonstrate that elasticity of the ice plays an important role in defining the beampattern of the scattered field. Fricke also used the FD approach to hypothesize that new, fluid-like keels which do not support shear, dominate the scattering loss from Arctic ice. However, Lepage [7] later disputed this hypothesis by demonstrating that scatter into flexural and horizontally polarized shear (SH) modes must be considered for realistic attenuation mechanisms for coherent loss in the Arctic Ocean. It is worthwhile to note that SH modes come into play only in 3D formulations of scattering, once again emphasizing the need to consider the three-dimensionality of the scattering problem.

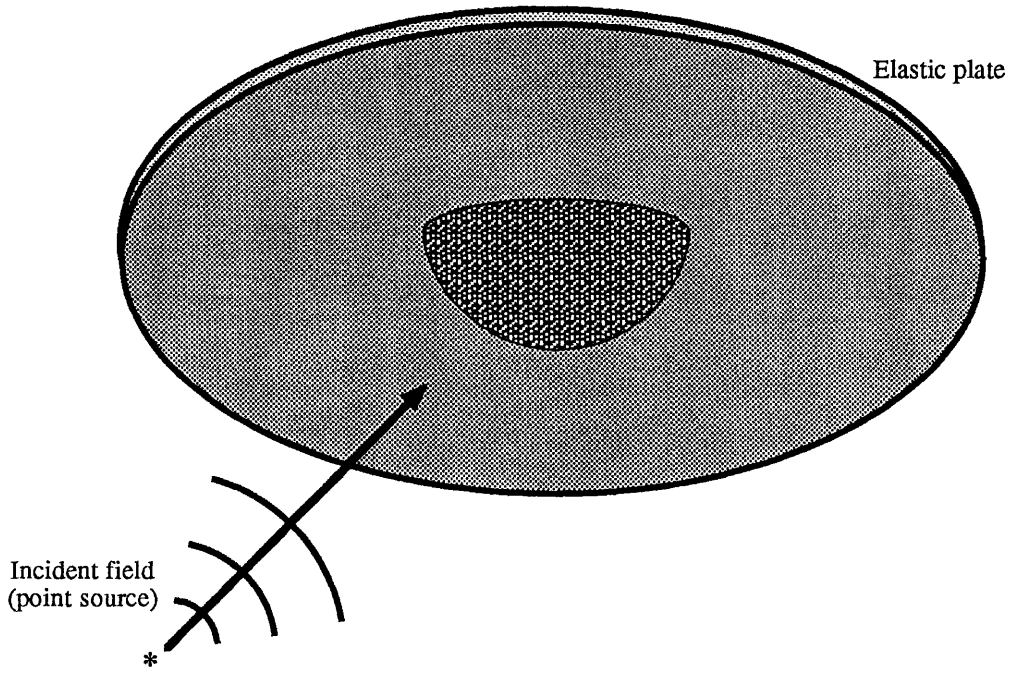

Figure 1-2: Model geometry for acoustic scattering from a three-dimensional feature under the ice cover.

1.3 Approach

The main focus of this thesis is to consider scattering from a three-dimensional feature or protuberance under Arctic ice as shown in Fig. 1-2. From the above discussion, it is evident that there are various options available to do this. One could possibly run a 3D version of either FD or BEM to synthesize the scattered field from a discrete isolated scatterer. On the other hand, one could conduct experiments, in the field or in the laboratory, and develop analytical models to help explain the data. Recently, there have been attempts to numerically model three-dimensional fluid-elastic interface scattering using the FD approach [14]. However, that analysis demonstrated the infeasibility of this method due to requirements of extensive computational facilities. There have also been attempts at 3D modeling using a boundary integral equation formulation [15]. Due to computational limitations, that analysis was restricted to scattering from a compact feature on a rigid boundary. Both these examples demonstrate the severe limitations imposed on numerical modeling within the confines of the presently available computational facilities. Therefore, I choose to make my analysis

more tractable by resorting to the latter approach in this thesis, where I will analyze field experimental data, and simultaneously develop a theoretical model to assist in the evaluation of three-dimensional scatter.

This thesis, therefore, may be viewed to consist of three main parts. In the first, I develop the analytical model and conduct a theoretical investigation of three-dimensional scatter. This analysis has a twofold objective. While providing an understanding of acoustic scatter from a large impedance discontinuity on an infinite, submerged plate, it will also aid in modeling the scattering pattern from under-ice features. This knowledge will be exploited in the second part, where I carry out an experimental evaluation of scattering using field data. The Matched Field analysis that will be conducted there requires a model of the replica fields. As the exact replica fields are computationally involved to compute, my theoretical analysis will guide me in developing an approximate model of the scattering pattern from Arctic ice features. In the final stage of this thesis, these two parts will come together, and I will compare my results from these two independent investigations. This will provide us with a complete understanding of the underlying wave phenomena, and will help us develop an appreciation of how the idealized environmental realizations compare with physical reality.

1.4 Organization of this thesis

The organization of this thesis is as follows. I begin with Chapter 2, where I derive the analytical solution for scattering from a thin, infinite, fluid-load plate with a three-dimensional protuberance whose dimensions are comparable with the wavelength of the incident acoustic waves. The canonical problem of scattering of acoustic waves from thin, infinite, elastic plates has been previously studied by many researchers in Structural Acoustics [16, 17, 18, 19, 20]. There have also been numerous efforts in the past to model scattering from a ribbed plate [21, 22], where the size of the rib was assumed to be small compared to the wavelength of the incident acoustic wave.

More recently, Guo [23] addressed the problem of scattering from an infinite, elastic plate loaded with fluid on one side and and a semi-infinite plate on the other. These studies reveal that an impedance discontinuity in the canonical geometry of a flat plate produces significant scattering into the fluid by both supersonic and subsonic waves in the plate. Additionally, subsonic waves get coupled into the plate by interaction of the acoustic wave with the impedance discontinuity. However, these studies were primarily two-dimensional in nature. Therefore, my theoretical investigation is an attempt to make forays into analytical modeling of three-dimensional impedance discontinuities.

Next I move on to analyzing experimental data. This will be the theme in Chapters 3 and 4, where I evaluate the scattering characteristics of large-scale features observed in the Arctic ice environment. This analysis involves the identification and isolation of "hot spots" under the ice canopy, and subsequent evaluation of their scattering patterns. We use the Matched Field Processor in a two step algorithm to solve this complex parameter estimation problem. In Chapter 3, I conduct a preliminary analysis of the field reverberation data, and discuss issues related to data conditioning, including source and array localizations. This will lead me to Chapter 4, where I solve the first step in the global parameter estimation problem, and identify discrete scatterers under the ice. My analysis in Chapter 2 will establish that I can model the features as point radiators with a quadrupolar scattering pattern. Fricke [13, 24] has demonstrated that the scattering pattern from a two-dimensional protuberance on an elastic plate in this frequency regime resembles a deformed quadrupole, especially near grazing angles of incidence. Moreover, the validity of this assumption for a 3D scattering scenario will also be confirmed by my analytical realizations of scatter from an isolated protuberance under ice. The use of this assumed scattering pattern will then provide me with a rough map of the under surface of the ice cover. My results will demonstrate that satisfactory results can be obtained with this assumption. This Chapter also estimates the global scattering characteristics of the ice cover.

Chapter 5 contains the second step in the global estimation problem where I evaluate the spatial scattering characteristics of these isolated features. The analysis is

made manageable by limiting the number of unknowns defining the nature of the scattered field. Simultaneously, I will compare the experimental results with those from an approximate theoretical formulation. The two separate investigations, though not directly comparable, will corroborate the physical mechanisms involved in three-dimensional scatter.

As a bonus, I have also derived the Greens functions for ring tractions in a solid unbounded elastic medium using spherical coordinates. Though not directly applicable to my theoretical formulation, this analysis which is presented in Appendix A of this thesis, aids in the derivation of the solutions to the plate-sphere coupled problem. The explicit analytical solutions presented there are useful when modeling the interaction between coupled structures using the full three-dimensional elastodynamic equations. This Appendix is a complete entity in itself, and I have included it in its entirety for future reference.

Chapter 2

Acoustic scattering from a three dimensional protuberance on a thin, infinite, submerged elastic plate

2.1 Introduction

In this Chapter, I develop the analytical solution for scattering from a thin, infinite, submerged elastic plate with a three-dimensional protuberance whose dimensions are comparable with the wavelength of the incident acoustic waves ($ka \sim O(1)$). The solution developed in this Chapter is "exact", and later in Chapter 5, I shall use an approximation of this model to represent scattering from a protuberance under the Arctic ice sheet. The size of the protuberance is large enough so that it can support elastic waves which can resonate, and additionally radiate into the fluid.

I begin by parameterizing the various wave phenomena involved in the scattering process in Section 2.2. Section 2.3 formulates the exact scattering problem using the Eulerian approach. In Section 2.4, I solve the decoupled constituent problems of the

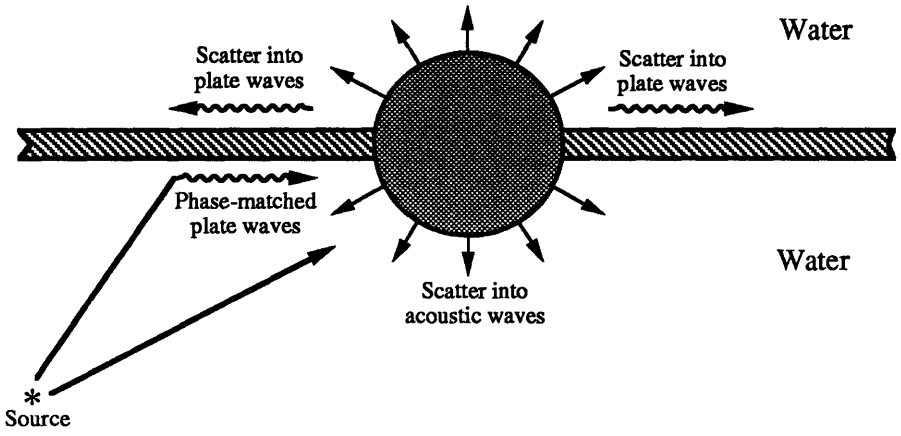

Figure 2-1: Schematic representation of source, plate and sphere geometry. The incident field excites waves inside the sphere and the plate, which then couple back into the surrounding acoustic medium.

free submerged sphere, the elastic plate, and the sphere excited by ring coupling forces and bending moment. Section 2.5 contains results from the analysis where I evaluate the attachment ring kinematics, the backscattered pressure, and the bistatic scattering pattern for scatter from the three-dimensional protuberance.

2.2 Parameterization of the Problem

Before formulating the problem of three dimensional scatter, I begin by parameterizing the wave phenomena involved in the scattering process. Fig. 2-1 shows the interaction between the incident sound field due to a point source and the plate-sphere coupled structure. The incident field excites elastic modes in the plate by phase-matching [25]. In general, assuming the plate to be thin, both compressional and flexural waves could be excited in the plate. With our plate parameters and frequencies of interest, only the lowest order plate modes are excited. These plate waves then travel towards the plate-sphere junction while radiating back into the fluid by phase-matched leakage. At the junction, they interact with the sphere and are (i) partially reflected back, (ii) partially converted into waves of other types, (iii) excite elastic waves in the sphere, and (iv) diffract into the fluid by scattering at the junction. Simultaneously, the

incident acoustic field excites the shear and compressional waves in the solid sphere, which then (i) radiate back into the fluid, (ii) excite structural waves in the plate, and (iii) diffract into the fluid by scattering at the junction. The total displacement components of the plate (subscripted with p) and sphere (subscripted with s) at the attachment ring can therefore be expressed as a sum of two components - one due to excitation by the acoustic wave (subscripted with a) and the other contribution due to the excitation by coupling forces and bending moment (subscripted with c) at that attachment ring, i.e.,

$$\begin{aligned} \mathbf{u}_{p,t} &= \mathbf{u}_{p,a} + \mathbf{u}_{p,c} \ , \\ \mathbf{u}_{s,t} &= \mathbf{u}_{s,a} + \mathbf{u}_{s,c} \ , \end{aligned} \tag{2.1}$$

where $\mathbf{u}_{p,t}$ and $\mathbf{u}_{s,t}$ represent the total displacements of the plate and sphere respectively, at the attachment ring.

It must be pointed out that in the formulation above I have neglected the contribution from the specular reflection from the side of the plate which may easily be added (e.g., see Ref. [25]). Once we have identified all the wave constituents that enter into the scattering scenario, I can then proceed to synthesize the total scattered field at the observer in terms of the contributions arising from the plate waves, and those due to the elastic waves in the sphere. The contributions from the plate waves excited by the incident field consist of (i) direct leakage of plate waves into the fluid by phase-matching, and (ii) diffraction of plate waves at the plate-sphere junction into the fluid. Similarly the elastic waves in the solid sphere contribute to the scattered field by (i) radiating back into the fluid, and (ii) diffracting into the fluid at the junction. The direct leakage of the plate waves and the radiation of the sphere modes can be easily computed by solving the canonical problems of an infinite submerged plate and the solid elastic sphere fully submerged under water. The solutions to both these constituent problems is well known, and therefore, I will present the significant results in an Appendix. Finally, just as I expressed the displacements in terms of two components, I express the total scattered pressure (p_t) in the fluid as a sum of the

contributions from the plate and sphere excited by the acoustic wave, and the coupling forces as

$$p_t = p_{s,a} + p_{s,c} + p_{p,a} + p_{p,c} \tag{2.2}$$

2.3 Coupling Formulation

The formulation for scattering from coupled elastic structures has been previously studied in great detail [26, 27, 28], where the Eulerian formulation was used to decompose the coupled structure into its decoupled constituents, with their interactions being accounted for by coupling forces and moments at the attachments. It was also shown that when the size of the attachments is small compared to wavelength, the junction could then be approximated as a point or ring junction as appropriate to the problem under consideration. If the attachment area is larger, then this may be viewed as a first order approximation to the exact solution.

The methodology of this approach is as follows. First, one must solve for the dynamics of the decoupled constituents independently. However, one needs to add some unknown source terms to account for the coupling at the attachment. In general, one expands these source terms in terms of coupling forces and moments depending on the characteristics of the attachment junctions. For example, if we have a pinned joint we need to retain only forces, whereas for a clamped joint, the analysis must include both forces and moments. These are in turn then determined by matching the kinematics of the constituent structures at the attachment junction, for example, displacements and slopes. This yields a set of algebraic equations which can then be solved for the unknown coupling forces and moments.

At this juncture, it is worthwhile to point out that for an arbitrary attachment between two structures, three components of stress and three displacement components must be matched at that junction. This is a complex problem to solve since the stress distribution at the junction is not known a priori. A possible solution procedure would involve making assumptions regarding the form of the stress distribution

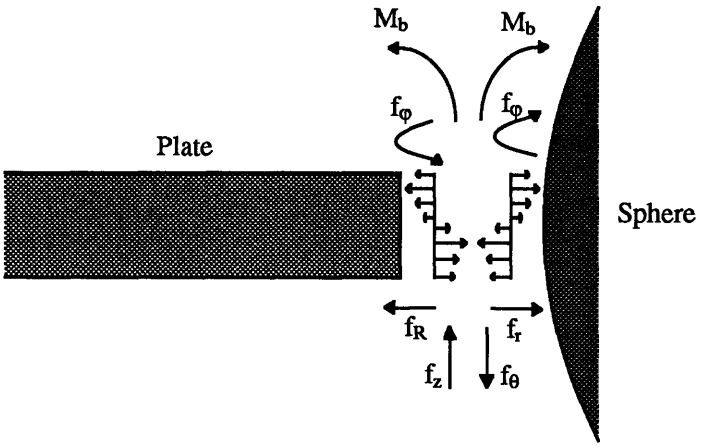

Figure 2-2: Coupling forces and bending moments involved in characterization of the attachment ring. The forces and moments for the plate are shown in their positive sense

in terms of some unknown coefficients, and then solving the boundary conditions for those unknown constants. Thus, in my model, where the thickness of the plate is small but not negligible compared to wavelength, I should match stresses at the plate-sphere junction. However, I choose to make the analysis more tractable by matching equivalent forces and moments (or integrated stresses) at the junction modeled as a ring of zero width. This is also consistent with the use of thin plate theory for the plate. Moreover, structural continuity requirements will be satisfied since I constrain the displacements and slopes at the junction.

The dynamics of the plate at the attachment junction are characterized by in-plane and out-of-plane motions. Out-of-plane displacements are produced by including a vertical shear force (f_z) and a bending moment (M_b), while in-plane displacements are obtained by including the radial (f_R) and circumferential (f_φ) in-plane forces in the analysis. Fig. 2-2 shows the junction between the plate and the sphere with the various coupling forces and moments. Also shown in the figure is the unknown stress distribution that exists at the coupling junction.

The displacements of the sphere due to the incident acoustic wave ($\mathbf{u}_{s,a}$) will be

found in subsection 2.4.1, and may be expressed as

$$\mathbf{u}_{s,a} = \sum_{m=-\infty}^{\infty} \underbrace{\left\{ \sum_{n=|m|}^{\infty} G_n^m \tilde{\mathbf{u}}_{s,a} \right\}}_{\hat{\boldsymbol{\Upsilon}}_s} e^{im\varphi} \tag{2.3}$$

where $\tilde{\mathbf{u}}_{s,a}$ are the displacements of polar order n and azimuthal order m, and G_n^m is defined later in eqn. (2.17). Here the 'hat' notation is used to denote dependence on the azimuthal order m only. Similarly, the plate displacements due to the incident acoustic wave may be expressed in the form

$$\mathbf{u}_{p,a} = \sum_{m=-\infty}^{\infty} \hat{\boldsymbol{\Upsilon}}_p e^{im\varphi} \quad . \tag{2.4}$$

From the analysis of the governing equations of motion of the elastic plate (see subsection 2.4.2), we may write the displacements of the plate due to the ring forces and bending moments as

$$\mathbf{u}_{p,c} = \sum_{m=-\infty}^{\infty} \hat{\boldsymbol{\Lambda}}_p \hat{\mathbf{f}}_p e^{im\varphi} \quad , \tag{2.5}$$

where $\hat{\boldsymbol{\Lambda}}_p = \hat{\mathbf{Z}}_p / 2\pi$ and $\hat{\mathbf{f}}$ denotes the Fourier Transform of the vector of coupling forces and is a function of the Fourier (azimuthal) order m only. $\hat{\mathbf{Z}}_p$ is the *influence matrix* for the plate and may be interpreted as being the admittance or mobility matrix relating forces and moments to velocities and rotation rates. It is given by

$$\begin{Bmatrix} \hat{v}_R \\ \hat{v}_\varphi \\ \hat{w} \\ \partial\hat{w}/\partial R \end{Bmatrix} = \begin{bmatrix} \hat{P}_{11} & \hat{P}_{12} & 0 & 0 \\ \hat{P}_{21} & \hat{P}_{22} & 0 & 0 \\ 0 & 0 & \hat{P}_{33} & \hat{P}_{34} \\ 0 & 0 & \hat{P}_{43} & \hat{P}_{44} \end{bmatrix} \begin{Bmatrix} \hat{f}_R \\ \hat{f}_\varphi \\ \hat{f}_z \\ \hat{M}_b \end{Bmatrix} . \tag{2.6}$$

The upper-right and lower-left quarters of the influence matrix are 0 since the in-plane motions are decoupled from the out-of-plane motions in thin plate theory, as shown

later. For the sphere, the resultants act in the opposite direction, and we will have

$$\mathbf{u}_{s,c} = \sum_{m=-\infty}^{\infty} \underbrace{\left\{ \frac{1}{2\pi} \sum_{n=|m|}^{\infty} a_{mn} \tilde{\mathbf{Z}}_s \right\}}_{\hat{\mathbf{\Lambda}}_s} \hat{\mathbf{f}}_s e^{im\varphi} \quad , \tag{2.7}$$

where

$$a_{mn} = \frac{2n+1}{2} \frac{(n-m)!}{(n+m)!} \quad ,$$

and $\mathbf{u}_{s,c}$ is the displacement of the sphere due to the ring forces and bending moments. Note that I have implicitly assumed that $\hat{\mathbf{f}}_s$ acts in an opposite sense to $\hat{\mathbf{f}}_p$. $\tilde{\mathbf{Z}}_s$ is the *influence matrix* for the sphere (derived in subsection 2.4.3), and is given by

$$\begin{Bmatrix} \tilde{u}_r \\ \tilde{u}_\varphi \\ \tilde{u}_\theta \\ \partial \tilde{u}_r / r \partial \theta \end{Bmatrix} = \begin{bmatrix} \tilde{S}_{11} & \tilde{S}_{12} & \tilde{S}_{13} & \tilde{S}_{14} \\ \tilde{S}_{21} & \tilde{S}_{22} & \tilde{S}_{23} & \tilde{S}_{24} \\ \tilde{S}_{31} & \tilde{S}_{32} & \tilde{S}_{33} & \tilde{S}_{34} \\ \tilde{S}_{41} & \tilde{S}_{42} & \tilde{S}_{43} & \tilde{S}_{44} \end{bmatrix} \begin{Bmatrix} \hat{f}_r \\ \hat{f}_\varphi \\ \hat{f}_\theta \\ \hat{M}_b \end{Bmatrix} . \tag{2.8}$$

Here the 'tilde' notation is used to denote dependence on both the polar order n and the azimuthal order m. Matching displacements at the attachment ring yields

$$\mathbf{u}_{p,a} + \mathbf{u}_{p,c} = \mathbf{T} \left[\mathbf{u}_{s,a} + \mathbf{u}_{s,c} \right]$$

or

$$\mathbf{u}_{s,a} - \mathbf{T}^{-1} \mathbf{u}_{p,a} = \mathbf{T}^{-1} \mathbf{u}_{p,c} - \mathbf{u}_{s,c} \quad , \tag{2.9}$$

where $\mathbf{T}$ is the transformation matrix from spherical to cylindrical coordinates for both displacements and forces, and is given by

$$\begin{Bmatrix} \hat{f}_R \\ \hat{f}_\varphi \\ \hat{f}_z \\ \hat{M}_b \end{Bmatrix} = \begin{bmatrix} \sin\gamma & 0 & \cos\gamma & 0 \\ 0 & 1 & 0 & 0 \\ \cos\gamma & 0 & -\sin\gamma & 0 \\ 0 & 0 & 0 & 1 \end{bmatrix} \begin{Bmatrix} \hat{f}_r \\ \hat{f}_\varphi \\ \hat{f}_\theta \\ \hat{M}_b \end{Bmatrix} . \tag{2.10}$$

Here γ is the polar angle at the junction ring. Inserting eqns. (2.5) - (2.7) into eqn. (2.9), we can write

$$\hat{\Upsilon}_s - \mathbf{T}^{-1}\hat{\Upsilon}_p = \mathbf{T}^{-1}\hat{\Lambda}_p\hat{\mathbf{f}}_p - \hat{\Lambda}_s\hat{\mathbf{f}}_s \quad . \tag{2.11}$$

Now inserting $\hat{\mathbf{f}}_p = \mathbf{T}\hat{\mathbf{f}}_s$ into eqn. (2.11), we have

$$\hat{\Upsilon}_s - \mathbf{T}^{-1}\hat{\Upsilon}_p = \left[\mathbf{T}^{-1}\,\hat{\Lambda}_p\,\mathbf{T} - \hat{\Lambda}_s\right]\hat{\mathbf{f}}_s \quad ,$$

and therefore, the coupling forces are found to be

$$\hat{\mathbf{f}}_s = \left[\mathbf{T}^{-1}\,\hat{\Lambda}_p\,\mathbf{T} - \hat{\Lambda}_s\right]^{-1}\left[\hat{\Upsilon}_s - \mathbf{T}^{-1}\hat{\Upsilon}_p\right] \quad . \tag{2.12}$$

Then using eqns. (2.5) and (2.7) , we can finally solve for the displacements $\mathbf{u}_{s,c}$ and $\mathbf{u}_{p,c}$.

2.4 The Decoupled Constituent Problems

In my formulation, I need to determine the kinematics of the plate and sphere at the attachment ring. This is done by solving each of the decoupled constituent problems separately. In the following sub-sections, I shall determine the displacement of the sphere at the coupling junction due to the incident acoustic wave ($\mathbf{u}_{s,a}$) in subsection 2.4.1, and the influence matrices for the plate ($\hat{\mathbf{Z}}_p$) and the sphere ($\tilde{\mathbf{Z}}_s$) in subsections 2.4.2 and 2.4.3 respectively. The total scattered field is then synthesized in subsection 2.4.4.

2.4.1 The free submerged sphere

Scattering of acoustic waves by a solid elastic sphere submerged in a fluid is well understood [29, 30, 31, 32]. However, previous analyses were limited to plane waves incident along one of the coordinate axes, or axisymmetric point source loadings [33],

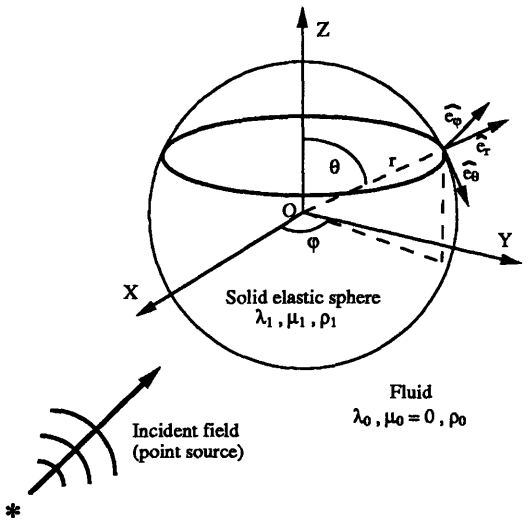

Figure 2-3: Geometry for scattering from a submerged solid elastic sphere due to an incident point source field.

which simplified the algebra considerably. In my case, I need to compute the scattered field and displacement fields along a ring on the sphere due to a point source located at an arbitrary position (r_0, θ_0, φ_0) as shown in Fig. 2-3. The sphere is assumed to have material properties (λ_1, μ_1, ρ_1) and is of radius a, while the surrounding fluid medium has material properties (λ_0, $\mu_0 = 0$, ρ_0), where λ and μ are Lamé constants, and ρ is the density of the material. The equations governing the motions of a homogeneous isotropic elastic solid are given by

$$(\lambda_1 + 2\mu_1)\nabla\nabla\cdot\mathbf{u} - \mu_1\nabla\times\nabla\times\mathbf{u} + \rho_1\mathbf{f} = \rho_1\frac{\partial^2\mathbf{u}}{\partial t^2} \quad , \tag{2.13}$$

where $\mathbf{u}$ is the displacement vector, $\mathbf{f}$ is the body force per unit mass of material, and the Laplacian operator in spherical coordinates is given by

$$\nabla^2 \equiv \frac{1}{r^2}\frac{\partial}{\partial r}\left(r^2\frac{\partial}{\partial r}\right) + \frac{1}{r^2\sin\theta}\frac{\partial}{\partial\theta}\left(\sin\theta\frac{\partial}{\partial\theta}\right) + \frac{1}{r^2\sin^2\theta}\frac{\partial^2}{\partial\varphi^2} \quad .$$

Following [34], I write the displacement potential in terms of three scalar fields, ϕ, ψ and $\check{\chi}$, i.e

$$\mathbf{u} = \nabla\phi + \nabla\times(\hat{e}_r r\psi) + \nabla\times\nabla\times(\hat{e}_r r\check{\chi}) \quad , \tag{2.14}$$

where the first term is the longitudinal part of the solution, and the other two are the transverse parts. Assuming an $\exp(-i\omega t)$ harmonic time dependence (suppressed henceforth), the potentials may be shown to satisfy the following Helmholtz equations

$$\begin{aligned} \left(\nabla^2 + \alpha_1^2\right)\phi &= 0 \ , \\ \left(\nabla^2 + \beta_1^2\right)\psi &= 0 \ , \\ \left(\nabla^2 + \beta_1^2\right)\chi &= 0 \ , \end{aligned} \tag{2.15}$$

where $\alpha_1 = \omega/c_\alpha$ and $\beta_1 = \omega/c_\beta$ denote the wavenumbers for the compressional and shear waves respectively, and c_α and c_β are compressional and shear wave speeds respectively, with

$$c_\alpha = \sqrt{\frac{\lambda_1 + 2\mu_1}{\rho_1}} \ , \ c_\beta = \sqrt{\frac{\mu_1}{\rho_1}} \ .$$

Also, I have normalized the potential $\check{\chi}$ by the shear wavenumber β as $\chi = \beta\check{\chi}$ so that the dimensions of ϕ, $r\psi$ and $r\chi$ are the same. Expanding the potential functions which satisfy eqn. (2.15) in terms of Spherical Bessel functions in r, associated Legendre functions in θ, and Fourier series in φ, I can find the resulting stress and displacement components. However, as discussed in Appendix A, these stresses and displacements contain a mixed dependence on the order of the associated Legendre functions $P_n^m(\cos\theta)$ and $P_{n-1}^m(\cos\theta)$. Therefore, following Appendix A, I shall instead satisfy the boundary conditions with transformed stress and displacement components which decouple in order n.

I begin by expanding the Helmholtz potentials for the incident, scattered and interior fields in terms of spherical waves as

$$\begin{aligned} \phi_i &= \sum_{m=-\infty}^{\infty} \sum_{n=|m|}^{\infty} G_n^m j_n(\alpha_0 r) P_n^m(\cos\theta) e^{im\varphi} \ , \\ \phi_s &= \sum_{m=-\infty}^{\infty} \sum_{n=|m|}^{\infty} A_{mn} G_n^m h_n(\alpha_0 r) P_n^m(\cos\theta) e^{im\varphi} \ , \\ \phi_r &= \sum_{m=-\infty}^{\infty} \sum_{n=|m|}^{\infty} B_{mn} G_n^m j_n(\alpha_1 r) P_n^m(\cos\theta) e^{im\varphi} \ , \end{aligned}$$

$$\psi_r = \sum_{m=-\infty}^{\infty} \sum_{n=|m|}^{\infty} C_{mn} G_n^m j_n(\beta_1 r) P_n^m(\cos\theta) e^{im\varphi} \quad ,$$

$$\chi_r = \sum_{m=-\infty}^{\infty} \sum_{n=|m|}^{\infty} D_{mn} G_n^m j_n(\beta_1 r) P_n^m(\cos\theta) e^{im\varphi} \quad , \tag{2.16}$$

where I have used the compact notation $h_n^{(1)} \equiv h_n$ to denote spherical Hankel functions of the first kind. The subscripts i and s denote the incident and scattered fields respectively, and r denotes the field inside the solid, and

$$G_n^m = i\,2\,\alpha_0 \frac{p_0}{\rho_0 \omega^2} a_{mn}\, h_n(\alpha_0 r_0) P_n^m(\cos\theta_0) e^{-im\varphi_0} \quad . \tag{2.17}$$

Here p_0 is the amplitude of the incident pressure at the surface of the sphere and a_{mn} was defined earlier. The scattered pressure is given by $p_{s,a} = \rho_0 \omega^2 \phi_s$, and our notation for negative orders m for the associated Legendre functions P_n^{-m} is as follows

$$P_n^{-m}(\cos\theta) = (-1)^m \frac{(n-m)!}{(n+m)!} P_n^m(\cos\theta) \quad .$$

Following Ref. [35], four boundary conditions need to be satisfied at the fluid-solid interface - (i) continuity of normal displacement, (ii) continuity of normal stress (pressure) (iii) vanishing of the shear stress $\tau_{r\theta}$ at the boundary, and (iv) vanishing of the shear stress $\tau_{r\varphi}$ at the surface of the sphere. The tangential stresses $\tau_{r\theta}$ and $\tau_{r\phi}$ are coupled in the polar order n, and the azimuthal order m. Since both must vanish at the surface of the sphere, any linear combination of these stresses must also be identically zero there. As described in Appendix A, I can alternatively prescribe the vanishing of the transformed stress components which are decoupled between the orders n and m. Then, using (2.16) and the expressions for displacements and stresses from Appendix A, the boundary conditions yield a system of equations which can be solved for the four unknown constants A_{mn}, B_{mn}, C_{mn} and D_{mn} (See Appendix B.2 for details). Finally, I can write the displacement components $\tilde{\mathbf{u}}_{s,a}$ at the attachment ring, $r = a$ and $\theta = \gamma$, on the free submerged sphere due to the incident acoustic wave

as

$$
\begin{aligned}
\tilde{u}_r &= \frac{1}{a}\left[B_{mn}\left\{nj_n(\alpha_1 a)-\alpha_1 a j_{n+1}(\alpha_1 a)\right\}+D_{mn}\frac{n(n+1)}{\beta_1}j_n(\beta_1 a)\right]P_n^m(\cos\gamma)\ , \\
\tilde{u}_\theta &= \frac{1}{a}\left[B_{mn}j_n(\alpha_1 a)+D_{mn}\frac{1}{\beta_1}\left\{(n+1)j_n(\beta_1 a)-\beta_1 a j_{n+1}(\beta_1 a)\right\}\right]\left[\frac{d}{d\theta}P_n^m(\cos\theta)\right]_{\theta=\gamma} \\
&\quad +C_{mn}j_n(\beta_1 a)\frac{im}{\sin\gamma}P_n^m(\cos\gamma)\ , \\
\tilde{u}_\varphi &= \frac{1}{a}\left[B_{mn}j_n(\alpha_1 a)+D_{mn}\frac{1}{\beta_1}\left\{(n+1)j_n(\beta_1 a)-\beta_1 a j_{n+1}(\beta_1 a)\right\}\right]\frac{im}{\sin\gamma}P_n^m(\cos\gamma) \\
&\quad -C_{mn}j_n(\beta_1 a)\left[\frac{d}{d\theta}P_n^m(\cos\theta)\right]_{\theta=\gamma}\ , \\
\frac{1}{r}\frac{\partial\tilde{u}_r}{\partial\theta} &= \frac{1}{a^2}\left[B_{mn}\left\{nj_n(\alpha_1 a)-\alpha_1 a j_{n+1}(\alpha_1 a)\right\}+D_{mn}\frac{n(n+1)}{\beta_1}j_n(\beta_1 a)\right]\left[\frac{d}{d\theta}P_n^m(\cos\theta)\right]_{\theta=\gamma}\ ,
\end{aligned}
\tag{2.18}
$$

where

$$
\left[\frac{d}{d\theta}P_n^m(\cos\theta)\right]_{\theta=\gamma} = n\cot\gamma P_n^m(\cos\gamma)-\frac{n+m}{\sin\gamma}P_{n-1}^m(\cos\gamma)\ .
$$

2.4.2 Thin elastic plate vibrations

Consider a thin infinite circular elastic plate of thickness h with an interior annulus of radius $b = a\sin\gamma$, and completely submerged in fluid. Here γ is the azimuthal angle on the sphere at which the sphere is attached to the plate and a is the radius of the sphere. The elastic plate is assumed to have material properties (λ_2, μ_2, ρ_2) which could possibly be the same as those of the attached sphere (λ_1, μ_1, ρ_1) while, as before, the fluid medium has material properties (λ_0, $\mu_0 = 0$, ρ_0). I assume the plate to be thin so that its flexural motions are decoupled from its extensional and shear motions. Moreover, using thin plate theory is consistent with my model of the plate-sphere ring attachment junction where I apply equivalent coupling forces and bending moments. Also, assuming a 3.0 m thick ice sheet, thin plate theory is applicable for frequencies less than about 100 Hz (see Ref. [20]). It must also be pointed out here that the exact

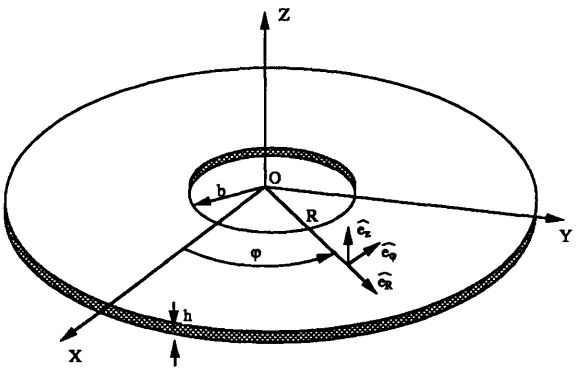

Figure 2-4: Geometry for a fluid-loaded elastic plate of thickness h excited by ring forces and bending moment at the interior annulus of radius b.

decoupled problem required to be solved as per my formulation is that of an annular plate completely submerged in water. For low frequencies, I assume that the fluid filling the annulus of the plate will not significantly alter the results of the analysis of plate vibrations presented in the following sections.

In-plane (compressional and shear) Motions

The extensional and shear motions of the plate can be formulated in terms of the in-plane displacement components, v_R and v_φ, in the radial and azimuthal directions respectively, which in turn can be expressed in terms of two potential functions Γ and Ω [36, 37] which satisfy the wave equations

$$\begin{aligned} \nabla^2\Gamma + \kappa^2\Gamma &= 0 \ , \\ \nabla^2\Omega + \eta^2\Omega &= 0 \ \cdot \end{aligned} \tag{2.19}$$

Here $\kappa = \omega/c_\kappa$, $\eta = \omega/c_\eta$ are the wavenumbers of the compressional and shear waves respectively, c_κ and c_η are the compressional and shear wave speeds,

$$c_\kappa = \sqrt{\frac{\lambda_2 + 2\mu_2}{\rho_2}} \ , \ c_\eta = \sqrt{\frac{\mu_2}{\rho_2}} \ \cdot \tag{2.20}$$

It must be noted here that fluid-loading changes the speed of the compressional modes by a very small amount as shown by Langley [18]. However, this component is extremely small for our parameters of interest and I shall disregard this correction. The in-plane displacements can then be expressed in terms of the two displacement potential functions as

$$\begin{aligned} v_R &= \frac{\partial \Gamma}{\partial R} + \frac{1}{R}\frac{\partial \Omega}{\partial \varphi} \ , \\ v_\varphi &= \frac{1}{R}\frac{\partial \Gamma}{\partial \varphi} - \frac{\partial \Omega}{\partial R} \ . \end{aligned} \tag{2.21}$$

Note that there is no z dependence in these expressions since the plate is assumed to be thin. For $R \geq a$, the solutions are

$$\begin{aligned} \Gamma(R,\varphi) &= \frac{1}{2\pi}\sum_{m=-\infty}^{\infty} \hat{C}_1 H_m(\kappa R) e^{im\varphi} \ , \\ \Omega(R,\varphi) &= \frac{1}{2\pi}\sum_{m=-\infty}^{\infty} \hat{C}_2 H_m(\eta R) e^{im\varphi} \ . \end{aligned} \tag{2.22}$$

where I have used the compact notation $H_m^{(1)} \equiv H_m$ to denote cylindrical Hankel functions of the first kind. The two unknown coefficients $\hat{C}_1$ and $\hat{C}_2$ are determined from the boundary conditions at $R = b$. Assuming the stresses τ_{RR} and $\tau_{R\varphi}$ are uniformly distributed over the inner circular edge of the plate, force equilibrium yields

$$\tau_{RR} = -\frac{f_R}{2\pi bh} \ , \quad \tau_{R\varphi} = -\frac{f_\varphi}{2\pi bh} \ . \tag{2.23}$$

Matching these stresses at the inner annulus of the plate, yields a set of equations for the constants $\hat{C}_1$ and $\hat{C}_2$, and therefore the elements $\hat{P}_{ij}$ $(i,j = 1,2)$. Details of this analysis and appropriate results are given in Appendix B.3.1.

Out-of-plane (flexural) Motions

The transverse displacement $w(R,\varphi)$, of the fully submerged plate satisfies the PDE [16, 20]

$$\nabla^4 w - k_f^4 w = -\frac{1}{D}\left[p_2|_{z=\frac{h}{2}} - p_1|_{z=-\frac{h}{2}}\right] \ , \tag{2.24}$$

where p_1 and p_2 are acoustic fields in the lower and upper semi-infinite fluid media respectively. $k_f = (\rho_s h\omega^2/D)^{1/4}$ is the flexural wavenumber of the free plate in vacuum, h is the thickness of the plate, $D = Eh^3/12(1-\nu^2)$, and E and ν are the Young's modulus and Poisson's ratio, respectively. As in the case of in-plane motions, I begin by decomposing the φ dependence into angular harmonics, and then solve eqn. (2.24) in terms of cylindrical Hankel functions and modified Bessel functions as

$$w(R,\varphi) = \frac{1}{2\pi}\sum_{m=-\infty}^{\infty}\left[\hat{C}_3 H_m(\xi_f R) + \hat{C}_4 K_m(\xi_f R)\right] e^{im\varphi} \ . \tag{2.25}$$

ξ_f is the flexural wavenumber in the submerged plate in the low-frequency limit approximated by [18, 20]

$$\xi_f \sim k_f\left[1 + \frac{2\rho_0}{\rho_2 h\sqrt{k_f^2 - k_0^2}}\right]^{1/4} \ . \tag{2.26}$$

I account for the coupling forces and bending moments via the boundary conditions at $R = b$. From Ref. [38], the boundary conditions are given by

$$M_r = -\frac{M_b}{2\pi b} \ , \ V_r = -\frac{f_z}{2\pi b} \ , \tag{2.27}$$

where M_r is the bending moment, and V_r is the Kelvin-Kirchoff reaction at the interior edge of the plate. Matching these at the inner annulus of the plate, yields another set of equations for the constants $\hat{C}_3$ and $\hat{C}_4$, and therefore the elements $\hat{P}_{ij}$ $(i,j = 3,4)$. Details of this analysis and appropriate results are presented in Appendix B.3.2.

Plate displacements due to incident acoustic wave

For the sake of completeness of my analytical formulation, I need to evaluate the displacement components in the plate due to the incident acoustic field due to a point source in the fluid. In general, the components of $\hat{\Upsilon}_p$ may be found by carrying out an analysis similar to the one described in the previous subsections. We can expand the incident and scattered fields, as well as the plate displacement components, in terms of cylindrical waves. In general, at low frequencies. both compressional and flexural modes can be excited in the infinite submerged plate, with the supersonic longitudinal wave being excited due to Poisson's effect. Therefore, both these plate modes need to be retained in this analysis. Note that the in-plane shear modes are not excited as their motions do not couple into the fluid. The Fourier coefficients corresponding to these can then be found by matching the boundary conditions at the fluid-elastic interface. It is imperative to include this component to find the exact solution to this coupled scattering problem. However, the flexural modes, being subsonic in this frequency regime, do not radiate from the plate by phase-matching [39], creating only an evanescent wave field near the surface of the plate.

Anticipating the problem of scattering from a protuberance under the ice canopy in the Arctic Ocean, my primary interest is to model the direct scatter of acoustic waves from the protuberance. In the real scattering scenario, the flexural and compressional modes that couple into the ice would have encountered a multitude of such protuberances while traveling towards the one of interest to me. At each such interaction, they would undergo mode conversion and transmission, thereby causing a loss in energy in the modes. It is a formidable task to keep track of all such interactions.

Secondly, as I will demonstrate later (see Fig. 2-17), the displacement components at the attachment ring due to these acoustically excited modes is extremely small (less than -80 dB) compared to those excited by the coupling forces and moments. Therefore, it is justified to ignore this contribution when synthesizing the total scattered field. This has the additional advantage of making the analysis more tractable. Therefore, setting the plate displacement vector $\mathbf{u}_{p,a}$ to be identically *zero*, eqn. (2.12)

simplifies to

$$\hat{\mathbf{f}}_s = \left[\mathbf{T}^{-1}\,\hat{\mathbf{\Lambda}}_p\,\mathbf{T} - \hat{\mathbf{\Lambda}}_s\right]^{-1}\hat{\mathbf{\Upsilon}}_s \ . \tag{2.28}$$

2.4.3 Solid elastic sphere kinematics

In developing the solutions for the displacement components on the sphere excited by surface ring tractions, I will follow the approach detailed in Appendix A, by first eliminating the mixed dependence of the tractions and displacements on terms containing P_n^m and P_{n-1}^m using the linear transformation described there. Next I expand the radiated and interior Helmholtz potentials in terms of Spherical Harmonic Waves (SHW) as

$$\begin{aligned} \tilde{\phi}_s &= I_{mn} h_n(\alpha_0 r) \quad , \quad \tilde{\phi}_r = J_{mn} j_n(\alpha_1 r) \quad , \\ \tilde{\psi}_r &= K_{mn} j_n(\beta_1 r) \quad , \quad \tilde{\chi}_r = L_{mn} j_n(\beta_1 r) \quad , \end{aligned} \tag{2.29}$$

where the SHW decomposition is defined as

$$\begin{aligned} \tilde{g}(n,m) &= \int_{-\pi}^{\pi} e^{-im\varphi} d\varphi \int_0^{\pi} g(\theta,\varphi) P_n^m(\cos\theta) \sin\theta d\theta \ , \\ g(\theta,\varphi) &= \frac{1}{2\pi} \sum_{m=-\infty}^{\infty} e^{im\varphi} \sum_{n=|m|}^{\infty} a_{mn} \tilde{g}(n,m) P_n^m(\cos\theta) \ . \end{aligned}$$

The coefficients I_{mn}, J_{mn}, K_{mn} and L_{mn} for the ring traction loads $\mathbf{f}_s$, with components $(f_r, f_\theta, f_\varphi, M_b)$, are found by matching the stresses at the attachment ring ($r = a$, $\theta = \gamma$) for each constituent traction load individually. The traction loads at the attachment ring are represented as

$$\tau_s^0(a,\theta,\varphi) = \mathbf{f}_s(\varphi) \frac{\delta(\theta-\gamma)}{2\pi a^2 \sin\theta} \ . \tag{2.30}$$

Expanding both sides in terms of SHW, and balancing tractions yields expressions for the amplitudes of the potentials I_{mn}, J_{mn}, K_{mn} and L_{mn}. The details of this analysis and the appropriate results have been outlined in Appendix B.4.

2.4.4 Total scattered pressure

As discussed earlier, the total scattered pressure is the sum of two contributions - one due to the incident acoustic wave, and the other due to the forced motions of the sphere. The compressional modes are weakly coupled to the fluid, while the flexural modes produce an evanescent field in the fluid. Therefore, assuming we are far enough from the plate, the contribution due to the latter can be neglected. Ignoring the radiated field due to the compressional mode, the contributions from the plate due to $p_{p,a}$ and $p_{p,c}$ can be identically set to *zero*. The contributions from the sphere consist of the component due to the acoustic field ($p_{s,a}$) which was found in subsection 2.4.1, and that due to excitation by the coupling forces and bending moment. The displacement components due to the forced excitation of the sphere were evaluated in subsection 2.4.3. The radiated pressure due to the latter is computed by summing up the contributions from the sphere excited by the ring coupling forces and bending moment as

$$p_{s,c} = \frac{1}{2\pi} \sum_{m=-\infty}^{\infty} \sum_{n=|m|}^{\infty} a_{mn} \mathcal{I}_{mn} h_n(\alpha_0 r) P_n^m(\cos\theta) e^{im\varphi} \quad , \tag{2.31}$$

where

$$\mathcal{I}_{mn} = \rho_0 \omega^2 \left[I_{mn}|_{\hat{f}_r} + I_{mn}|_{\hat{f}_\varphi} + I_{mn}|_{\hat{f}_\theta} + I_{mn}|_{\hat{M}_b} \right] \cdot \tag{2.32}$$

2.5 Results

In this Section, I present the results from my analytical model of scattering from the three-dimensional protuberance on the thin infinite fluid-loaded elastic plate. For the purpose of illustration, I choose the material for the model to be solid ice of density $\rho_1 = \rho_2 = 910\ Kg/m^3$, compressional wave speed $C_p = 3500\ ms^{-1}$, and shear wave speed $C_s = 1600\ ms^{-1}$. The ice plate is assumed to be 3.0 m thick and attached to a sphere of radius 10.0 m along its equator ($\gamma = 90.0^o$). The coupled structure is completely submerged in water of density 1000 Kg/m^3 and sound speed 1460 ms^{-1}. The sphere is placed at the origin of the coordinate system and the point source is positioned at

r = 780.0 m, $\theta_0 = 130.0^o$ (or 40.0^o grazing) and $\varphi = 0.0^o$ which corresponds to X = -600 m, Y = 0.0 m, Z = -500 m in Cartesian coordinates.

2.5.1 Benchmarking via sanity checks

Before presenting results from this three-dimensional scattering scenario, it is imperative that I validate my analysis by running some sanity checks on my analytical model. This is especially important since I have no benchmark solutions for three-dimensional scattering available for comparison. Therefore, I present three cases to validate my theoretical model.

Rigid and pressure-release spheres

The first test case that I consider is the backscattering form function and scattering beampatterns from both rigid and pressure-release spheres. I obtained these by considering the limiting case of elastic spheres. The rigid sphere is obtained by letting the material properties of the elastic sphere attain very high values, while the pressure-release sphere is obtained in the limit of vanishing material properties. I now consider the backscattering form function and the bistatic beampattern from these spheres.

(i) *Backscattering form function*

The backscattered pressure from the rigid solid sphere is shown by the dashed line (- -) in Fig. 2-5. The results have been computed up to a ka value of 10, and I have therefore summed 40 orders to obtain the scattered pressure. For low frequencies, in the Rayleigh scattering regime, the scattered field is dominated by the monopole and dipole terms, which have the same dependence on ka. In the high-frequency or Kirchoff-geometric acoustics scattering regime, the scattered field approaches the constant value of 1, i.e., the reflection coefficient from a plane rigid boundary. In the intermediate frequency range, we observe the characteristic oscillatory behavior of the scattered field. This is the regime where the resonances of the sphere characterize the scattered field. As discussed in [20], this phenomena can be interpreted in terms of

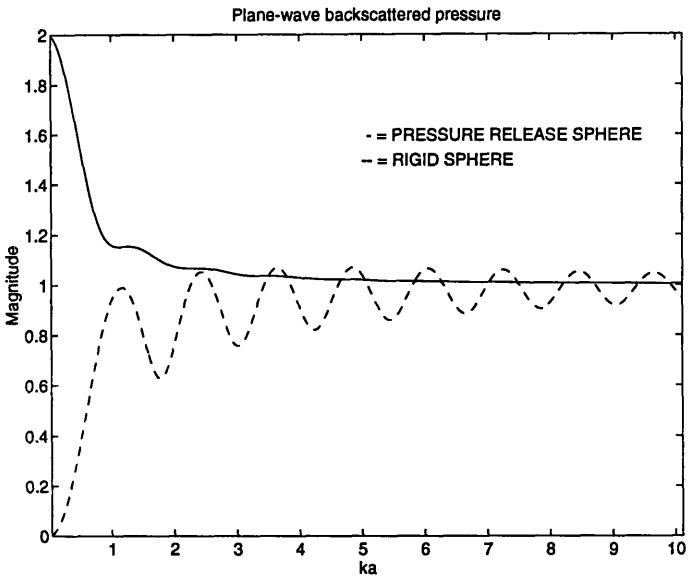

Figure 2-5: Backscattered pressure from rigid (denoted by the dashed line (- -)) and pressure-release (solid line (-)) spheres computed using matrix inversion from my theoretical model. In the intermediate frequency range, the rigid sphere displays the characteristic oscillatory behavior due to interference between the specular and creeping waves.

creeping waves, which travel around the sphere, and then combine with the specular either destructively or constructively producing the characteristic interference pattern.

The backscattered pressure from a pressure-release sphere has also been plotted in Fig. 2-5 as the solid line (-). We observe that the scattered field reaches a maximum value at very low frequencies as the sphere essentially radiates like a monopole, and then as frequency increases, uniformly tends to the value of 1, i.e., the reflection coefficient from a plane pressure-release surface. The plot in Fig. 2-5 compares extremely well with that published in literature, for example Fig. (2a) in Ref. [31], and Fig. (11a) in Ref. [20]. Therefore, my first sanity check validates my analysis in these limiting cases of backscatter.

(ii) *Bistatic Beampattern*

Now consider the bistatic scattering beampattern from the rigid and pressure-release spheres for a non-dimensional frequency of $ka = 0.2$ as shown in Fig. 2-6. The figure on the left for the rigid sphere agrees extremely well with that presented in, for

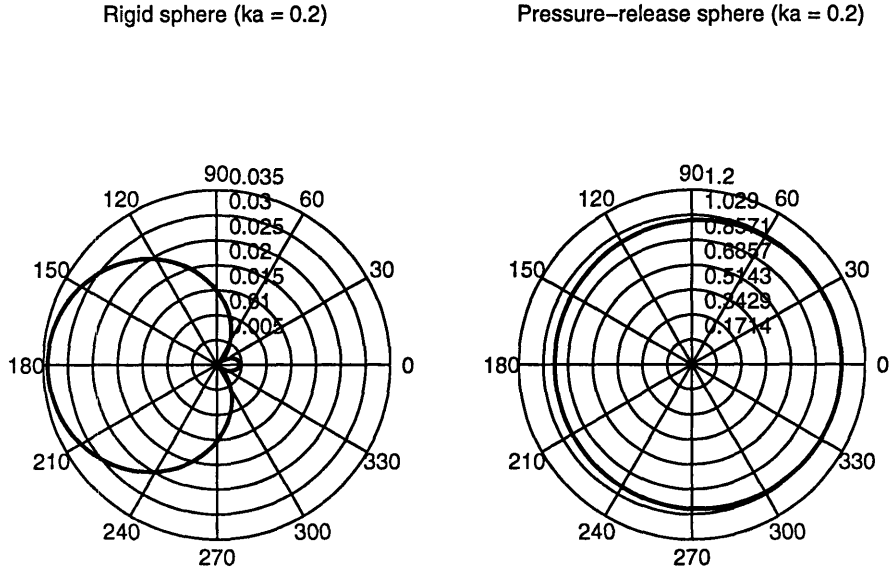

Figure 2-6: Bistatic scattering beampattern from rigid and pressure-release spheres for $ka = 0.2$. The acoustic wave is incident from the left, and therefore backscatter is to the left and forward to the right. The contour levels are plotted in terms of linear magnitude.

example, Fig. (6.2.6) of Ref. [40]. At this low frequency, when the acoustic wavelength is much larger than the dimension of the sphere, we get very high backscatter and very low forward scatter. This is due to the fact that the total scattered field consist of a monopole and dipole term, in fact the directivity being of the form $(1.5\cos\phi - 1.0)$. On the other hand, the pressure-release sphere behaves more like a monopole, with alternating compressions and expansions of the spherical surface, thereby re-radiating a spherical wave back into the acoustic medium.

Ice sphere

The next example I consider is that of scattering from a solid elastic ice sphere. Fig. 2-7 shows the form function computed from Faran's [30] and Hickling's [31] results, and my formulation for the free sphere. We observe that the two plots are in excellent agreement in both magnitude and location of the peaks and valleys in the form function, thereby validating my analysis once again. It is interesting to note that when I plotted the form function using the material properties of ice given by Hickling [31],

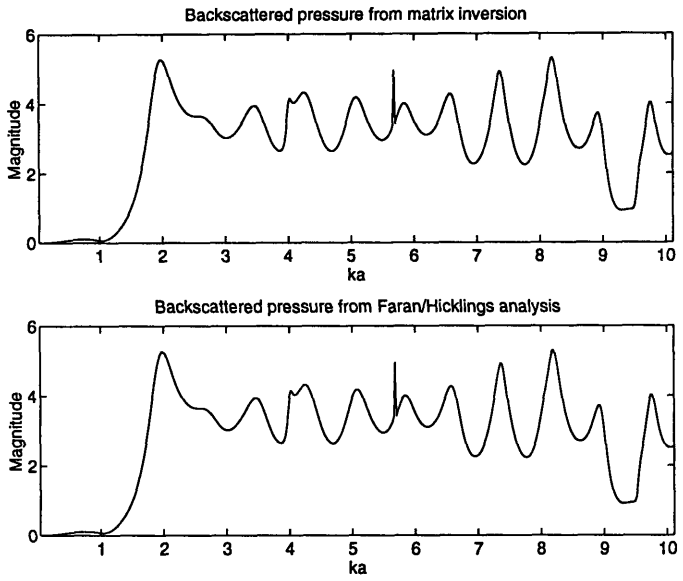

Figure 2-7: Backscattered pressure from an ice sphere computed using coupling formulation (upper figure) and from Faran/Hickling's analysis (lower figure). The levels are in terms of linear magnitude.

the form function looks different compared to that presented here. This is especially noticeable in reference to the sharp peak at $ka \sim 5.7$. My analysis suggests that it corresponds to the contribution due to the Rayleigh wave which is supersonic with respect to the fluid with the material properties used by me, while it is subsonic with the material properties used in his analysis.

Coupling formulation with vanishing plate thickness

Finally, I present the case when the thickness of the attached plate in my coupling formulation is vanishingly small. Then, the contributions from the coupling forces and bending moment must also be vanishingly small, and the plate-sphere coupled model should reduce to that of the free sphere only. Therefore, letting the radius of the sphere remain 10 m as before, and choosing a plate of thickness 2 mm, I obtain the results shown in Fig. 2-8. The figure shows the backscattered pressure due to the free submerged sphere only, as well as the total sum of contributions from all the attachment forces and moments. As expected, the contributions from the coupling forces and moments are negligibly small compared to that from the free sphere, in

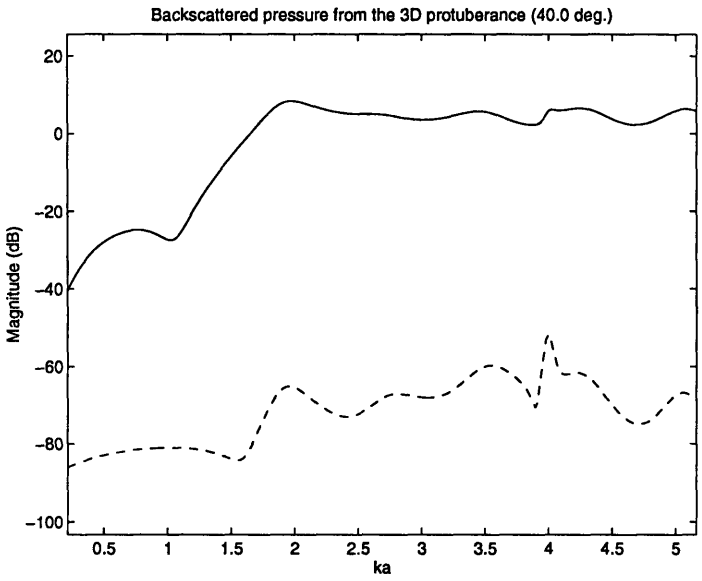

Figure 2-8: Validation of analytical model. Backscattered pressure from the three-dimensional protuberance for source located at $\theta_0 = 130.0°$, and in the limit of vanishing plate thickness. The dashed line (- -) represents the sum of the contributions from the coupling forces and bending moment while the solid line (-) represents the backscattered pressure from the fully submerged sphere only.

fact lower by about 50 - 60 dB. Similar results are obtained by making the plate very soft by considering the limit of vanishing wave speeds and material density. These limiting benchmark solutions, therefore, once again validate my coupling formulation.

2.5.2 Examples

I now return to the three-dimensional scattering problem and present some results from my analytical formulation. The results presented here basically consist of three main parts. In the first part, I shall compute all the kinematic and dynamic quantities associated with the interaction between the plate and the sphere for a fixed angle of incidence. The second part illustrates the dependence of the excitation of the elastic modes in the plate for varying angles of incidence of the acoustic field. Finally, I discuss the three-dimensional scattering patterns from the plate-sphere coupled model.

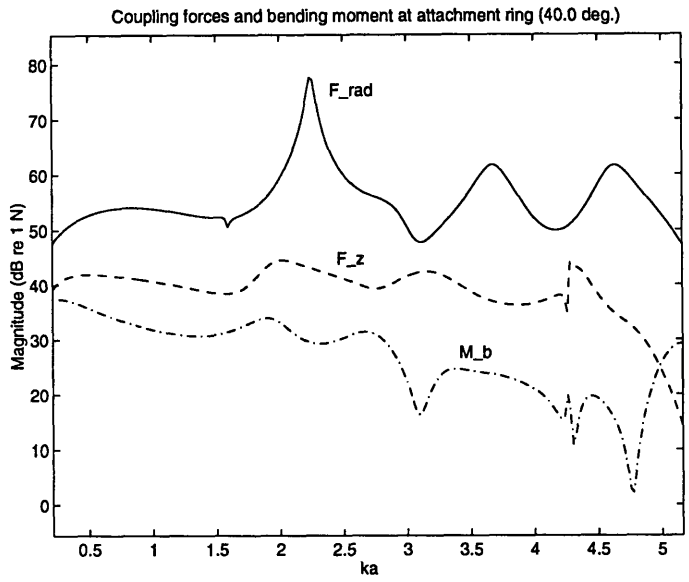

Figure 2-9: Coupling forces and bending moment at the attachment ring for $\theta_0 = 130.0^o$. The solid line (-) represents f_R, the dashed line (- -) f_z, while the dashed-dotted line (-.) denotes M_b (re 1 Nm).

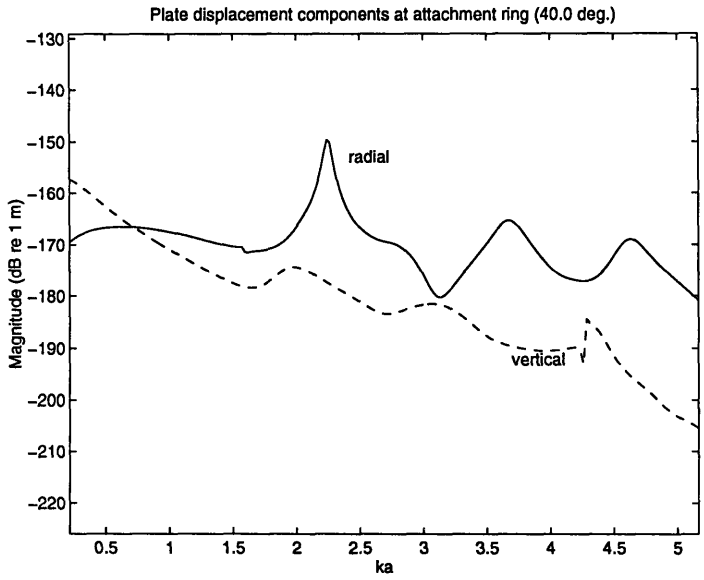

Figure 2-10: Plate displacement components at attachment ring for $\theta_0 = 130.0^o$. The solid line (-) represents u_R and the dashed line (- -) represents u_z. u_φ is negligible and is not shown here.

Source at $\theta_0 = 130.0^o$ (40.0^o grazing)

Fig. 2-9 shows the coupling forces and bending moment at the point ($\varphi = 0.0^o$) on the attachment ring ($\gamma = 90.0^o$) as a function of the non-dimensional frequency parameter ka, where k is the acoustic wavelength in water and a is the radius of the sphere. Examination of the figure reveals that the radial in-plane force f_R is the more strongly excited compared to the vertical force f_z and the bending moment M_b, and has resonances at ka values of 2.3, 3.7 and 4.6. The azimuthal force f_φ has a node at this point, and therefore its magnitude is extremely small and does not appear in this plot. The amplitude of excitation of the in-plane forces is much higher than the vertical force f_z and the bending moment M_b as the attached plate primarily constrains the motions of the sphere in the horizontal plane at the attachment ring. As a result, the radiated field due to the interaction forces should be dominated by contributions from forces in the φ and R directions. That this is the case will become evident from my analysis that I will present a little later.

The displacement components of the plate at the same point on the attachment ring are shown in Fig. 2-10. Once again we observe the resonances in the radial displacement component v_R at ka of 2.3, 3.7 and 4.6. At low frequencies ($ka < 0.6$) the out-of-plane displacements are higher in magnitude than the in-plane displacements. However, as the impedance of the plate to vertical motions increases with frequency, we observe the roll-off in amplitude of the out-of-plane motions. Also, since the flexural waves are subsonic in this frequency regime, they do not couple to the surrounding fluid and only produce an evanescent field in the fluid in the vicinity of the plate. Once again, the azimuthal displacement component v_φ has a node at this location and therefore does not appear in this plot.

To develop a better understanding of the spatial structure of the coupling forces and displacements at the junction, I also computed these quantities for select frequencies at the attachment ring. Fig. 2-11 shows the plate displacement components and the coupling forces as a function of the azimuthal angle φ on the attachment circle for ka = 1.0. This figure clearly illustrates the nodal structure of the azimuthal displacement

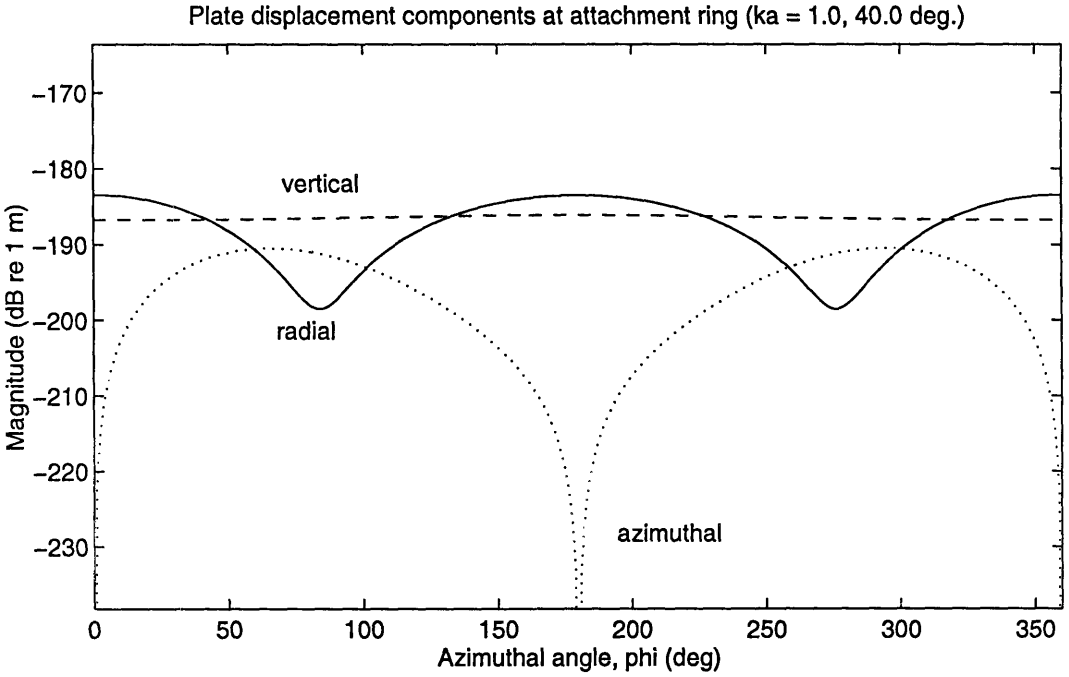

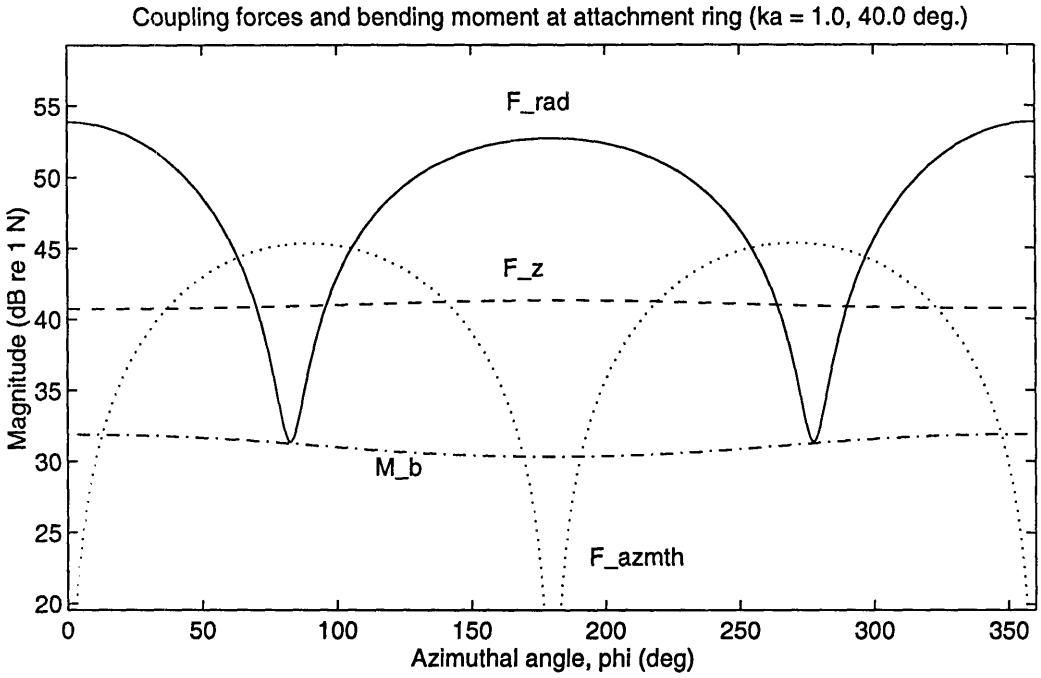

Figure 2-11: Plate kinematics at the attachment ring for $\theta_0 = 130.0°$, $ka = 1.0$. The upper figure shows the plate displacement components at the attachment ring, with the solid line (-) representing v_R, the dotted line ($\cdots$) denoting v_φ, the dashed line (- -) w. The lower figure shows the coupling forces and bending moment at the attachment ring, with the solid line (-) representing f_R, the dotted line ($\cdots$) denoting f_φ, the dashed line (- -) f_z, and the dashed-dotted (- .) denoting M_b (re 1 Nm).

component v_φ which is antisymmetric with respect to the coordinate φ, whereas the radial displacement component v_R is symmetric. While v_φ displays deep nulls at the nodes of the displacement fields, the nulls in v_R are less prominent. Also note that at 0° azimuth, the radial displacement component is about 3 dB higher than the vertical displacement component w. However, if we were to compute the average the displacements at the junction, we would observe that the two displacements are of the same order of magnitude. The out-of-plane displacement due to the flexural wave is more or less constant around the circumference of the junction.

The coupling forces and bending moment are shown in the lower part of Fig. 2-11. The structure of these dynamic quantities closely resembles that of the kinematic quantities plotted in the upper part of the figure. This is not surprising since there is a direct relationship between $\mathbf{u}_{p,c}$ and $\mathbf{f}_p$ via the influence matrix $\mathbf{Z}_p$. The magnitudes of excitation of the vertical force f_z is on average 5-7 dB lower than the in-plane force f_R. Also, observe that the magnitude M_b is about 10 dB lower than f_R suggesting that the contributions to the radiated field due to M_b will be less significant compared to that due to f_R.

Fig. 2-12 shows the plate displacements and forces around the circumference of the junction for a higher frequency, i.e., $ka = 2.3$. Note that this frequency corresponds to the first resonance observed in the plate displacement components in Fig. 2-10. Consistent with our observations there, we notice that the in-plane displacements are significantly higher (by about 20 dB) than the vertical displacement component w. This is due to the fact that at this frequency, the excitation forces strongly excite the compressional resonances of the sphere. The radial motion of the compressional mode then, in turn, couples to the in-plane motions of the plate. Also shown in the lower part of the figure are the forces and bending moment at the ring. Observe that the difference in magnitude of excitation of the radial force f_R is 30 dB higher than f_z as compared to 15 dB in Fig. 2-11 at $\varphi = 0.0^\circ$. Also, as in the case of $ka = 1.0$, we observe that the amplitude of excitation of the bending moment is 10 dB lower than the vertical force f_z. The interesting point to note here is that as we move up in frequency,

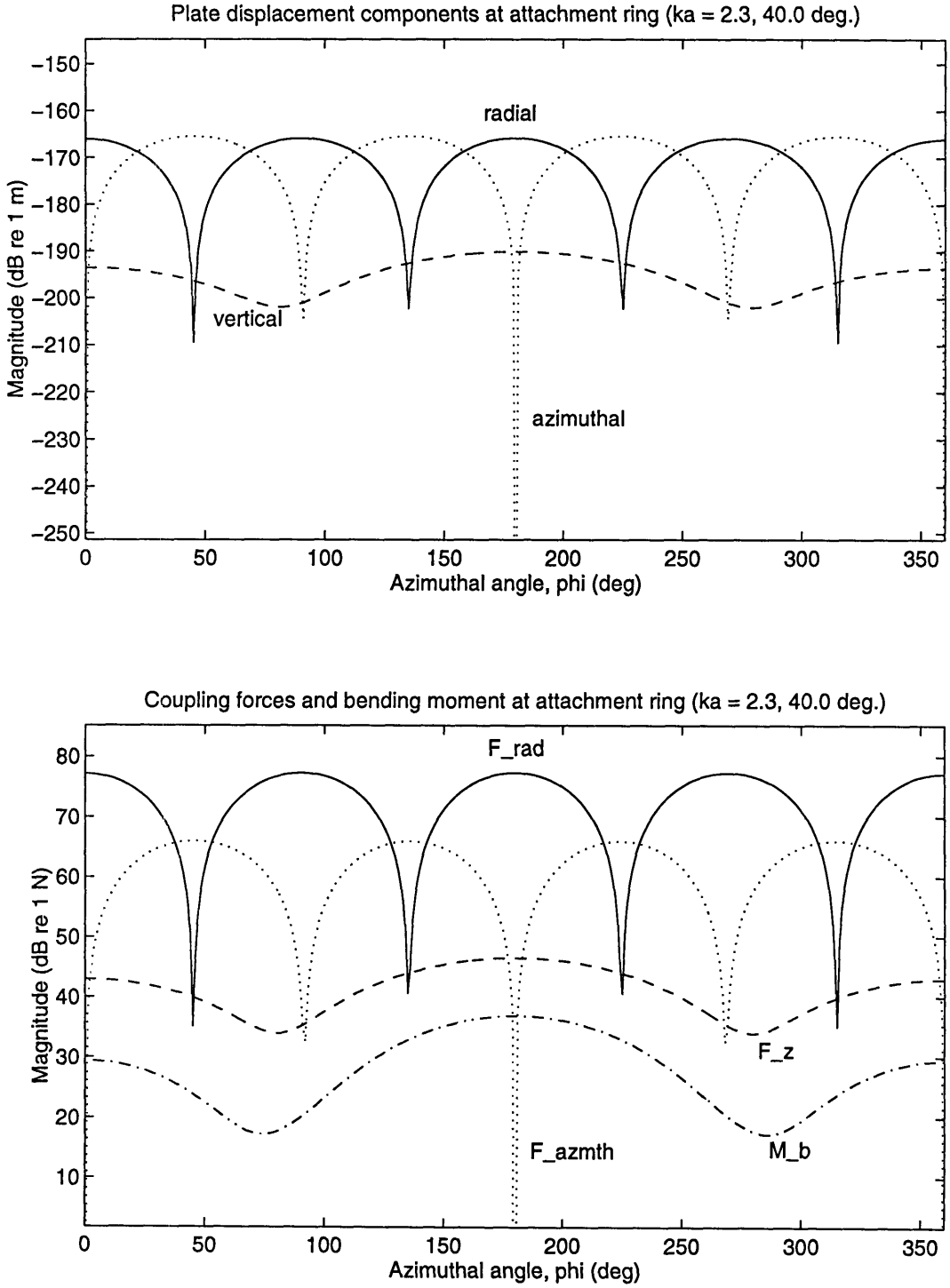

Figure 2-12: Plate kinematics at the attachment ring for $\theta_0 = 130.0^o$, $ka = 2.3$. The upper figure shows the plate displacement components at the attachment ring, with the solid line (-) representing v_R, the dotted line ($\cdots$) denoting v_φ, the dashed line (- -) w. The lower figure shows the coupling forces and bending moment at the attachment ring, with the solid line (-) representing f_R, the dotted line ($\cdots$) denoting f_φ, the dashed line (- -) f_z, and the dashed-dotted (- .) denoting M_b (re 1 Nm).

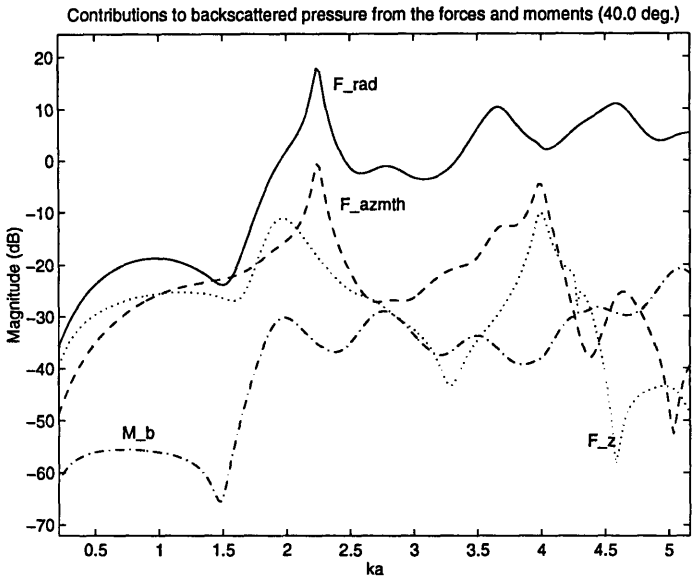

Figure 2-13: Individual contributions to backscattered pressure from the coupling forces and bending moment. The solid line (-) represents the contribution due to f_R, the dashed line (- -) due to f_φ, while the dotted line ($\cdots$) corresponds to f_z, and the dashed-dotted line (-.) represents that due to M_b.

the number of nodes in the displacement components increase. This is understandable since for higher frequencies, the contributions from the higher azimuthal orders m become more dominant.

Thus far I have concentrated my analysis on the kinematics and dynamics of the attachment junction. It is also instructive to consider the relative importance of these forces and displacements to the total radiated pressure. Therefore, in Fig. 2-13 I have plotted the individual contributions to the backscattered pressure resulting from these excitations. The figure reveals that below ka of 2.0, the contributions from all the forces are comparable in magnitude. However, above a ka value of 2, the dominant contribution arises from the in-plane forces (f_R and f_φ), and are higher than that from the the vertical force (f_z). This is to be expected since the attached plate primarily constrains the in-plane motions of the sphere. This is because the impedance of the plate with respect to in-plane motions is much higher than the out-of-plane motions. Also, note that the contribution from the bending moment is the weakest being about 30 dB lower than the radial force f_R at most frequencies.

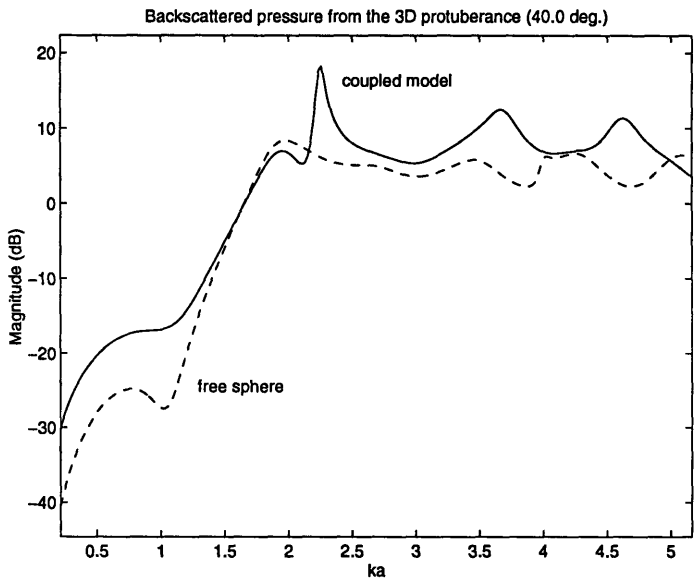

Figure 2-14: Backscattered pressure from the three-dimensional protuberance for source located at $\theta_0 = 130.0°$. The continuous line (-) represents the total backscattered pressure from the coupled model while the dashed line (- -) represents the backscattered pressure from the fully submerged sphere only.

Fig. 2-14 shows the total backscattered pressure from the three-dimensional protuberance, the solid line being the sum of the contributions from the free submerged sphere and all the forces and the bending moment, whereas the background field due to the fully submerged elastic sphere only is represented by the dashed line. As the radial force is the dominant contributor, we observe its characteristic structure in the total backscattered field. Note that the attachment of the plate to the sphere results in a modulation of the form function of the free sphere by the kinematics of the sphere at the attachment ring. The resonance structure is due to standing waves set up inside the sphere when excited by the coupling forces and bending moment. The location of the peaks agrees with the values computed by setting $\Delta_0 = 0$ in eqn. (B.5). An important conclusion from this figure is that the attachment of the plate to the sphere is a frequency selective process and is manifested in the scattered field at certain frequencies only.

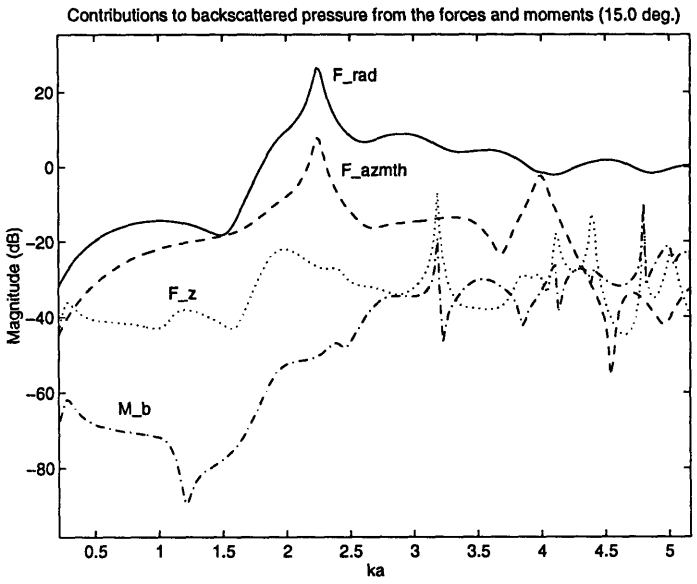

Figure 2-15: Individual contributions to backscattered pressure from the coupling forces and bending moment for $\theta_0 = 105.0°$. The solid line (-) represents the contribution due to f_R, the dashed line (- -) due to f_φ, while the dotted line (···) corresponds to f_z, and the dashed-dotted line (-.) represents that due to M_b.

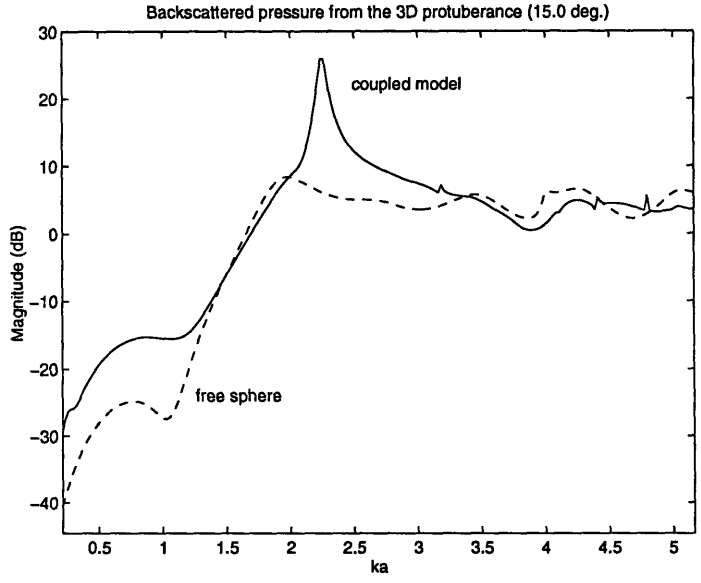

Figure 2-16: Backscattered pressure from the three-dimensional protuberance for source located at $\theta_0 = 105.0°$. The continuous line (-) represents the backscattered pressure from the coupled model while the dashed line (- -) represents the backscattered pressure from the fully submerged sphere only.

Source at $\theta_0 = 105.0^o$ (15.0^o grazing)

Fig. 2-15 shows the individual contributions to the backscattered field from the coupling forces and bending moment for a shallower grazing angle of incidence ($\theta_0 = 105.0^o$ or 15.0^o grazing). A closer comparison of these results with those presented earlier in Fig. 2-13 for $\theta_0 = 130.0^o$ reveals that the qualitative nature of the contributions from the coupling forces is not altered by changing the angle of incidence. This result is reinforced when we plot the total backscattered field as shown in Fig. 2-16. We observe that for small frequencies ($ka < 3.0$) there is almost no difference between the results for the two different grazing angles of incidence. At higher frequencies, the resonances that we observed in the 40.0^o incidence case are not as prominent here. The conclusion then is that for low frequencies the backscattered pressure is not qualitatively affected by changing the angle of incidence. However, there is a caveat to be noted here. As my results in the next section will demonstrate, although the total backscattered pressure remains almost unchanged, the physics of the interaction between the plate and sphere are significantly modified.

Plate-sphere interaction dynamics as a function of grazing angle of incidence

It is informative to consider the dynamics of the attachment junction as a function of grazing angle of incidence. This will illustrate the relative importance of the different elastic modes that get excited in the plate for different angles of incidence. Simultaneously, this will also demonstrate the relative importance of the elastic modes excited in the plate via direct acoustic excitation and those due to the coupling forces and moments.

The displacement fields of an infinite, fluid loaded plate excited by a point monopole source in the fluid have been previously investigated in detail by, for example, Langley [18]. Langley computed the in-plane and out-of-plane displacement fields for the case of the point source positioned axisymmetrically, i.e., there is no dependence on

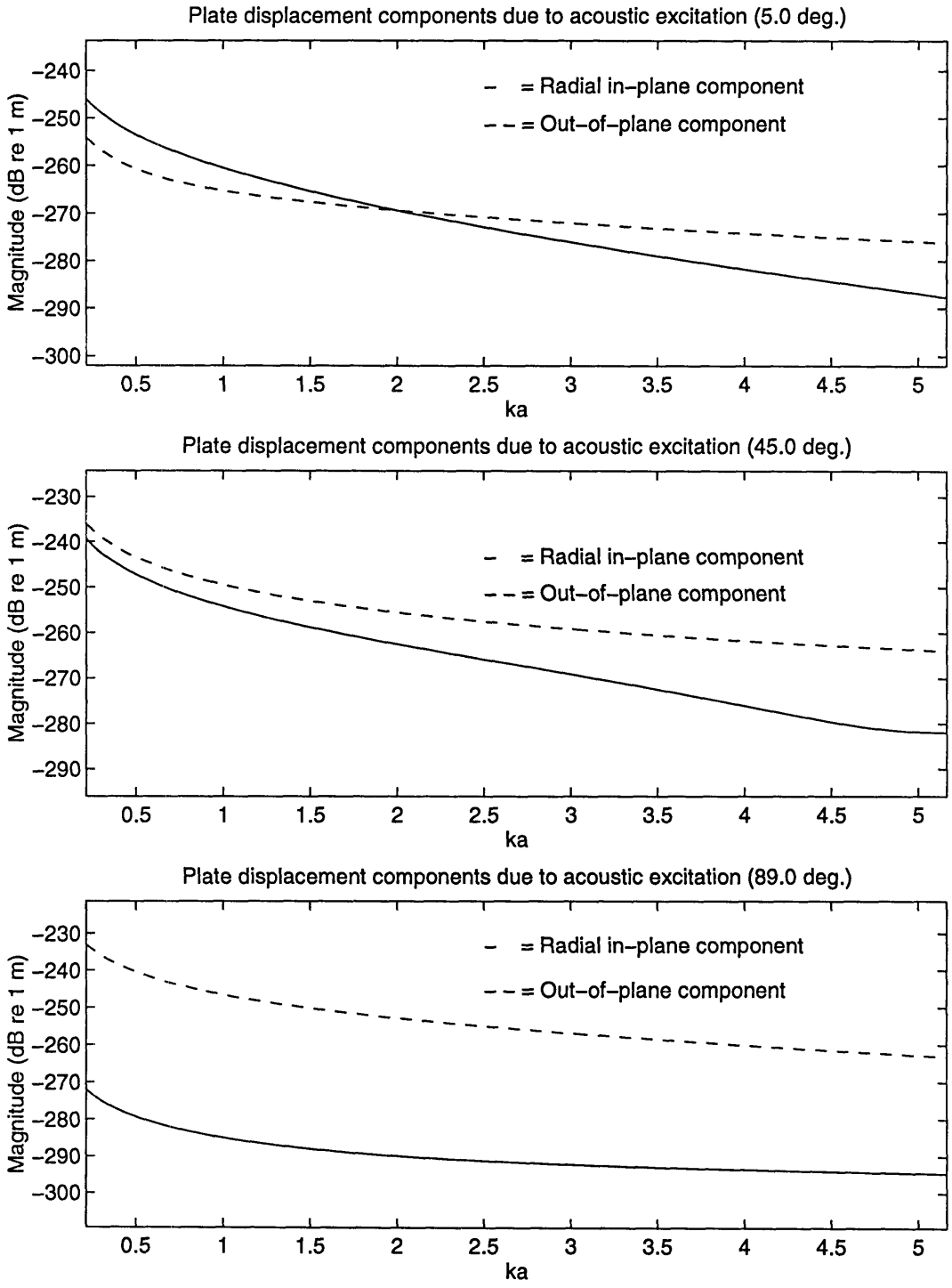

Figure 2-17: Plate displacement components at attachment ring due to acoustic excitation for $\theta_0 = 95.0°$, $135.0°$, and $179.0°$. The solid line (-) represents v_R and the dashed line (- -) denotes w. This figure illustrates that the displacement components at the attachment ring due to the acoustically excited modes is negligible compared to those due to coupling forces (compare with Fig. 2-18).

the azimuthal coordinate φ. Using eqns. (36) and (37) from Langley [18], I plot the plate displacement components at the point $\varphi = 0.0^o$ on the attachment ring for three different angles of incidence, $\theta_0 = 5.0^o$, 45.0^o, and 89.0^o grazing, as shown in Fig. 2-17. Note that these results are valid for the point monopole source positioned in the far field of the plate. Also, I have normalized the frequency axis by the radius a of the sphere.

Due to Poisson's effect, the compressional modes have a vertical displacement component in addition to the in-plane component. The flexural waves are subsonic in this frequency regime, and are therefore very weakly excited. For our plate parameters, the critical grazing angle for the excitation of compressional waves in the plate roughly corresponds to $\theta_{cr} = 59.0^o$. Therefore, the compressional modes excited by the acoustic source will be observed at the attachment ring for all grazing angles θ such that $\theta_0 < 59^0$. This is evident from the figure which shows that the amplitude of the in-plane components are significantly lower for the case when $\theta_0 = 89.0^o$. The point to be made from this plot is that the typical magnitudes of the displacement components for this frequency range, and over all grazing angles, is between -240 dB to -280 dB.

In Fig. 2-18 I have plotted the plate displacement components at the point $\varphi = 0.0^o$ on the attachment ring for three different angles of incidence, θ_0 - 5.0^o, 45.0^o, and 90.0^o grazing. Note that the magnitudes here typically range from -160 dB to -200 dB. Comparing these magnitudes for each grazing angle to those plotted in Fig. 2-17, we observe that the displacements due to acoustic excitation are more than 80 dB below those due to the coupling forces and moments at the attachment ring. Therefore, the approximation I made in obtaining eqn. (2.28) is clearly justified, and the resulting errors are almost negligible.

Now consider the displacements due to the interaction forces in the low frequency regime $ka < 1.5$, or in terms of frequency $f < 35Hz$, The figure shows that for very shallow grazing angles, the excitation of the in-plane motion in the plate is higher than the vertical displacement. This makes intuitive sense as at these low values of grazing angles, the primary action of the incident acoustic field is to cause a lateral motion of

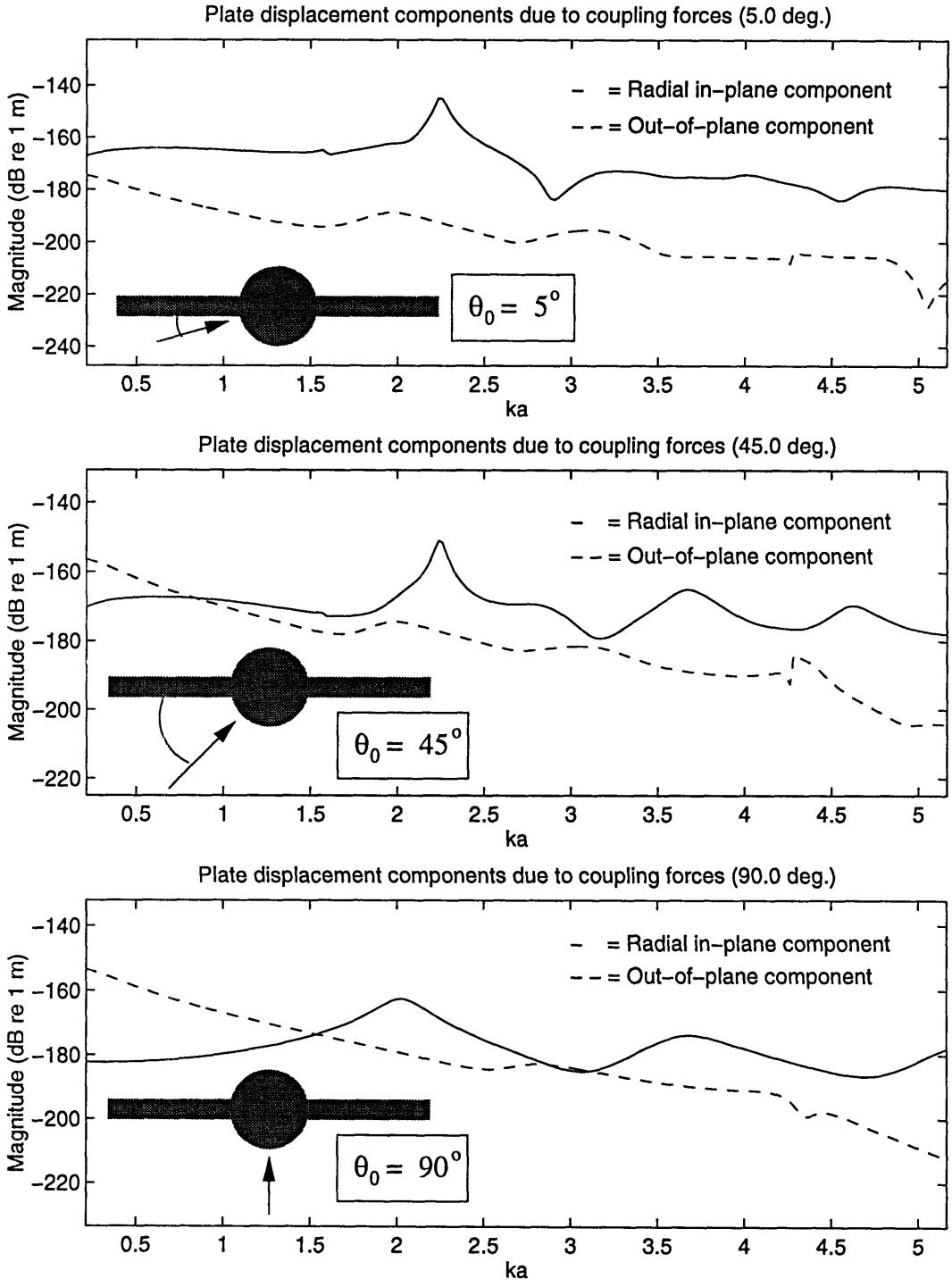

Figure 2-18: Plate displacement components at attachment ring due to coupling forces for $\theta_0 = 95.0°$, $135.0°$, and $180.0°$. The solid line (-) represents v_R and the dashed line (- -) represents w. v_φ is negligible and is not shown here. The figures illustrate that in the low frequency regime, the relative excitations of the in-plane and out-of-plane motions vary with angle of incidence.

the sphere in the horizontal plane. This translational motion then, in turn, excites the plate horizontally, thereby producing higher deformations in the in-plane direction as opposed to the vertical motions. As we progress to higher grazing angles, the flexural motions start becoming comparable to the in-plane motions. At 90.0^o grazing, i.e., with the source illuminating the plate-sphere coupled structure from directly below, we observe large amplitudes of displacement in the vertical direction. These large vertical displacements are due to the incident acoustic field which forces the sphere to oscillate predominantly in the vertical direction. However, we also observe the roll-off in the vertical displacements with frequency because of the enhanced flexural impedance of the elastic plate. Therefore, we conclude that the relative amplitudes of the motions of the plate in different directions are determined by the grazing angles at which the acoustic field is incident on the plate sphere junction.

A more definitive corroboration of this conclusion may be achieved by considering the distribution of energy among the various wave types excited in the elastic ice plate. An exact analysis would require the computation of stresses and strains due to each of these wave types in the plate. However, I can make a first order estimate of this energy distribution by assuming that, for example, the energy injected into the compressional mode is given by the product of radial force and radial displacement. This is not exactly correct since the radial force on the plate generates both the radial and azimuthal components of displacement. This is caused by the two dimensional nature of the plate geometry. As the plate expands in the radial direction, it must also simultaneously stretch in the azimuthal direction, i.e., the radial displacement component v_R and the strain in the azimuthal direction ϵ_φ are completely coupled. This is also evident from eqn. (2.21).

Thus, I calculate the approximate energy levels injected into the various wave types at the attachment ring, averaged over the azimuthal direction, as

$$U_{comp} = \sum_{m=-\infty}^{\infty} \frac{1}{2}\mathrm{Re}\left[\hat{f}_R \hat{v}_R^*\right] \quad , \quad U_{shear} = \sum_{m=-\infty}^{\infty} \frac{1}{2}\mathrm{Re}\left[\hat{f}_\varphi \hat{v}_\varphi^*\right] \quad ,$$

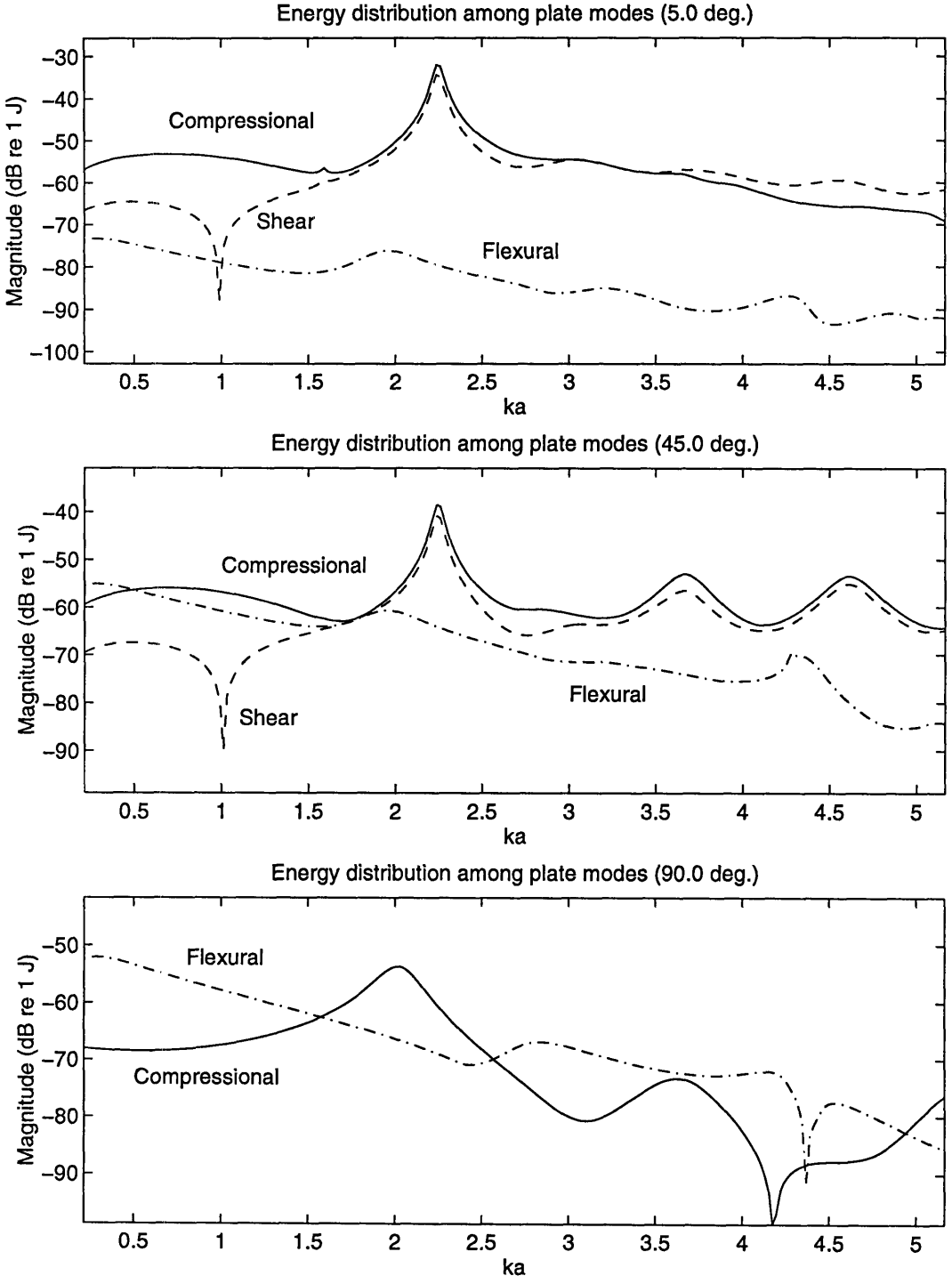

Figure 2-19: Energy distribution among the various plate modes at the attachment ring for $\theta_0 = 95.0°$, $135.0°$, and $180.0°$. The solid line (-) represents the energy in the compressional mode, the dashed line (- -) represents the energy in the shear mode, while the dashed-dotted (- .) line denotes the energy in the flexural waves. The figures illustrate that in the low frequency regime, the relative energies in the various elastic modes of the plate vary with grazing angle of incidence.

$$U_{flex} = \sum_{m=-\infty}^{\infty} \left\{ \frac{1}{2}\mathrm{Re}\left[\hat{f}_z \hat{w}^*\right] + \frac{1}{2}\mathrm{Re}\left[\hat{M}_b \frac{\partial \hat{w}^*}{\partial R}\right] \right\} \quad , \tag{2.33}$$

where "*" denotes complex conjugate. Note that the bending energy consists of contributions from both the vertical force f_z and the bending moment M_b. Consistent with our results for the displacements, we observe that the energy in the flexural waves increases with increasing angle of incidence. Once again limiting our analysis to the frequency regime $ka < 1.5$, we note that for very shallow grazing angles, the energy introduced in the in-plane motions is about 10 dB higher than in the flexural waves. At intermediate angles ($\theta_0 = 45.0^o$) the flexural and in-plane modes have comparable energy levels. Note the presence of the resonances as were observed in the plate displacement components. However, for beam incidence ($\theta_0 = 90.0^o$), the energy in the flexural mode is about 15 - 20 dB higher than the in-plane modes. At this juncture, it is also worthwhile to note that Lepage [7], who used MSP to model the rough ice water interface, observed similar differences in the energy levels between the out-of-plane and in-plane motions. In fact, for a 17 Hz plane wave incident at 10^o grazing on the rough interface, he observed the vertical energy of the antisymmetric mode to be about 5 dB higher than the energy in the horizontal motions.

Thus our analysis of the plate sphere interaction dynamics leads us to the following inference. The plate displacements and the energy levels of the various plate modes suggests that the nature of the interaction is significantly modified by varying the angle of incidence. A good indication of this effect would be noticed by computing the bistatic scattered pressure for various angles of incidence. If indeed the results show strong dependence on grazing angles, i.e., significant observables, then it should be possible to invert for these physical mechanisms from measurements of the acoustic field in the fluid medium. The subsequent analysis, where I compute the spatial scattering patterns from this protuberance, will demonstrate how strongly these observables are manifested in the scattered field.

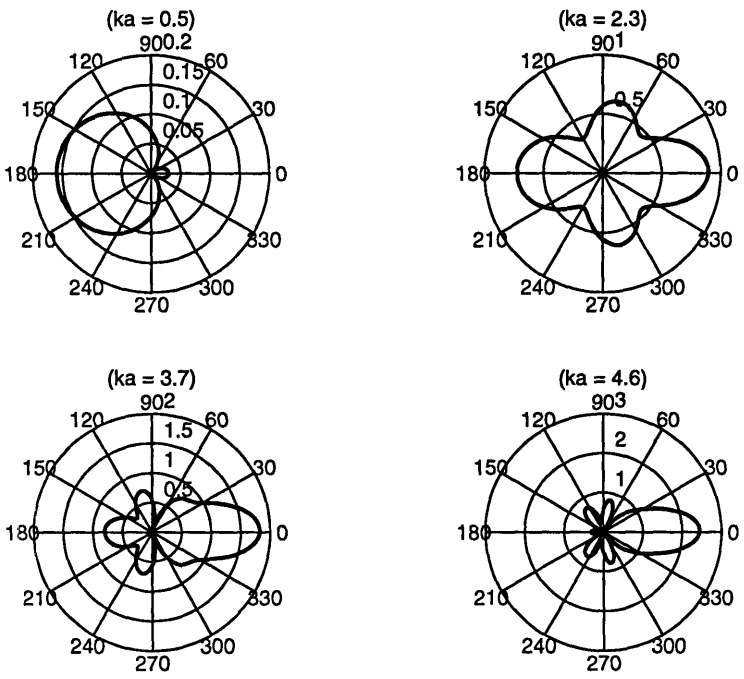

Figure 2-20: Scattering beampattern from the elastic ice sphere for ka = 0.5, 2.3, 3.7, 4.6. Backscatter is to the left and forward scatter is to the right

Spatial structure of the scattered field

As mentioned earlier, our primary interest is in the analysis of scattering in the frequency regime ($ka \sim O(1)$), which is also the frequency range for which our analysis is valid. The next step is to evaluate the bistatic scattering pattern from the protuberance. I shall compute the scattering pattern for a fixed source and receiver geometry. The source is assumed to be positioned, as before, at X = -600 m, Y = 0.0 m, Z = -500 m, i.e., a grazing angle of incidence roughly corresponding to 40.0°, while the sphere is located at the origin of the coordinate system. The receiver plane is located 500 m below the plate, i.e., at the depth corresponding to the depth of the source. I shall compute the scattering pattern at four distinct values of ka, i.e., at ka = 0.5, 2.3, 3.7, 4.6. The first frequency ka = 0.5, is a typical low frequency value, whereas the other three are the locations of the resonances of the in-plane radial motions as observed in Fig. 2-10.

Before computing the bistatic scattering patterns from the coupled geometry, it is instructive to consider the beampattern from the solid elastic sphere only at these

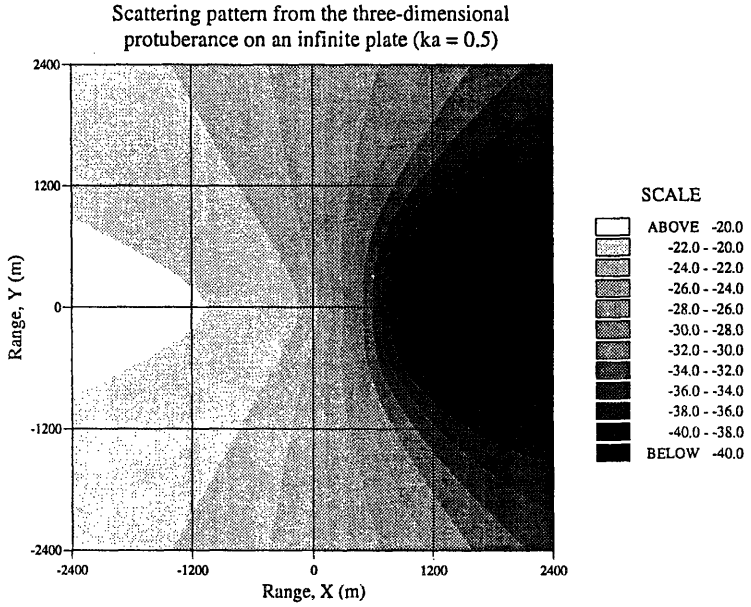

Figure 2-21: Scattering pattern from the 3D protuberance on the elastic plate for ka of 0.5. The source is located at (-600,0) and at a depth of 500 m, the receiver plane is also located at a depth of 500 m, while the spherical protuberance is centered at the origin.

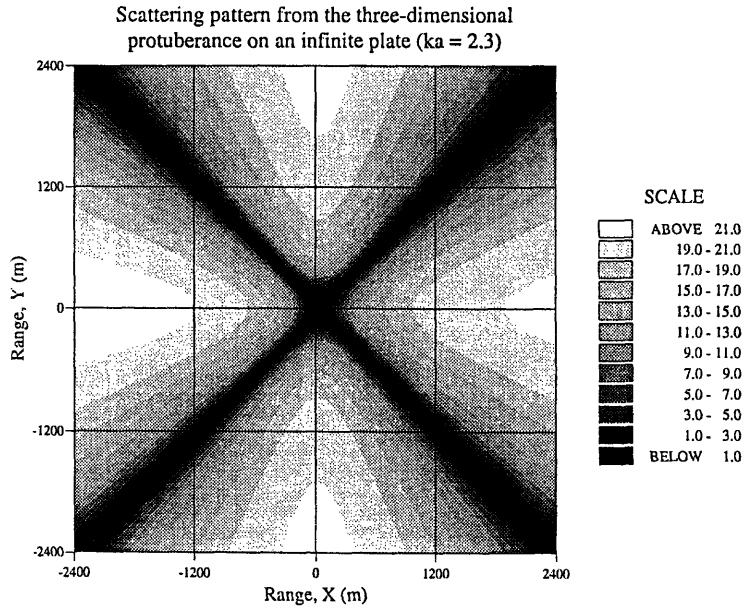

Figure 2-22: Scattering pattern from the 3D protuberance on the elastic plate for ka of 2.3. The source is located at (-600,0) and at a depth of 500 m, the receiver plane is also located at a depth of 500 m, while the spherical protuberance is centered at the origin.

frequencies. This will provide an insight into the physics of the coupled problem. Fig. 2-20 shows the bistatic beampatterns from the ice sphere for these four frequencies. From the figure, we observe that for very low frequencies ($ka = 0.5$), the behavior of the elastic sphere resembles that of a rigid sphere (compare with Fig. 2-6). As we move to a higher frequency ($ka = 2.3$), we observe that the scatter displays a very interesting pattern. Neither backscatter nor forward scatter is essentially the dominant behavior; we observe significant scatter in other directions too. This is due to the interference pattern generated by the radiation from both the compressional and shear modes in the sphere. As the frequency is increased to other higher values ($ka = 3.7, 4.6$), we begin to observe higher scatter in forward direction. This once again resembles the scattering characteristics from a rigid sphere. These scattering beampatterns should be borne in mind when trying to understand those from the coupled geometry which I shall now present.

In Fig. 2-21, I have plotted the bistatic scattering pattern for a ka value of 0.5. The pressure levels have been corrected for the transmission loss from source to scatterer, and from scatterer to receiver. As in the case of the free sphere, we observe very high scatter in the backward direction, and very low levels in the forward direction. This is due to the fact that at this frequency, the contributions from the coupling forces and bending moment are comparable with that from the direct scatter from the sphere resulting in an interference pattern that produces a deep null in the forward direction. However, as we move away from this frequency to $ka = 2.3$, as shown in Fig. 2-22, we observe deep null regions at angles of 45^o from the source-sphere axis. These nulls are caused by the interference between the compressional and shear modes in the sphere, as is also evident by the strong radial component of motion of the sphere. The predominant mode of vibration of the sphere is like a quadrupole as is also evident from Fig. 2-12. This multi-lobar nature of the radial motion of the sphere has been referred to as the *football resonance* in Ref. [41], where the sphere is expanding along the X axis, and simultaneously compressing in the Y direction, and vice versa. Note that this vibration mode exists in the free sphere too (see Fig. 2-20).

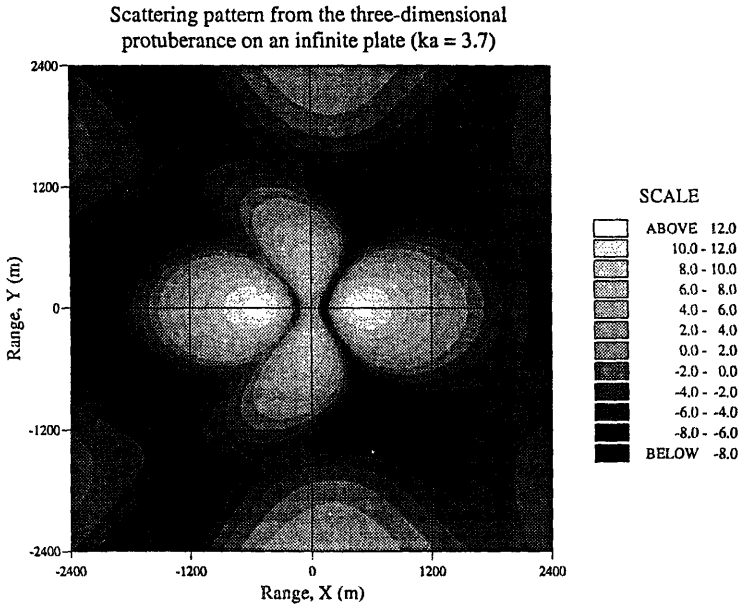

Figure 2-23: Scattering pattern from the 3D protuberance on the elastic plate for ka of 3.7. The source is located at (-600,0) and at a depth of 500 m, the receiver plane is also located at a depth of 500 m, while the spherical protuberance is centered at the origin.

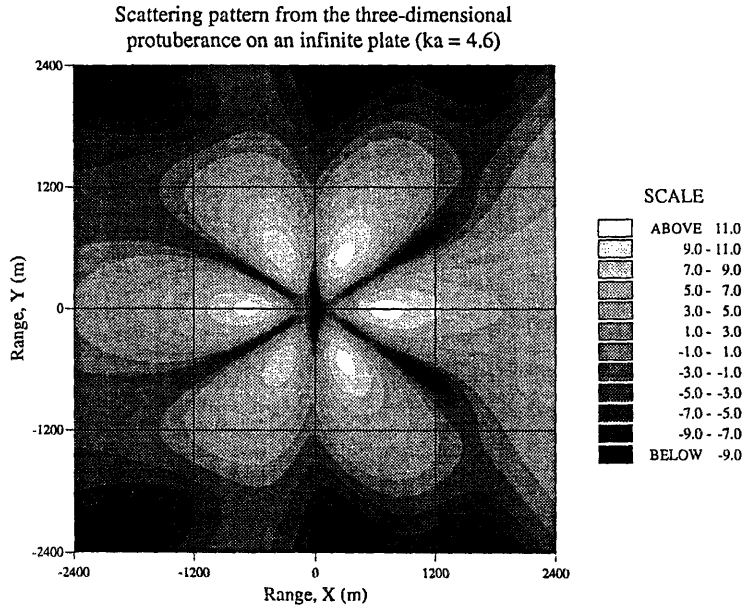

Figure 2-24: Scattering pattern from the 3D protuberance on the elastic plate for ka of 4.6. The source is located at (-600,0) and at a depth of 500 m, the receiver plane is also located at a depth of 500 m, while the spherical protuberance is centered at the origin.

Next, I compute the scattering pattern for $ka = 3.7$ as shown in Fig. 2-23. At this frequency, the acoustic wavelength is almost equal to the diameter of the sphere and causes a global resonance in the sphere. The bright spots correspond to direct forward and backscatter. Note the multi-lobar structure of the beampattern. We observe regions of deep null beyond the lobes of the beampattern. At $ka = 4.6$, as shown in Fig. 2-24, we observe a similar field except for the fact that now we have additional lobes of high scatter. This interesting lobar nature of the beampattern arises from the constructive and destructive interference between the elastic modes in the sphere. Also, at these frequencies, the primary motion of the sphere is in the horizontal plane, with constraints from the attached plate. As we go higher in frequency, we expect to see more and more lobes in the pattern. An essential outcome of these results is to the demonstrate the three-dimensional nature of the scattering pattern from our plate-sphere coupled model.

2.6 Summary

In this Chapter, I have developed an analytical solution for the analysis of scattering from a three-dimensional protuberance on a thin infinite submerged plate. The protuberance was modeled as a solid elastic sphere attached to the plate along its equatorial plane. The results from even our simplified model demonstrated the rich nature of the scattered field. Some of the essential results of this analysis are summarized below.

- Among all the forces and bending moment included in the characterization of the coupling between the sphere and the plate, in general, the excitation of the in-plane radial force f_R is the highest.

- The radial force and displacement components (f_R and v_R) are symmetric with respect to the azimuthal coordinate, whereas the azimuthal force and displacements (f_φ and v_φ) are antisymmetric.

- For shallow angles of incidence, the dominant contribution to the scattered field arises from the in-plane forces as the attached plate primarily restrains the lateral motion of the sphere. With increase in frequency, the contributions due to the out-of-plane forces, and therefore the flexural waves in the plate, are higher than the in-plane modes of the plate. Similar observations were made by Lepage [7] who showed that flexural waves play an important role in the estimation of scattering loss in the Arctic ice environment. On another note, the contributions from the bending moment are always smaller than the the vertical force, and could therefore be ignored in the analysis.

- The presence of the plate is manifested in the scattered field in a frequency selective manner corresponding to the resonances of the sphere excited by the coupling forces.

- In the low frequency regime ($ka < 1.5$), the relative magnitudes of the plate displacement components depends on the grazing angle of incidence θ_0. As the grazing angle is increased to beam incidence, the excitation of flexural waves in the plate becomes increasingly predominant. However, with increasing frequency there is a gradual roll-off in the amplitudes of excitation of the flexural waves.

- The spatial structure of the scattered field consists of a multi-lobar pattern, with higher number of lobes with increasing frequency.

- The most significant point to be noted here is that unlike a 2D analysis, the 3D analysis that I have presented here allows the inclusion of horizontally polarized shear (SH) modes. Lepage [7] has shown that these play a role in the low-frequency loss observed in the Arctic ice propagation environment. The results of my analysis here reiterate their importance in 3D scattering scenarios. I demonstrated that the contributions from these modes can be significant, which therefore necessitates their inclusion in any realistic model of the three-dimensional scattering scenario.

In Chapter 5, I will draw upon my analysis here, and make comparisons with results from experimental data, where I shall evaluate scattering from a discrete protuberance under the Arctic ice sheet. Although the explicit analytical solution presented here is for an idealized environmental model, I will show how this analysis may be exploited to construct a model for the real scattering scenario.

Chapter 3

Reverberation Experiments

3.1 Overview

In the previous Chapter, I formulated an analytical model which I will use to compare with results from experimental data. The following two Chapters discuss some issues related to the processing of data gathered from real field experiments in the Arctic Ocean. As with any real experimental data set, some amount of data conditioning needs to be undertaken before any estimates can be made of quantities of interest. Thus, I have divided the analysis of the experimental data into two Chapters. In Chapter 3, I conduct a preliminary analysis of the raw reverberation data, and discuss some data conditioning methodologies I developed to make the data amenable to more detailed analysis. I discuss issues related to the uncertainty in source position and receiver array locations. This is critical as all subsequent estimates that I make will depend on whether I have the correct positions of the source and receivers. In Chapter 4, I shall set up the data analysis as a global parameter estimation problem, and make some global estimates of the scattering characteristics of the rough ice.

3.2 The CEAREX Experiments

The Coordinated Eastern Arctic Experiments (CEAREX 89) were sponsored by the Office of Naval Research (ONR), and jointly conducted by the scientists of Massachusetts Institute of Technology (MIT), Woods Hole Oceanographic Institute (WHOI), and the Naval Research Laboratory (NRL). These experiments were conducted in the Norwegian-Iceland Sea in an area northeast of Greenland. Various experiments were carried out each with different objectives. Some measured long range propagation while others monitored the sources of ambient noise. Of particular interest to us, are the short-range reverberation experiments that were carried out in the afternoon of 15th of April between 13:26 and 14:52 hours local time. The sources used in these experiments were 1.8 *lb* SUS charges with nominal detonation depths of 800 *feet* or 244 m, and set off at an approximate distance of 250 m from the apex of the crossed horizontal hydrophone array. Five shots were fired at intervals of 15 minutes, and only the data from four of these was available to us for subsequent processing.

Fig. 3-1 shows a schematic of the layout of the acoustics camp (A-camp) during the CEAREX experiments. The camp was situated on a circular floe about 650 m in diameter as depicted by the circular jagged boundary in Fig. 3-1. The geographical *North* points upwards and *East* points to the right. The scale is roughly 1 cm = 50 m. The acoustics hut is located near the center of the camp floe which is also the apex of the horizontal hydrophone array. The main camp is located about 300 m due *North*. Also seen in the pictorial representation, about 250 m *North* and 60 m *East* of the apex of the array, is Wiebe's biology hydrohole through which the SUS charges for the reverberation experiments were dropped. Aerial pictures of the camp revealed that the area around the camp had a rough topography.

3.3 Receiver Array Geometry

Two sets of arrays were deployed during these reverberation experiments. The first consisted of a crossed horizontal hydrophone array with unequally spaced receivers

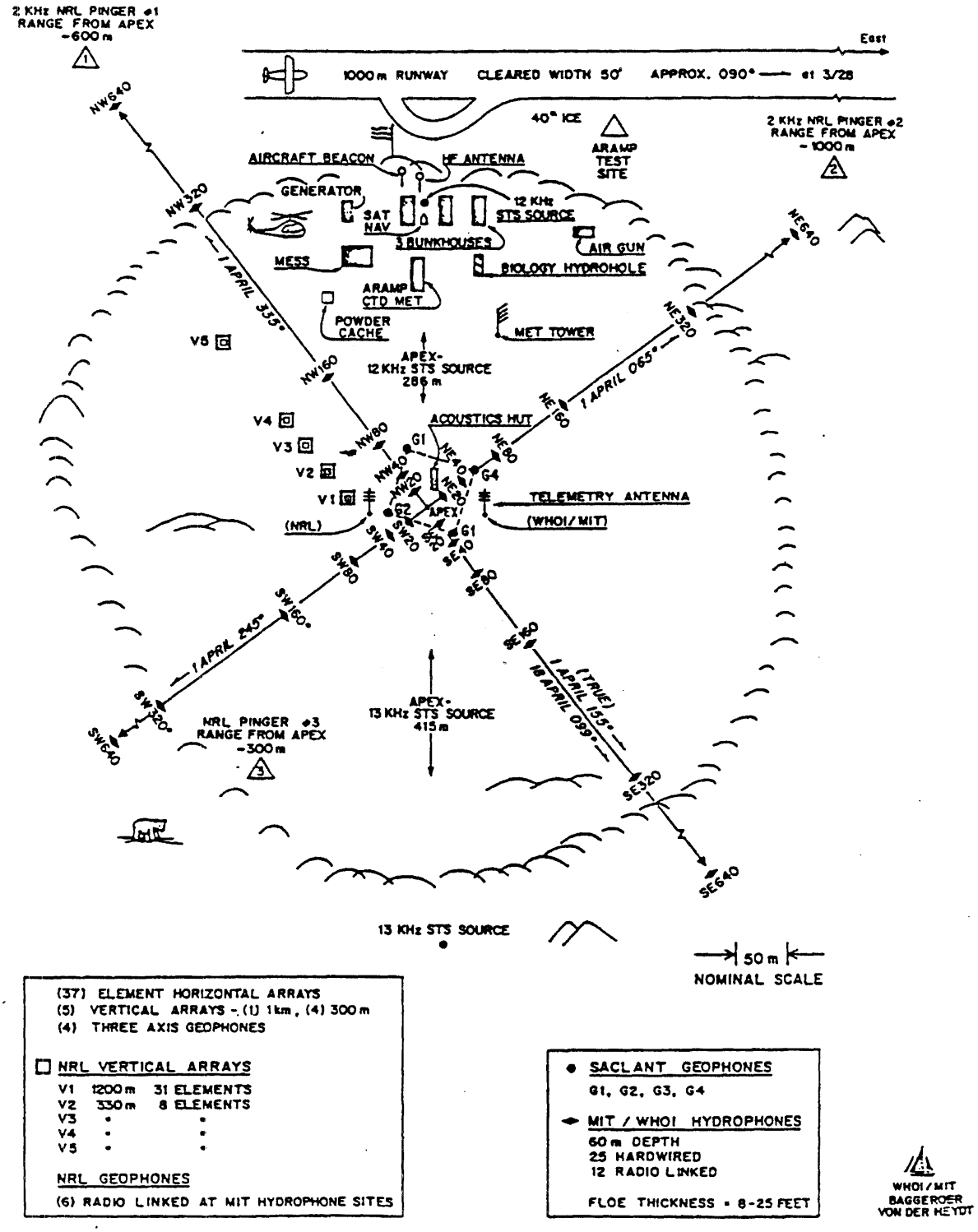

Figure 3-1: CEAREX Acoustics Camp Layout.

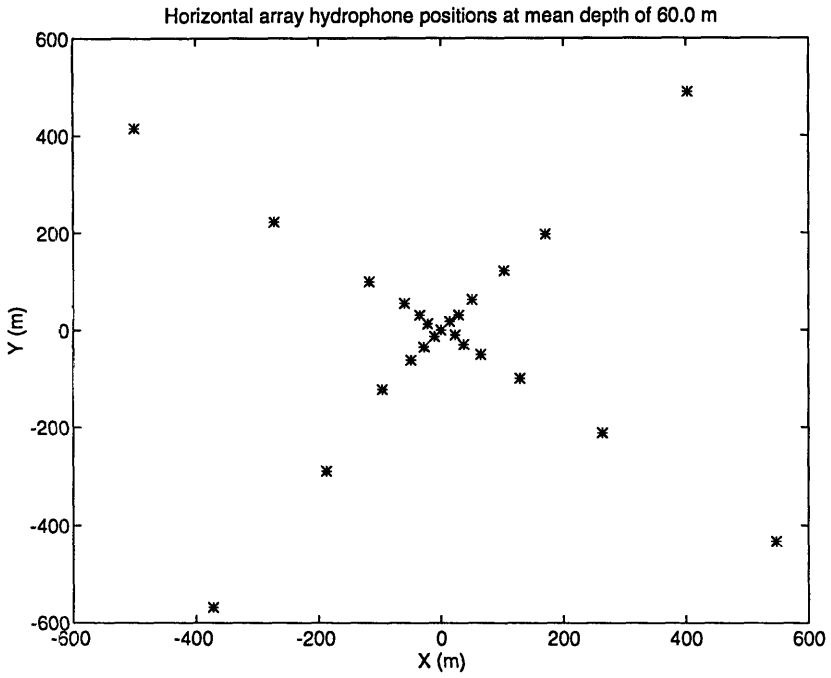

Figure 3-2: Horizontal crossed array sensor positions with the X axis pointing towards *East* and the Y axis pointing *North*.

(Mills' Cross), located at nominal depths of 60 m, and was monitored by MIT/WHOI. The second receiver array system which was deployed by NRL consisted of one long ($\sim$ 1200 m) and four short ($\sim$ 330 m) vertical arrays. Moreover, these two sets of arrays were connected to different data acquisition systems. The MIT/WHOI data recording system acquired the digital data at a sampling rate of 1 kHz, while the NRL data acquisition system recorded the data at a sampling frequency of 689.0625 Hz.

3.3.1 Horizontal Array

The crossed horizontal hydrophone array consisted of 25 logarithmically spaced hydrophones distributed along the two legs of the array as shown in Fig. 3-2. The hydrophones were placed at nominal distances of 20 m, 40 m, and so on up to 640 m from the apex of the array. The Northwest-Southeast (NW-SE) and Northeast-Southwest (NE-SW) legs were thus approximately 1280 m in length. The positions of the hydrophones on the horizontal array were monitored in real time via an acoustic Sensor Tracking System (STS). Six high frequency pingers were deployed at cali-

brated positions, and periodic travel time measurements from these to the various hydrophones were used in a simulating annealing algorithm to estimate sensor positions [42]. All the hydrophones recorded very high quality data, and therefore I was able to use all of them in our analysis. Table C.1 in Appendix C lists the positions of the horizontal array sensors that I used in all my analysis.

3.3.2 Vertical Line Arrays

One long and four short vertical line arrays were deployed by NRL. The 1200 m long vertical line array consisted of 31 hydrophones, 21 of which were spaced 30 m apart at nominal depths of 30 - 630 m, and 10 of which were spaced 60 m apart at nominal depths of 690 - 1230 m. The four short 300 m long vertical line arrays consisted of 8 hydrophones each at nominal depths of 30 m, 90 m, 120 m, 150 m, 180 m, 210 m, 270 m and 330 m. These were approximately positioned along the NW leg of the crossed horizontal array as shown in Fig. 3-1. The fixation points of the top of the 5 vertical arrays were at ranges of 67 m, 92 m, 116 m, 148 m and 231 m from the apex of the MIT/WHOI crossed array. Six hydrophones of the vertical line array and five hydrophones on the short arrays had severe 60 Hz contamination and were thus not used in our analysis. Using a high-frequency pinger, the hydrophone positions were recorded for only 16 channels on the long vertical line array, and I interpolated for the locations of the missing hydrophones from the shape of the array. Only the locations of the fixation points were recorded for the short vertical line arrays, and therefore I had to once again interpolate for the positions of the missing hydrophones. As shown in the following sections, I carried out an empirical analysis to estimate the sensor positions on the shorter arrays. My methodology is based on the ideas suggested by Polcari [43].

Sensor position predictions for the long vertical line array

I model the cable statics problem using a very simple approach, parameterized such that the analysis can be easily extended to similar cables. I assume the sensors to be

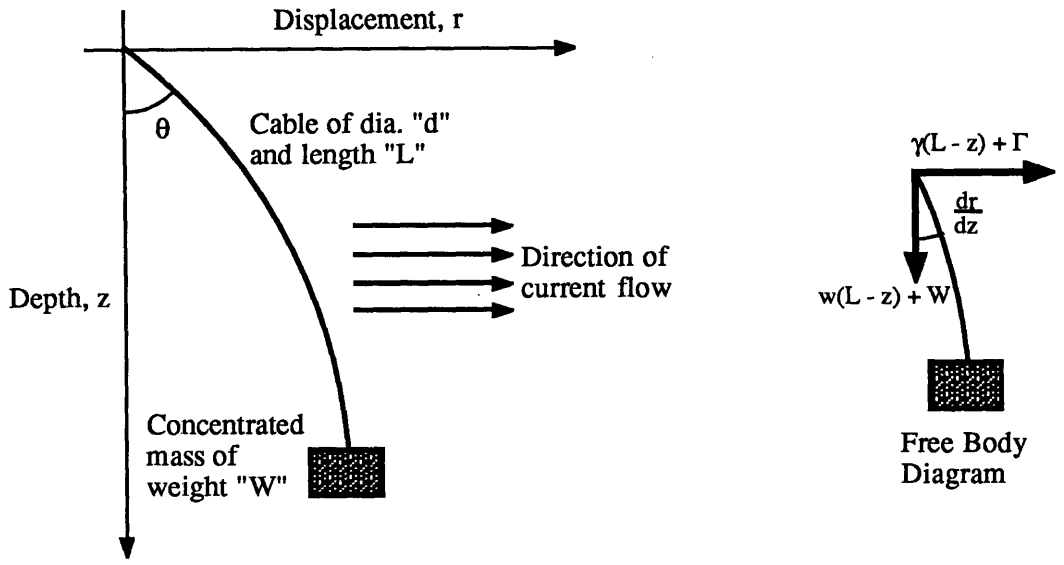

Figure 3-3: Cable displacement under a uniform current.

suspended from a uniform cable of length L, diameter d, and weight per unit length w, with one end fixed to the ice and a concentrated mass of weight W hanging at the other end as shown in Fig. 3-3. The current U is assumed to be uniform and constant in depth. Note that in the Arctic ice environment we have the additional complexity associated with the drift of the ice floe. In my model, I assume that the velocity U is the resultant of the current velocity and the drift velocity of the ice floe.

The uniform flow U produces a horizontal drag force per unit length γ on the cable and a drag force Γ on the mass hanging at the end of it. The drag force γ on the cable is given by $\gamma = \rho C_d A U^2/2$, where ρ is the density of water, A is the frontal area ($A = d \times$ unit length), and C_d is the drag coefficient which depends on the Reynolds number, $R = Ud/\nu$, where ν is the kinematic viscosity of water. The horizontal drag has two components - tangential and normal to the cable axis. The tangential component is usually much smaller than the normal component, and will thus be neglected in our analysis. This is also consistent with the small angle (or relative displacements) approximation made in this analysis.

Consider the free body diagram of a point on the cable at a vertical distance of z

from the point of suspension of the cable as shown in the right half of Fig. 3-3. The horizontal force is the sum of two components - the drag on the lower section of the cable which is approximately given $\gamma(L-z)$ and the drag Γ on the concentrated mass at the end. The vertical force is the sum of the weight of the lower portion of the cable given by $w(L-z)$ and the weight of the mass W. Note the implicit use of the small angle approximation inherent in this analysis, where I have used the vertical coordinate (z) instead of the coordinate (s) along the axis of the deflected cable.

The slope of the cable at any point z may then be expressed as

$$\tan\theta = \frac{dr}{dz} = \frac{\Gamma + (L-z)\gamma}{W + (L-z)w} \quad . \tag{3.1}$$

Eqn. (3.1) can be written as

$$\frac{dr}{dz} = a\left[1 + \frac{b}{c-z}\right] \quad , \tag{3.2}$$

where

$$a = \frac{\gamma}{w}\,, \qquad b = \frac{\Gamma}{\gamma} - \frac{W}{w}\,, \qquad c = \frac{W}{w} + L \ . \tag{3.3}$$

Integrating both sides of eqn. (3.2), and using the condition $r = 0$ at $z = 0$ yields the solution -

$$r = a\left[z - b\ln\left(1 - \frac{z}{c}\right)\right] \ . \tag{3.4}$$

This equation, which defines the shape of the cable under a uniform flow, describes the relationship between the depth z and displacement r. However, we are not done yet. We know the positions of the sensors along the length of the cable, and therefore we need to find the relationship between the depth z and the distance s along the axis of the displaced cable too.

We begin by noting that $ds^2 = dz^2 + dr^2$, or since dr/dz is assumed to be small, I can use the approximation

$$ds \;=\; dz\sqrt{1 + \left(\frac{dr}{dz}\right)^2} \;\approx\; \left[1 + \frac{1}{2}\left(\frac{dr}{dz}\right)^2\right] dz \ . \tag{3.5}$$

Substituting eqn. (3.4) in eqn. (3.5), integrating both sides, and using the condition $s = 0$ at $z = 0$, we obtain the result

$$s = z\left(1 + \frac{a^2}{2}\right) - a^2 b \ln\left(1 - \frac{z}{c}\right) + \frac{a^2 b^2}{2}\left(\frac{1}{c - z} - \frac{1}{c}\right) \cdot \tag{3.6}$$

Thus eqns. (3.4) and (3.6) then relate s, z and r for any point on the cable. As mentioned earlier, positions of only 16 sensors on the long vertical array were recorded using a high-frequency pinger. The depths and horizontal displacements of these receivers along the $SW - NE$ axis are then used in a *least-squares-minimization* scheme to estimate the parameters a, b and c which best fit the data. My results yield

$$\begin{aligned} a &= \frac{\gamma}{w} &&= 0.85 \ , \\ b &= \frac{\Gamma}{d} - \frac{W}{w} &&= -1322.4 \ , \\ c &= \frac{W}{w} + L &&= 2553.1 \ \cdot \end{aligned} \tag{3.7}$$

Using these estimates in eqn. (3.4), I can draw the deflected shape of the long vertical line array in a plane parallel to $SW - NE$ axis as shown by the dark line in the lower part of Fig. 3-4. It is evident from my results that the simplified analysis I have carried out is adequate at modeling the real data. Regarding the unknown sensor locations, the only information that I have is the distance along the displaced cable. Thus I can read off their r and z coordinates from the best fit line in the lower part of Fig. 3-4. The known and interpolated sensor positions are also shown in the same figure by "*" and "o" respectively.

The cable also has an out-of-plane displacement component or an offset, as shown in the upper part of Fig. 3-4. A possible explanation is the non-uniformity of the current flow in depth, contrary to the assumptions made in our analysis. However, I was able to account for this displacement as well, by fitting a 5^{th} order polynomial through the known data points. Then, with an estimate of r for the unknown receiver positions from the lower part of Fig. 3-4, I can then also estimate their out-of-plane displacements as shown in the upper part of the same figure. Thus, we now have complete information on the sensor positions of the long vertical line array, and my

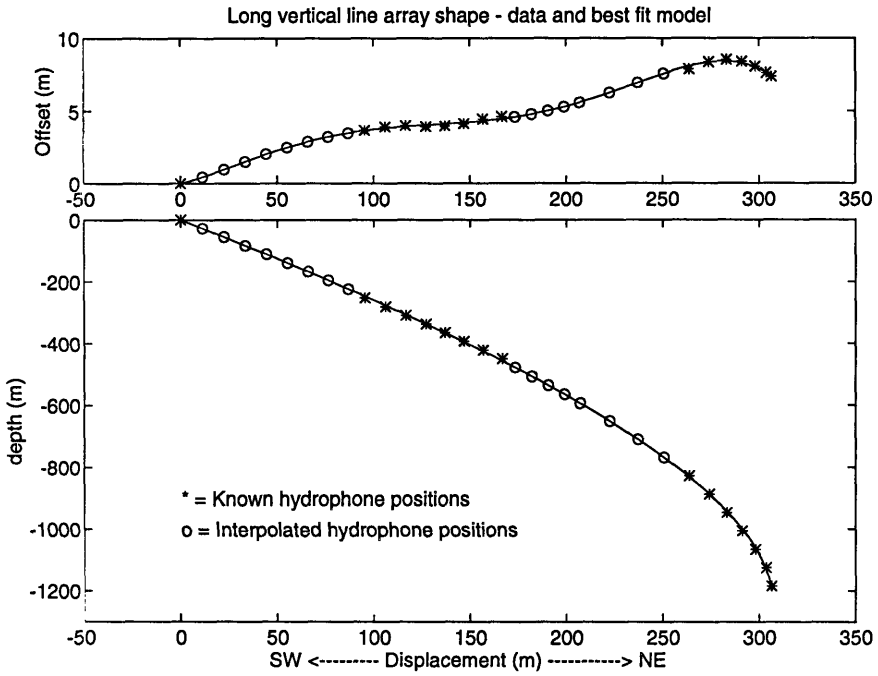

Figure 3-4: Long vertical line array displaced shape - data and best fit model with positive horizontal axis pointing along the $North - East$ direction. The array tilt is due to ocean current and drift of the ice floe.

results are summarized in Table C.2 in Appendix C.

Sensor position predictions for the short vertical line arrays

My analysis in the previous section has the significant advantage of being amenable to make predictions regarding the deflected shapes of similar cables. I have parameterized the deflected shape in terms of three quantities which were also estimated for the long vertical array. Note that the non-dimensionalization of the problem eliminated the need to know the specifics of the cable or the mass suspended from it. This is very advantageous as I will now demonstrate how I can use the analysis and results of the previous section to estimate the deflected shape of the shorter arrays.

No information was available from NRL regarding the cables or the weights suspended from them for either the long or short vertical arrays [44]. Thus, my analysis of cable statics so far is not directly useful for making any estimations on the shorter arrays. However, the information which is available to us is that the shorter arrays

were cables of length 330 m. I shall make the following assumptions for the shorter cables to estimate their sensor positions.

- The parameter a estimated above for the long cable is the same for the shorter cable. Since the shorter cable will have a smaller diameter, it will also have a smaller weight per unit length as it varies as the square of the diameter. The drag force per unit length will also be reduced since it is directly proportional to the diameter. However, the drag force also depends on the drag coefficient which in turn depends in a complicated way on the Reynolds number which is a function of the cable diameter. Therefore, this assumption is not unreasonable.

- The second parameter b is also assumed to remain unchanged for the shorter cable. For the shorter cable, the mass attached at its end must also be smaller, and therefore, also the drag force on the mass. Reasoning as above, I can conclude that this parameter also remains unchanged.

- The parameter c which depends on the length of the cable, however, does change. From my analysis I had $c = \frac{W}{w} + L$, where $L = 1230\ m$ for the long cable. From my earlier estimate of c, and using the new length $L' = 330\ m$, my estimate of c' for the shorter cable becomes 1653.1.

Using the approximations listed above, I can estimate the deflected shape of the shorter arrays as shown in Fig. 3-5. Then with a knowledge of the distances of the sensors from the point of suspension, I can estimate the sensor positions for the shorter arrays. The estimated hydrophone positions are shown by the symbol "o" in Fig. 3-5. Note the different scale of this figure compared with that of the longer array. Regarding the out-of-plane or cross displacements, having no other information, it is not unreasonable to assume that the drift current on the shorter arrays is the same as that of the longer array since they are suspended in the same water column. Therefore, I assume that the shorter arrays have the same angle of offset as the longer array. I estimated this angle from the upper figure in Fig. 3-4, and used this in predicting the offsets for the shorter arrays. Moreover, I also assume that all the shorter arrays have

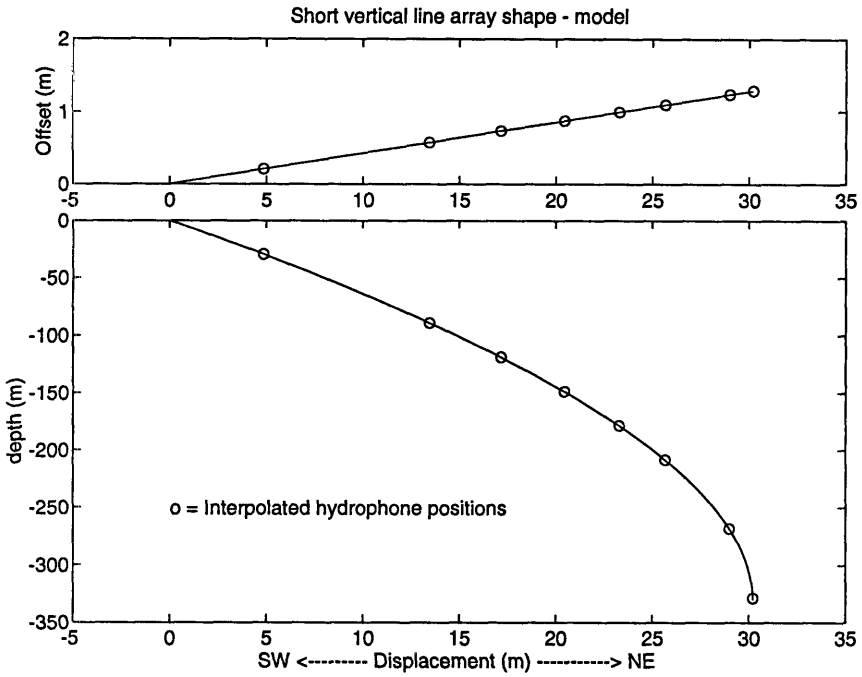

Figure 3-5: Short vertical line array displaced shape - best fit model with positive horizontal axis pointing along the *North – East* direction. The array tilt is due to ocean current and drift of the ice floe.

identical displaced shapes as computed above. However, from practical considerations, we know that this will not necessarily be the case, but this is the best I can do given the limitations of the available information. My results for the sensor positions of the four shorter arrays are listed in Table C.3 in Appendix C.

3.4 Sound Velocity Profile

The sound velocity profile was measured up to a depth of 500 m. In my analysis, I shall use a bilinear approximation of the measured profile as shown in Fig. 3-6. The gradients of the upper and lower profiles are estimated to be $g_0 = 0.0905\ s^{-1}$ and $g_1 = 0.013\ s^{-1}$ with the sound velocities at the top of the profile and at the transition depths being $c_0 = 1437.0\ ms^{-1}$ and $c_1 = 1458.5\ ms^{-1}$ respectively. The transition between the two profiles occurs at a depth of 239 m. In other words, if I let $c(z)$ be

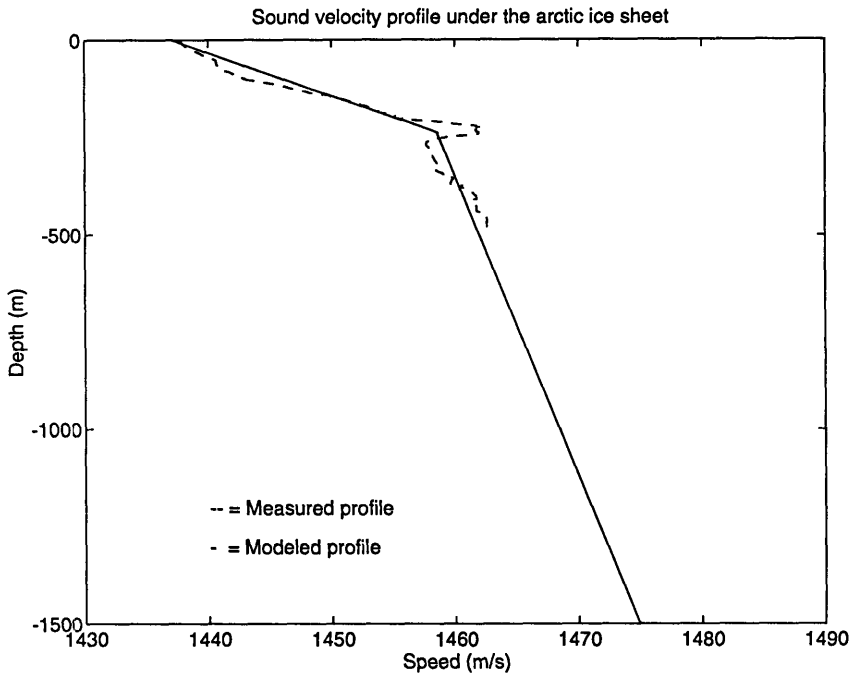

Figure 3-6: Measured and bilinear approximation of the Sound Velocity Profile.

the sound velocity at any depth z, then I can write

$$c(z) = \begin{cases} c_0 + g_0 z & \text{for } 0.0 < z < 239.0m \\ c_1 + g_1(z - 239.0) & \text{for } z > 239.0m \end{cases}$$

Additionally, it may be noted that the value 0.013 s^{-1} for the gradient of the lower profile is not very different from $0.016ms^{-1}$, the typical value for deep oceans. However, as my subsequent analysis of short range reverberation primarily involves the upper part of the SVP, I shall use the gradient estimated from the measured profile rather than the value for the deep oceans.

In all my subsequent analysis, I computed ray angles, time delays and path lengths along ray trajectories using a ray tracing algorithm. The methodology behind this algorithm is as follows. To compute these quantities I discretized the spatial domain of interest into a discrete set of points. To compute these ray quantities with respect to the source, I launched a series of rays covering the whole angular spectrum, and then tabulated the arrival times, source and receiver angles, and path lengths. I interpolated for these quantities at points of interest using cubic splines. I benchmarked

my ray tracing algorithm to verify if it gave the right answers by comparing these with those obtained by using an isovelocity SVP. Other than due to refraction, these numbers from my ray tracing algorithm agreed reasonably well with those obtained from straight line paths. I carried out a similar analysis for estimation of these parameters for rays launching off from the ice sheet. The numbers obtained were close to those from a constant SVP, once again, validating my ray tracing code.

3.5 Data Conditioning

The first task at hand was to extract the segment of data of interest to us from optical disks for the horizontal arrays. The data was stored in WHOI on optical disk # M120-7321-185, side # 2. The vertical array data, with a 16-bit integer format, was acquired from NRL (courtesy Tom Hayward) on an exabyte tape. Before any data could be processed, I had to synchronize the two different data sets to the same reference time frame, i.e., I was required to estimate the shot times or the *zero* time reference for the time series. The NRL log book records show that five shots were fired at 15 minute intervals of which one turned out to be a dud. Thus, data from only four shots was available for the analysis. The shot times recorded in the log book were 13:41:55, 13:56:50, 14:11:00 (dud), 14:26:52 and 14:41:50 hours local time. To estimate the shot time in the data, I needed to know the locations where the charges were set off. As far as the source locations were concerned, the only information available was that the SUS charges were dropped into Wiebe's biology hydrohole (see Fig. 3-1). However, the precise location of this spot was not available, and therefore, I was also faced with the task of estimating the source positions from the raw time series.

3.6 Raw Experimental Data

Fig. 3-7 shows the raw time series for Shot # 1 for the 25 channels of the horizontal array, sampled at 1 kHz. The channels numbers on the plot are in no particular

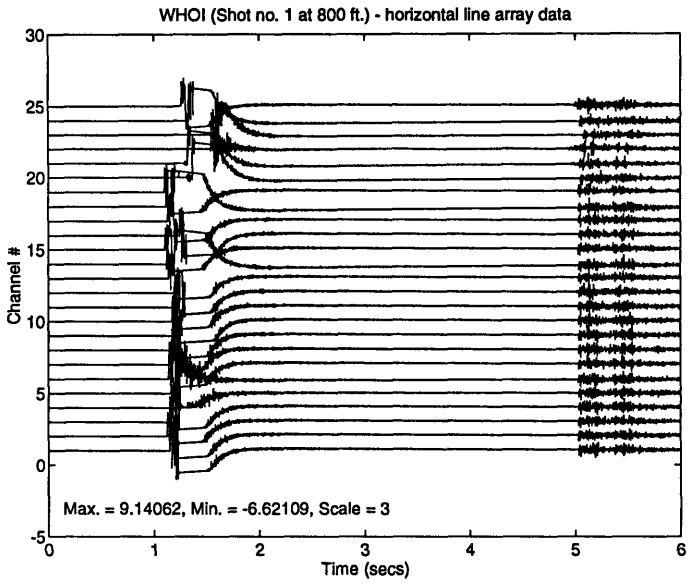

Figure 3-7: Horizontal line array raw data for Shot # 1. Observe the direct bottom returns that arrive around 5.1 *secs*, and the surface-reflected bottom returns that arrive about 0.2 *secs* later.

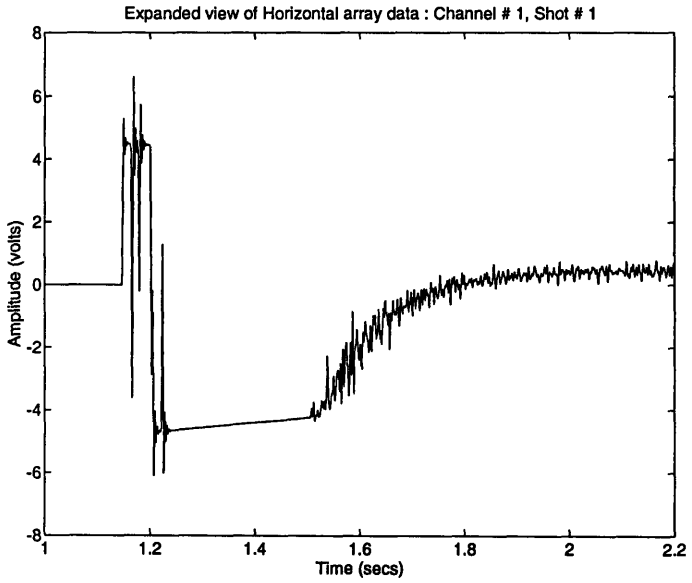

Figure 3-8: Expanded view of horizontal line array raw data for Shot # 1, Channel # 1.

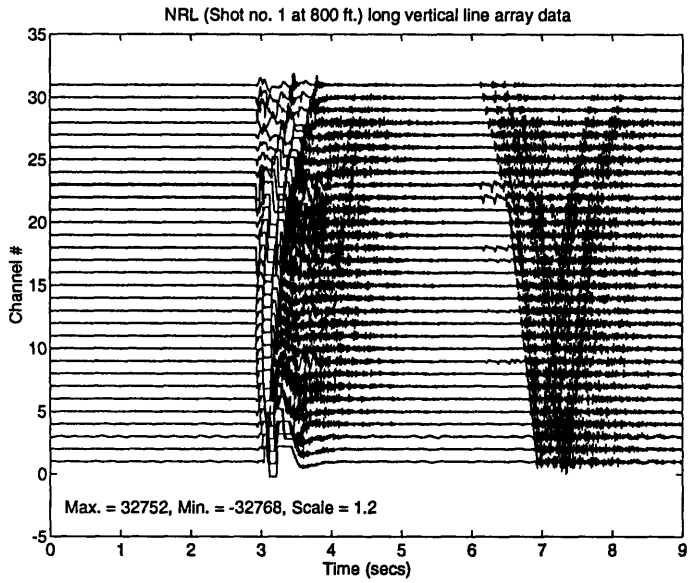

Figure 3-9: Long vertical line array raw data for Shot # 1. The direct bottom returns and the surface-reflected bottom returns are clearly distinguishable for the deeper receivers.

order. The direct shock pressure pulse is seen to arrive around 1.2 *secs* at most of the receivers. The hydrophones are observed to saturate with the arrival of the shock pressure pulse. After a characteristic system decay time, the sensors are seen to come back on line as shown in the expanded view in Fig. 3-8. Note that the data is not clipped but superposed on a system decay response. Also, the bubble pulses can be easily seen in the close-up view of the time series. The ocean bottom is roughly at a depth of 3.0 Km, and therefore, as we would expect, the first bottom arrivals come in about 4 *secs* later, at a time of about 5.1 *secs*. Also seen are the surface-reflected bottom returns that arrive about 0.2 *secs* later. The usable data for estimating short-range scattering from under the ice surface is then contained between 1.8 *secs*, i.e., after the sensors come back on line, and 5 *secs*.

On the other hand, the raw time series for the 31 long vertical and 32 short vertical line array hydrophones, sampled at 689.0625 Hz, are shown in Fig. 3-9 and Fig. 3-10 respectively. As mentioned before, these time series were recorded on a different data acquisition system by NRL. The direct arrival is seen to come in around 3.0 *secs* for the top-most receiver of the long vertical array, denoted by channel # 1. The

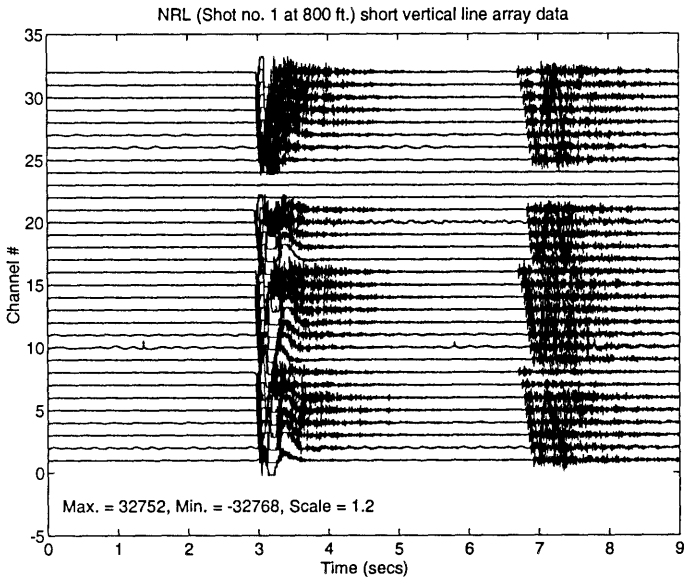

Figure 3-10: Short vertical line array raw data for Shot # 1.

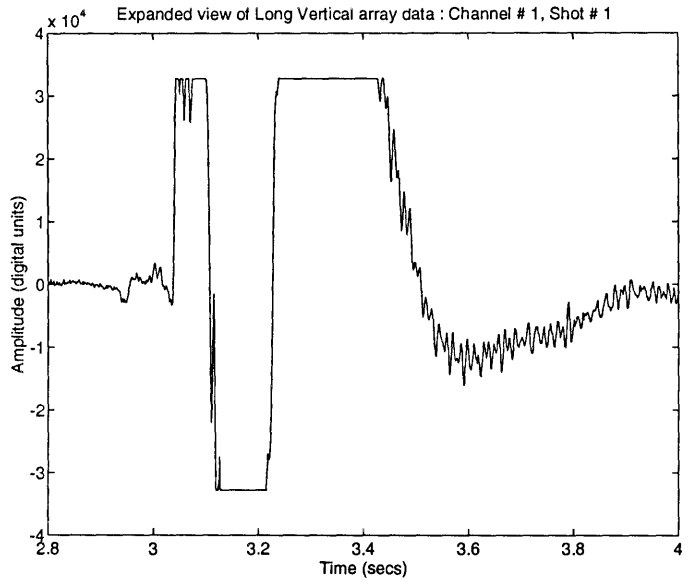

Figure 3-11: Expanded view of long vertical line array raw data for Shot # 1, Channel # 1.

receiver time series are stacked in the order of depth with the deepest hydrophone corresponding to Channel # 31. The bottom reflected arrival comes in about 4 *secs* later at a time of about 7.0 *secs* for the shallowest receiver. Note how the direct bottom returns and the surface-reflected bottom returns are clearly separated for the deeper receivers of the long vertical array. These could also be used in the future to evaluate the scattering characteristics of the ocean bottom in the Arctic Ocean. In contrast to the MIT/WHOI system, the arrival of the shock pressure pulse at the hydrophone nearest to the source, results in a simultaneous saturation of all the hydrophones as is evident from the expanded view of the time series of a typical sensor of the vertical arrays as shown in Fig. 3-11. In spite of the clipping of the time series, we can observe the faint outline of the bubble pulses here. However, I do not have enough confidence to use these in any kind of estimation scheme.

3.7 Source Localization

To estimate the source locations, I developed a source localization scheme based on a χ^2 estimation procedure. In general, I need to search a four-dimensional parameter space with the unknowns being the three source coordinates and the shot time. However, to simplify the analysis, I did this in two steps by reducing the number of unknowns to three by estimating the source detonation depths via a different analysis.

Previous results by Wakeley [45] have shown that the depth of detonation may be related to the first bubble pulse period and weight of the charge by

$$Z = (0.21)^{6/5}\, W^{2/5}\, (T_{BP_1})^{-6/5} - 10.1 \quad , \tag{3.8}$$

where Z is the depth of detonation in m, W is the weight of the charge in Kg, and T_{BP_1} is the first bubble pulse period in *secs*. The bubble pulses are clearly visible in the raw horizontal array time series (Fig. 3-8) but not in the vertical array data (Fig. 3-11) which is clipped as shown before. Therefore, I estimated the first bubble pulse period from the MIT/WHOI data by noting the difference in arrival times of

Bubble pulse periods and depths of detonation		
Shot #	$T_{BP_1}(secs)$	$Z_s(m)$
1	0.0194	246.5
2	0.0199	239.1
3	0.0189	254.4
4	0.0196	244.0

Table 3.1: Estimated first bubble pulse periods and the corresponding depths of detonation

the shock pulse and the first bubble pulse, and then averaging the result over the 25 channels. As stated before, the weight of the SUS charge used in the experiments was 1.8 *lb* or 0.82 *Kg*. My estimates of the bubble pulse periods and the corresponding depths of detonation are shown in Table 3.1.

The next step is to determine the (X, Y) coordinates of the source locations, and the time when the shot was fired. This is done by first identifying the arrival time of the direct pressure pulse, i.e., the peak of the shock pulse, at each hydrophone. As noted before, the arrival times of the direct pressure pulse on the vertical array sensors is obscured by the system-wide overload. Thus, I was unable to use the NRL data in my shot localization procedure, and my analysis was therefore confined to the horizontal array arrival times only. Using ray tracing in the bilinear sound speed profile, for each assumed position of the source (X, Y), I computed the time delays from the source location to each of the receivers. The shot time is estimated by averaging the difference between the arrival times and the computed delays over all the hydrophones as

$$\hat{t}_{shot} = \frac{1}{N} \sum_{i=1}^{N} (t_i - \tau_i) \quad , \tag{3.9}$$

where N is the number of sensors used in the analysis, t_i is the arrival time at the i^{th} sensor in the raw data, and τ_i is the time delay from the assumed source position to the i^{th} sensor. The *mean-square-error*, χ^2 of our estimate for this guess is then computed as -

$$\chi^2 = \frac{1}{N} \sum_{i=1}^{N} \left[t_i - (\hat{t}_{shot} + \tau_i) \right]^2 \quad . \tag{3.10}$$

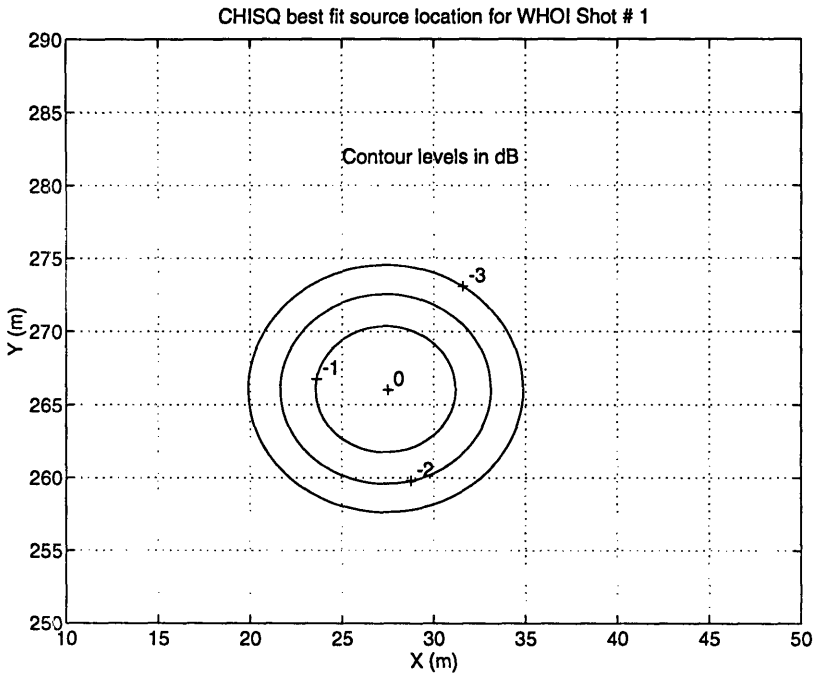

Figure 3-12: Contours of constant levels of $1/\chi^2$ for best fit source location for Shot # 1

I compute the value of χ^2 at different locations in a given region of interest and plot contours of constant values of $1/\chi^2$ as shown in Fig. 3-12, where the contours levels are plotted in a dB scale and normalized to a maximum value of 0 dB. The point where χ^2 is a minimum, or $1/\chi^2$ is a maximum, is then my best estimate of the coordinates (X_s, Y_s) of the shot location. The plot shows that I have indeed obtained this estimate with a very high resolution, the -3 dB contour being only 15 m in diameter.

I carried out this analysis for each of the four shots, and obtained similar χ^2 ambiguity contours. My results for the four different shots are summarized in Table 3.2. The results demonstrate that I was able to come up with very reliable and consistent estimates of the locations where the SUS charges went off. Moreover, these estimates are also consistent with the location of Wiebe's hydrohole (see Fig. 3-1) from where the SUS charges were reportedly dropped through a hole in the ice cover. It is also worthwhile to note that the source locations for the different shots need not be precisely the same because when the SUS charges are dropped through the hole in the ice, they will tend to drift a little, with the drift varying from shot to shot.

Estimates of source location for the 4 shots			
Shot #	$X_s(m)$	$Y_s(m)$	$Z_s(m)$
1	27.5	266.0	246.5
2	31.5	266.0	239.1
3	28.5	266.0	254.4
4	28.5	265.5	244.0

Table 3.2: Estimates of source location for the 4 different shots using a χ^2 based analysis.

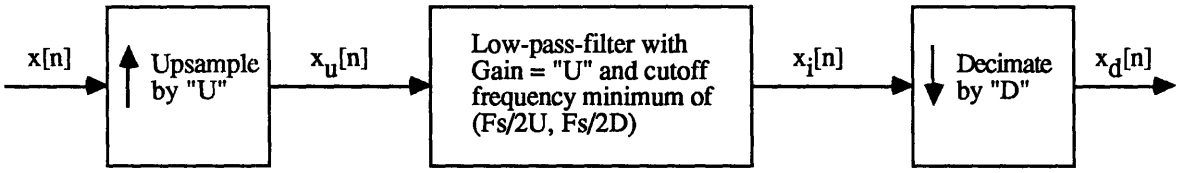

Figure 3-13: Data resampling algorithm. U is the upsampling factor and D is the decimation factor.

3.8 Data Synchronization

Before any data could be processed, the raw NRL and MIT/WHOI data had to be synchronized, i.e., filtered and resampled to the same common sampling frequency. As pointed out previously, the NRL data was sampled at the nominal rate of 690 Hz and the MIT/WHOI data was sampled at 1000 Hz. Since the maximum frequency of interest to us is 130 Hz, I decided to resample both the data sets at four times this frequency, i.e., at the common rate of 520 Hz. Fig. 3-13 shows the algorithm I used in reducing the sampling rates for the data sets by a non-integer factor. Following the approach in Ref. [46], by a combination of decimation and interpolation, it is possible to resample the data at a different rate. This is done by first identifying two integers U and D such that the ratio U/D equals the factor L by which I wish to reduce the sampling frequency. In my case, for the NRL data $U = 40$, and $D = 53$ since $L = 690/520 = 1.33$ and for the MIT/WHOI data $U = 13$, and $D = 25$ because $L = 1000/520 = 1.92$.

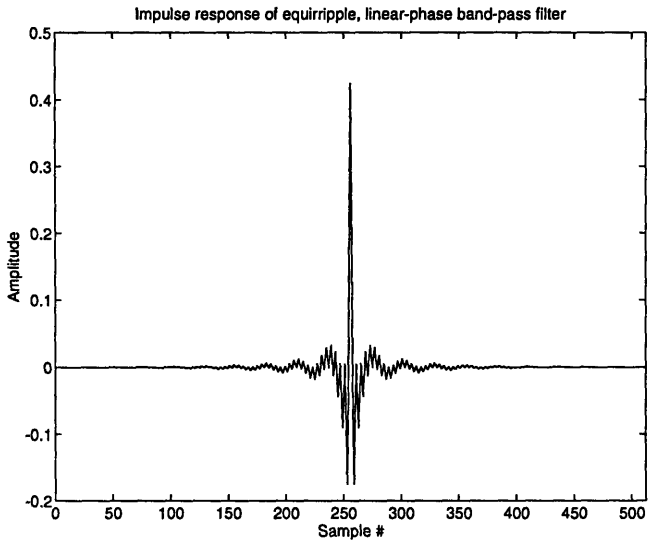

Figure 3-14: Impulse response of equiripple, linear-phase, band-pass-filter, designed using the Parks-McClellan algorithm, with a pass band of 19.5 - 130 Hz.

Having decided upon the 2 integers U and L, the raw data is first upsampled or interpolated by a factor U, low-pass filtered, and then decimated by the factor D. The low-pass filter used was a 8th order Chebyshev type I filter with cut-off frequency of 0.8 times half the sampling frequency of the data set being filtered, and a pass band ripple of 0.05 dB. The resampled data was then finally band-pass-filtered between the frequency range 19.5 Hz - 130.0 Hz using a equiripple linear-phase filter designed using the Parks - McClellan algorithm. Fig. 3-14 shows the impulse response of this FIR filter and Fig. 3-15 shows its frequency response. Note that the sidelobes are more than 85 dB down. The resampled data sets were then time-shifted to *zero* time reference to coincide with the time the SUS charges went off.

As the the two data sets were acquired on different systems, their gains and sensitivities also had to be corrected for. The MIT/WHOI horizontal array sensors had a sensitivity of -160 dB re 1 $\mu Pa/\sqrt{Hz}$, and at a 1 kHz sampling rate were low-pass filtered with a 8 pole Butterworth filter with the -3 dB point at 260 Hz. No gains were applied at pre-amplification stage [42]. On the other hand, the NRL vertical array sensors had a sensitivity of -157 dB $V/\mu Pa$, and a preamp/digitizer gain of 65536 digital units per 10 V, and variable gain settings for the four different shots

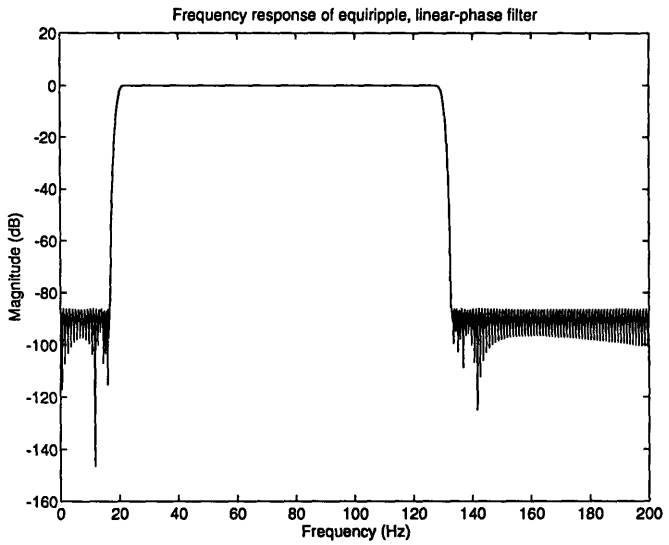

Figure 3-15: Frequency response of equiripple, linear-phase, band-pass-filter, designed using the Parks-McClellan algorithm, with a pass band of 19.5 - 130 Hz.

of 20 dB, 30 dB, 40 dB and 40 dB respectively [44]. Therefore, to obtain the data values in μPa, the MIT/WHOI values were multiplied by 10^8, and the NRL values were multiplied by the factor $(1.0/6553.6) \times 10^{157/20}$ / gain.

Fig. 3-16 shows the signal at Channel # 1 of the horizontal array after filtering, *zero* time shifting, and correcting for sensor sensitivity. From the figure, it is clear that the usable portion of the data for reverberation analysis is limited between 0.6 *secs* and the arrival time for bottom returns.

3.9 Summary

In this Chapter, I have conducted a preliminary analysis of the CEAREX field reverberation data which I will use subsequently for estimating the scattering characteristics of ice. The analysis carried out in this Chapter basically consisted of two parts -

- Array localization and source position estimation.
- Synchronization of the MIT/WHOI and NRL data sets.

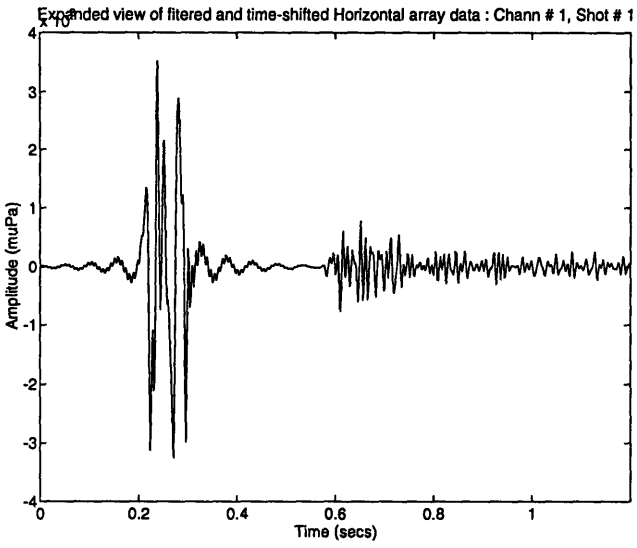

Figure 3-16: Expanded view of filtered and time-shifted horizontal line array raw data for Shot # 1, Channel # 1.

As the discussion in this Chapter illustrated, I was severely handicapped regarding the sensor positions of the vertical arrays, especially the four shorter arrays. However, aided by an empirical analysis, I was able to make some estimates of the sensor locations on the vertical arrays. I shall briefly return to these estimates in Chapter 4, where I discuss how I further improved these estimates via a different analysis.

I also obtained very reliable and consistent estimates of the positions where the SUS charges detonated. These were pre-requisite to the synchronization of the MIT/WHOI and NRL reverberation time series. The matched field analysis that shall be carried out in Chapter 4 requires these two data sets to be referenced to the same time frame. This will then allow us to simulate a volumetric array by combining the outputs from the horizontal and vertical arrays, thereby providing higher resolution in our beamformer output.

Chapter 4

Matched Field estimation of scattering from ice

4.1 Overview

As stated earlier, the main theme behind this thesis is to analyze scattering from a three-dimensional feature or protuberance under the Arctic cover. The analysis may be viewed to consist of two parts where the first deals with the development of an analytical model. This was undertaken in Chapter 2. The second part consists of an experimental evaluation of scattering using field data. Chapter 3 contained the preliminary analysis of the data from the CEAREX field experiments. The subsequent analysis will dwell upon the identification and isolation, as well as the determination of the scattering characteristics of discrete protuberances under the Arctic ice canopy. In its most general form, this is a complex multi-parameter estimation problem with the unknown quantities to be estimated being (i) the location of the protuberances, and (ii) their spatial scattering characteristics.

Among the multitude of methods available to solve this problem is the Matched Field Processor (MFP), which maximizes the correlation between data and model. In other words, the MFP compares the observed data with an assumed model defined

by a set of parameters. The search parameter set is chosen so as to encompass the true parameters which generated the data. One then searches the complex multi-dimensional parameter space for that combination set of variables which maximizes the correlation between the data and the model. The methodology of this processor will be discussed in the section that follows. Note that this is similar but distinct from the Mean Square Error (MSE) minimization method which tries to minimize the error between the data and the replica model generated from search parameters.

Within the gamut of matched field estimators are included the conventional and high-resolution processors. The conventional processor weights the dependence on the parameters uniformly, whereas the high resolution processor adaptively weights the parameters so as to maximize its performance. It is to be noted that while the performance of the conventional processor (e.g., the Bartlett processor) is relatively insensitive to mismatch in the environmental parameters that define the model, the performance of the high resolution processor rapidly degrades with increasing environmental mismatch. Ideally, one prefers to use the high resolution processor, like the Maximum Likelihood Method (MLM), since it optimizes the weights and provides estimates of the parameters with the highest resolution. However, it is severely constrained by demanding an exact knowledge of the environment that defines the replica field or model. Therefore, in a scenario where uncertainties exist in defining the environment, the Bartlett processor, in spite of its lower resolution, is to be preferred.

Coming back to my problem of locating the protuberances as well as determining their scattering characteristics, I should ideally use the MLM processor to obtain estimates of these quantities with very high confidence. However, since I am using real field data, instead of data generated in controlled surroundings, environmental uncertainties are bound to creep in. For example, I do not have the precise locations of the sensors on the vertical arrays even though my estimates for the horizontal array are reasonably good. Also, I have approximated the SVP as a bilinear profile which further introduces some errors in my estimates of arrival times and ray angles. These

uncertainties will cause a deterioration in the performance of the MLM processor which will produce erroneous results. Therefore, I will carry out my analysis with the Bartlett processor which is more forgiving.

In general, the scattered field from a large-scale feature under ice may be represented by $g(\rho, f, \mathbf{r}_p, \mathbf{r}_o)$, where ρ is the size of the feature, f is the frequency, $\mathbf{r}_p$ and $\mathbf{r}_o$ are the three-dimensional coordinates of the location of the protuberance and the receiver. Note that it is not known a priori what the functional dependence of g is on these parameters, and the position of the protuberance is not known either. This is inherently a complex problem to solve where I need to simultaneously determine the location of the feature and is scattering characteristics. Therefore, I make this insurmountable task more manageable by splitting this complicated problem into two parts. In the first step I shall isolate and identify discrete scatterers under the ice cover. My theoretical analysis in Chapter 2 allows me to assume that the three-dimensional features resemble point radiators with a quadrupolar scattering pattern. Fricke [13, 24] has demonstrated that the scattering pattern from a two-dimensional protuberance on an elastic plate, i.e., an elastic keel, resembles a deformed quadrupole. That this is also the case for the three-dimensional scattering scenario will be confirmed by my analytical realizations of scatter from an isolated protuberance under ice. This assumed scattering pattern, will then provide me with an approximate map of the under surface of the rough ice cover. As my analysis will demonstrate, I obtain satisfactory results and am able to isolate strong features or "hot spots". This will be the main focus of this Chapter.

In Chapter 5, I will continue with the next step where I will evaluate the spatial scattering characteristics of these protuberances. In general any acoustic field can be synthesized by a multi-polar expansion. Theoretically, any such expansion must include poles of all orders. However, once again, I shall make my analysis tractable by assuming that the scattered field consists of a dipole term and a quadrupole term. For the low frequency regime that is of interest to us, as previously shown by Fricke [13], this is not an unreasonable approximation as the contribution from the higher

order terms may be shown to be negligible. In fact, the estimates obtained from the data and my analytical model will reiterate the validity of my assumption.

The matched field estimation procedure that I carry out is a significant improvement over the results that have been published recently [47] using the data from the long vertical array only. The results presented here are of higher resolution as I have combined the outputs from all the arrays, simulating a volumetric array [48]. Another difference between the results of this thesis and the previously published work is that while I compute my results via matched field processing, their results were based on plane-wave beamforming.

4.2 Matched Field Array Processing

As mentioned earlier, the matched field processor correlates the field arriving at the array with model replicas of the expected field. In other words, the intent is to find which replica field best compares with the received signal. Matched field processing techniques have traditionally been used by researchers in Acoustics in the past in the context of plane-wave beamforming. The beamformer steers the array in all possible look directions and outputs the direction with which the best match was obtained between the received plane-wave and the modeled replica plane-wave. However, recent literature [49] has demonstrated the applicability of this approach in the context of localizing a distant source in range, depth and bearing. Here, I shall adapt the algorithm to nearfield beamforming or focusing.

Consider an N element array in a narrowband environment where both signal (s) and noise (n) are present. Following the approach outlined in [50], I assume the noise process to be white, and uncorrelated from sensor to sensor. Denoting the signal arriving at the array by $S(\omega, \underline{z}_n|\underline{p}_T)$, and the noise at the array by $\mathcal{N}_n(\omega)$, with variance $\mathcal{N}_0(\omega)$, I can write

$$\mathcal{N}_n(\omega) = \mathcal{N}_0(\omega)\delta_{ij} \quad ,$$

where ω is the frequency of the narrowband signal. Note that $S(\omega, \underline{z}_n|\underline{p}_T)$ contains

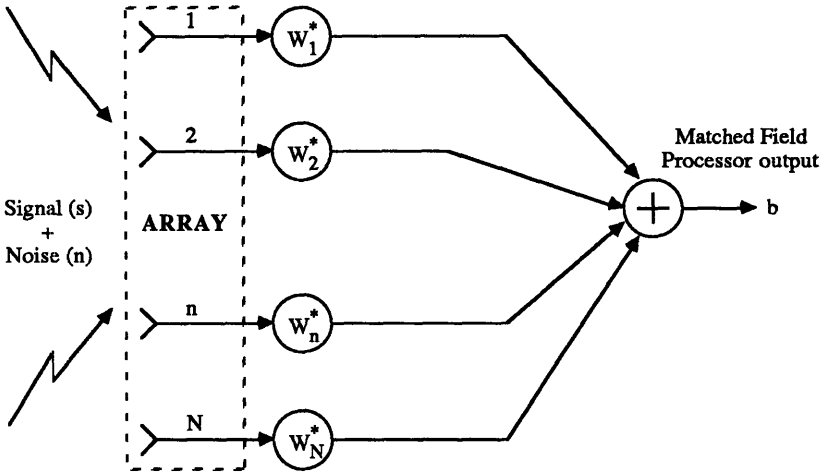

Figure 4-1: Flowchart depicting matched field array processing. s is the signal arriving at the sensors, n is the noise component, uncorrelated from sensor to sensor, and b is the matched field processor output.

both the signal and noise components, and is dependent on $\underline{p}_T$, the true parameter set describing the field. Examples of $\underline{p}_T$ include source location coordinates (x, y, z), direction of plane-wave $\underline{k}$, or sound speed of the medium $\underline{c}$. In the frequency domain, the matched field processor output, b_{signal}, is obtained by weighting the signals at the sensors by W_n^*, followed by summation over all the elements of the array as shown in Fig. 4-1. Here "*" denotes complex conjugate. In other words, the output of the processor may be written as

$$b_{signal} = \sum_{n=1}^{N} W_n^* \, S(\omega, \underline{z}_n | \underline{p}_T) = \underline{W}^+(\omega) \, \underline{S}(\omega) \ , \tag{4.1}$$

where "+" denotes complex conjugate transpose. The white noise level at the output of the processor is given by

$$\sigma_n^2 = \mathcal{N}_0(\omega) \sum_{n=1}^{N} |W_n(\omega)|^2 \ . \tag{4.2}$$

The objective of the matched field array processor is to maximize the Signal-to-Noise

Ratio (SNR) at the output of the processor, i.e.,

$$\underset{W_n(\omega)}{\text{Max}} \ \frac{|b_{signal}|^2}{\sigma_n^2} \quad ,$$

or

$$\underset{W_n(\omega)}{\text{Max}} \ \frac{|\sum_{n=1}^{N} W_n^*(\omega) S(\omega, \underline{z}_n|\underline{p}_T)|^2}{\mathcal{N}_0(\omega) \sum_{n=1}^{N} |W_n(\omega)|^2} \quad ,$$

or in vector notation,

$$\underset{\underline{W}}{\text{Max}} \ \frac{|\underline{W}^+ \underline{S}|^2}{\mathcal{N}|\underline{W}|^2} \ . \tag{4.3}$$

The solution may be obtained by setting $\nabla_{Re[\underline{W}]}$, $\nabla_{Im[\underline{W}]} = 0$, i.e., we must separately set the derivatives with respect to the real and imaginary parts equal to 0. This yields

$$2\underline{S}^+ |\underline{W}^+ \underline{S}| \, |\underline{W}^+ \underline{W}| \ - \ 2\underline{W}^+ |\underline{W}^+ \underline{S}| \, |\underline{S}^+ \underline{W}| \ = \ 0$$

or

$$W_n(\omega) = S(\omega, \underline{z}_n|\underline{p}_T) \ , \tag{4.4}$$

and the resulting SNR is given by

$$SNR = \sum_{n=1}^{N} \frac{|S(\omega, \underline{z}_n|\underline{p}_T)|^2}{\mathcal{N}_0(\omega)} \ . \tag{4.5}$$

In other words, the output of the processor is maximized when we correlate the signal received at the array with the true replica field. In general, the true parameter set $\underline{p}_T$ defining the received field at the array is not known. In such a situation, one uses the matched field array processor to estimate the parameter set $\hat{\underline{p}}_T$ defining the field. One computes the output of the matched field processor in response to different trial weight vectors associated with each trial parameter set $\underline{p}$. The parameter set for which the output of the processor is maximized, i.e., the field has been "matched", is then the best estimate of the true parameter set defining the field. The response of

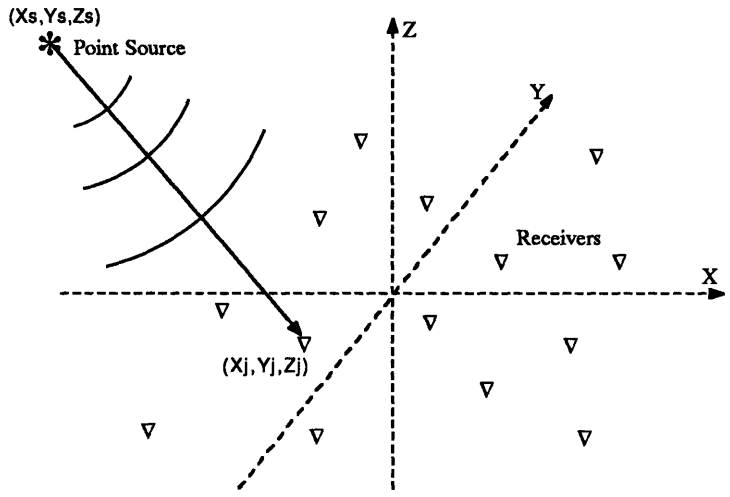

Figure 4-2: Receiver array and source geometry for nearfield beamforming or focusing

the processor to a trial parameter set $\underline{p}$, is then given by

$$\mathcal{W}(\omega, \underline{p}|\underline{p}_T) = \frac{\sum_{i=1}^{N} S(\omega, \underline{z}_n|\underline{p}) S^*(\omega, \underline{z}_n|\underline{p}_T)}{\sum_{i=1}^{N} |S(\omega, \underline{z}_n|\underline{p}_T)|^2} \quad , \tag{4.6}$$

where the output of the processor has been normalized to have unity response at the true signal parameter set. Note that in the context of plane-wave beamforming, this implies a 0 dB response at the Maximum Response Axis (MRA). Also, this processor can easily be simplified to the case of plane-wave beamforming, where the parameter set defining the field received at the array reduces to the directional wavenumber $\underline{k}$.

4.3 Nearfield Beamforming or Focusing

I will now demonstrate the application of matched field array processing to nearfield beamforming or focusing. Consider a time harmonic point radiator of strength P_0 and frequency ω located at (x_s, y_s, z_s) in the nearfield of an array of receivers of arbitrary geometry as shown in Fig. 4-2. Assuming the radiation pattern to be denoted by $B(\omega, \theta, \varphi)$, the field received by the N sensors of the array, located at (x_j, y_j, z_j), may

be expressed as

$$P_j(\omega) = P_0(\omega)B(\omega,\theta_j,\varphi_j)\frac{e^{ikR_j^T}}{R_j^T} + \mathcal{N}_j(\omega), \quad j = 1,\ldots,N \ , \tag{4.7}$$

where $P_0(\omega)$ is the source strength at 1 m, and θ_j and φ_j are the polar and azimuthal angles, respectively, subtended by the source at the j^{th} receiver. $\mathcal{N}_j(\omega)$ is the noise term uncorrelated from sensor to sensor, k is the acoustic wavenumber with $k = \omega/c$, and c is the speed of sound in the medium. The distance from the source to the j^{th} receiver is given by

$$R_j^T = \left[(x_s - x_j)^2 + (y_s - y_j)^2 + (z_s - z_j)^2\right]^{1/2} \ , \ j = 1,\ldots,N \ \cdot \tag{4.8}$$

The nearfield beamforming operation estimates the strength of the point source and its location from the received signal at the N sensors. Since my model assumes a point radiator, the signal strength may be estimated by exploiting the difference in phase of the spherical wavefront at each of the sensors. Noting the analogy with my analysis in the previous section on matched field array processing, the received signal at the array $P_j(\omega)$ corresponds to $S(\omega, \underline{z}_n|\underline{p}_T)$, while the parameter $\underline{p}_T$ corresponds to the source location coordinates (x_s, y_s, z_s). For a trial source position (x, y, z), the output of the nearfield beamformer is given by

$$\hat{P}(\omega) = \sum_{j=1}^{N} W_j \, R_j \mathcal{B}_j \, P_j(\omega) e^{-ikR_j} \quad , \tag{4.9}$$

where

$$R_j = \left[(x - x_j)^2 + (y - y_j)^2 + (z - z_j)^2\right]^{1/2} \ , \ j = 1,\ldots,N \quad , \tag{4.10}$$

and

$$\mathcal{B}_j = \frac{b_j}{\sum_{j=}^{N} b_j} \quad , \quad b_j = \frac{1}{B(\omega,\theta_j,\varphi_j)} \quad \cdot \tag{4.11}$$

Here, W_j is the weighting or array taper vector, and the radiation pattern has been normalized to obtain a 0 dB response at the MRA. The radial distance R_j appears in the numerator of eqn. (4.9) to account for the spherical spreading loss. In applications

where the change of this term from one sensor to the other is small, this term may be conveniently dropped without affecting the performance of the processor. However, if we are interested in estimating the source strength, then it is crucial that this term be retained. Also, the term $B(\omega, \theta_j, \varphi_j)$ accounts for the radiation pattern. In this case, eqn. (4.9) will yield the estimate of the source strength when the trial source position coincides with the true source coordinates.

The discussion so far has been a frequency-domain approach, where the output of the matched field processor is computed for narrowband signals. However, if we have a wideband signal, it may be advantageous to do the processing in the time domain by invoking time-frequency duality. Although, the processing becomes faster, there are some caveats to be noted here.

(i) Sampling in time

Imposing an upper limit on the error in phase, say $\pi/2$, the highest frequency for which the processing can be done in the time domain is limited by the sampling rate of the data, i.e. if we impose the requirement

$$2\pi f(\Delta t) < \frac{\pi}{2} ,$$

then

$$f_{max} < \frac{1}{4(\Delta t)} . \tag{4.12}$$

(ii) Sampling in space

The second point to bear in mind concerns the spacing between the array elements. Imposing a similar constraint on the phase error in the spatial domain requires

$$k(\Delta R) < \frac{\pi}{2} ,$$

where, k is the acoustic wavenumber, and ΔR is the difference in path lengths from the source to adjacent receivers as shown in Fig. (4-3). As can be seen from the figure, the path length differential ΔR varies from sensor to sensor in the array. Hence, it

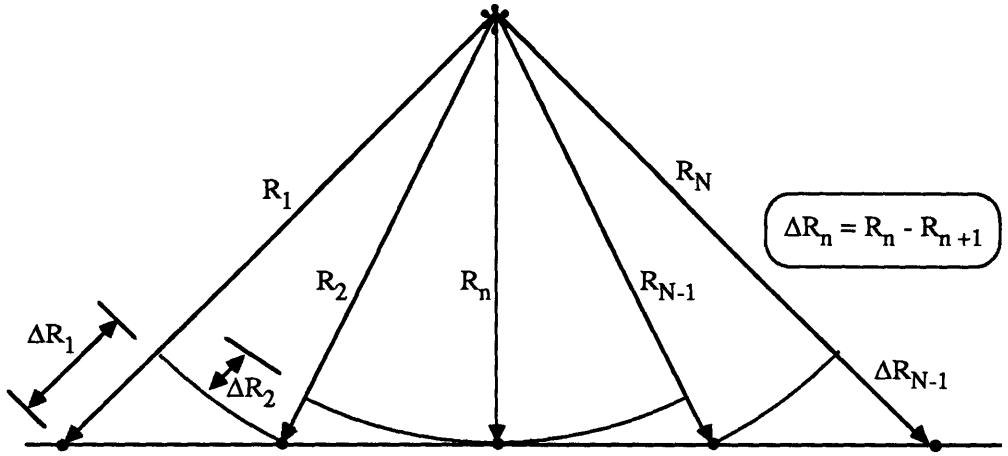

Figure 4-3: Equally spaced line array geometry for determining differential path lengths in nearfield beamforming.

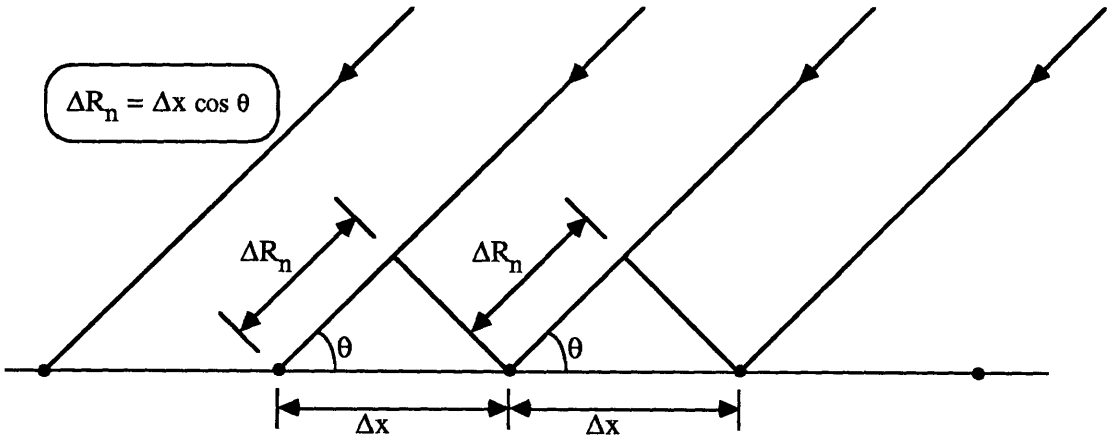

Figure 4-4: Equally spaced line array geometry for determining differential path lengths in plane wave beamforming.

is not very obvious which ΔR one should consider when developing the phase error criteria. If one is overly cautious, then the criteria must be satisfied by the minimum ΔR. In practice, this usually needs to be violated and one chooses a typical value of ΔR for the array such that

$$(\Delta R)_{min} < (\Delta R) < (\Delta R)_{max} \quad ,$$

and then one proceeds to develop a bound for the error in phase. However, if we consider plane-wave beamforming with a uniformly spaced line array, and an inter-element spacing of Δx as shown in Fig. 4-4, and relax the phase error criterion to be π instead of the more stringent $\pi/2$, we get

$$\frac{2\pi}{\lambda} \cos(\theta) (\Delta x) < \pi \quad ,$$

or

$$f_{max} < \frac{c}{2(\Delta x)\cos(\theta)} \quad , \tag{4.13}$$

where θ is the grazing angle made by the incoming plane-wave with the line array. Considering the case when the array is steered broadside, this reduces to the familiar Nyquist sampling criterion $(\Delta x) < \lambda/2$. I will refer back to eqns. (4.12) and (4.13) subsequently when I shall evaluate the performance of our arrays.

(iii) Frequency dependence of radiation pattern

In general, the radiation pattern of the source depends on both frequency (ω) and the angles subtended at the receivers (θ_j, φ_j). Therefore, unless the beampattern is frequency independent, or constant over the signal bandwidth, i.e., $B(\omega, \theta, \varphi) \equiv B(\theta, \varphi)$, it would be erroneous to to the processing in the time domain.

4.4 Adaptive Focusing for CEAREX arrays

In the analysis to be presented in this section, I shall combine the outputs from the horizontal array, the long vertical line array, and the four short vertical line arrays. I begin by simulating a broad band point monopole source, a truncated *sinc* function of bandwidth 125 Hz, duration 65 *msecs* and sampled at 1 kHz. A truncated *sinc* is convenient as it has a flat frequency spectrum and is very narrow in the time domain. I let the source be located at (900.0,900.0,3.357), i.e., at the mean depth of the ice sheet. Next, assuming spherical spreading, I propagated the field to all the receivers as shown by eqns. (4.7) and (4.8) and constructed a synthetic time series for each of the sensors. Note that since the monopolar source has a uniform radiation pattern which is independent of frequency, i.e., $B(\omega,\theta,\varphi) = 1.0$, I can take advantage of time-domain processing. Simultaneously, I also added white Gaussian noise to all the sensors with an effective SNR of 60 dB. Satisfying the criteria of eqn. (4.12) requires that the limiting frequency for which time-domain processing is acceptable is given by $f_{max} < 1/(4 \times 0.001)$ or $f < 250Hz$.

Having synthesized the time series for each of the channels, I then used nearfield beamforming or focusing to propagate the fields back to the plane coinciding with the mean ice depth. It is to be noted that back propagation is a particular case of matched field processing as in both schemes, the output is given by the product of the signal received at the array and the conjugate of the replica field. In the first stage of my analysis, I used the three array configurations separately to evaluate their individual performances. Fig. 4-5 shows the ambiguity function for the crossed horizontal array, where I have focused onto a grid of dimensions 600 m square using a step size of 10.0 m. Also, I have geometrically averaged the output of the processor over the frequency band 45 Hz - 55 Hz. It has been shown previously [49] that the sidelobe levels can be further reduced by averaging over frequencies, as the locations of the sidelobes is frequency dependent.

As discussed in an Section 3.3.1, the two legs of the crossed hydrophone array are each about 1280 m long, and therefore we get good resolution in range. However,

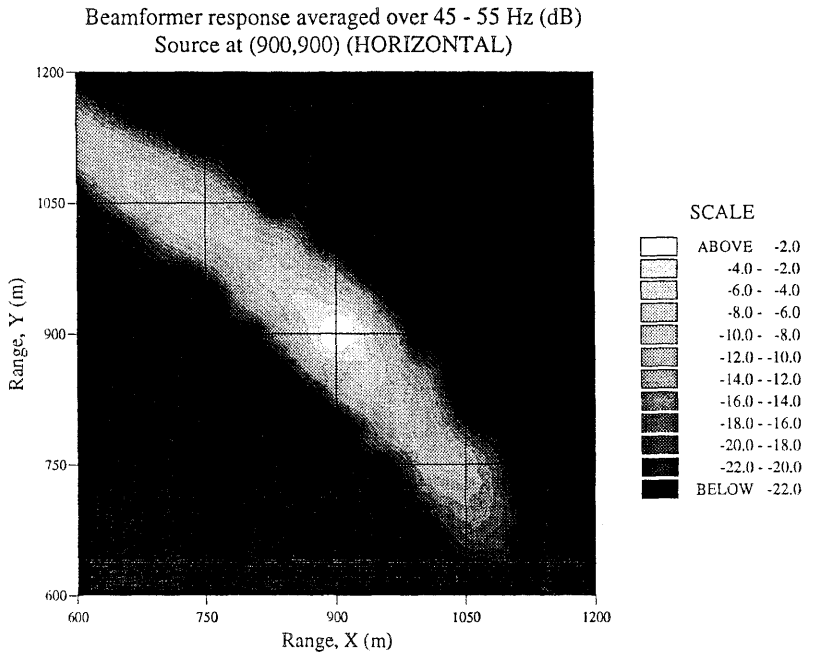

Figure 4-5: Contours of constant levels of beamformer output for the horizontal array averaged over the frequency band $45 - 55Hz$.

the array does not perform well in resolving the azimuthal ambiguity as the sensor geometry, as opposed to that of a ring array, does not sample the field fine enough in the azimuthal direction. Notice the high sidelobes, almost 6 dB down, in the azimuthal direction. From classical optics, the angular resolution of a uniform line array of length L is approximately given by $\Delta_\theta \sim \lambda/L$. Therefore, the range resolution of a uniform line array focused at a distance R_T may be approximated by $\Delta_{range} \sim (\lambda/L) \times R_T$. At a frequency of 50 Hz, the wavelength is approximately 29 m, and the distance of the source from the apex of the array is approximately 1130 m. Therefore, the resolution in range is almost $1130 \times 29/1280 \sim 25$ m. From the figure we observe the resolution in range to be about 35 m or so, not very different from the classical optics result.

Fig. 4-6 shows the ambiguity function for the long vertical line array alone, averaged over the same frequency band as before. As we would have expected, this array has good resolution in range, in the order of about 40 m or so, but poor resolution in the azimuthal direction. The response of the shorter line arrays is shown in Fig. 4-7. This array performs better than the longer vertical array in azimuth, and a little worse in

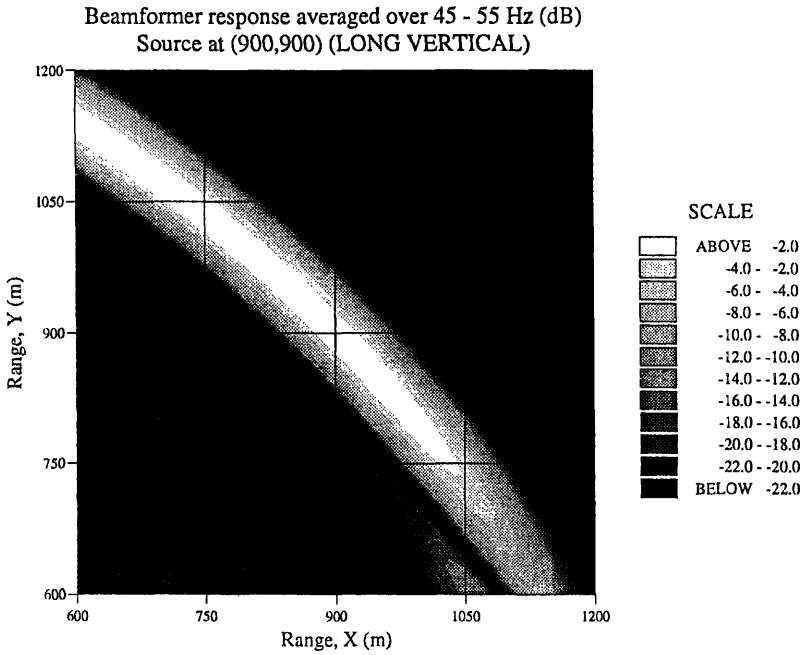

Figure 4-6: Contours of constant levels of beamformer output for the long vertical line array averaged over the frequency band $45 - 55Hz$.

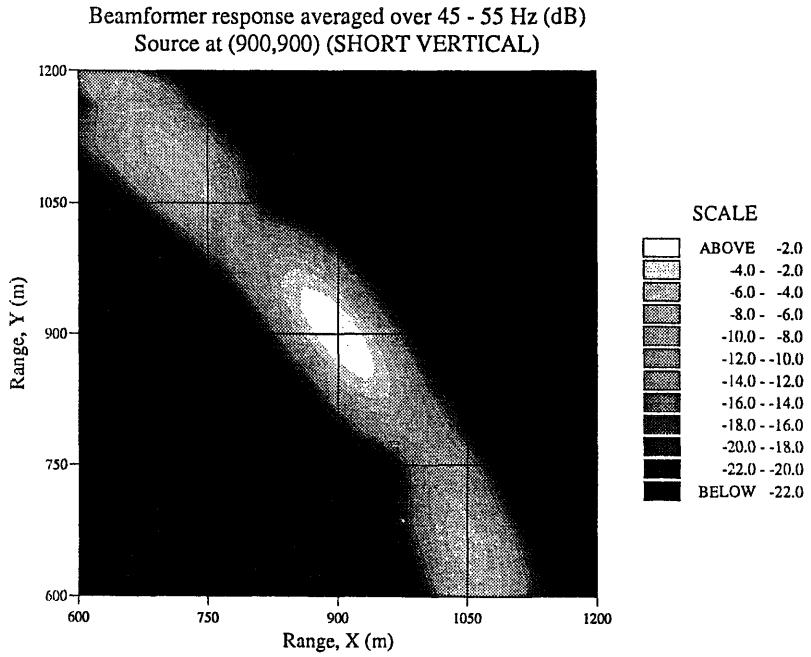

Figure 4-7: Contours of constant levels of beamformer output for the short vertical line arrays averaged over the frequency band $45 - 55Hz$.

range as the arrays are shorter in length.

My task is to combine the outputs from the three arrays in an adaptive manner so as to maximize the performance in both range and azimuth. From these results it is clear that combination of the outputs from these arrays in equal proportions will not be the most optimum response as they have different characteristics. What is required is to combine the outputs from these three arrays in a manner that optimizes the resolution in both range and azimuth. Hence, I need to introduce some kind of adaptive combination. At this stage it is worthwhile to point out that I could have chosen to use any of the high resolution beamformers like MLM or MUSIC to adaptively combine the outputs from the three arrays so as to optimize performance. However, I preferred to use the conventional Bartlett beamformer as the performance of the adaptive beamformers degrades with environmental mismatch. Note that this is unavoidable in my case, as I have limited information on the source and receiver geometry. I estimated these in the previous Chapter, but as with all estimates, these are correct within certain error bounds. This will the lead to uncertainties in arrival times, which would in turn cause the adaptive beamformers to place nulls at signal locations.

Therefore, after an extensive study of various possible combinations of the conventional beamformer outputs, I found that the best response is obtained by combining the outputs from the three arrays - horizontal, long vertical, and short vertical - in the ratio 0.6, 0.2, 0.2, respectively. Note that the sum of the three ratio factors must equal 1 if the output is not to be biased (recall the 0 dB MRA requirement). The ambiguity function for this adaptive processor is shown in Fig. 4-8, where the response has once again been averaged over the frequency band 45 Hz - 55 Hz. Note the improvement in performance in the azimuth direction while simultaneously preserving the range resolution. Also observe the significant reduction in sidelobes. I shall use this adaptive scheme in all subsequent analyses. Fig. 4-9 shows the beamformer response averaged over the frequency band 75 Hz - 85 Hz. Comparison with Fig. 4-8 reveals that, as we would expect, with increasing frequency, the width of the mainlobe is decreased

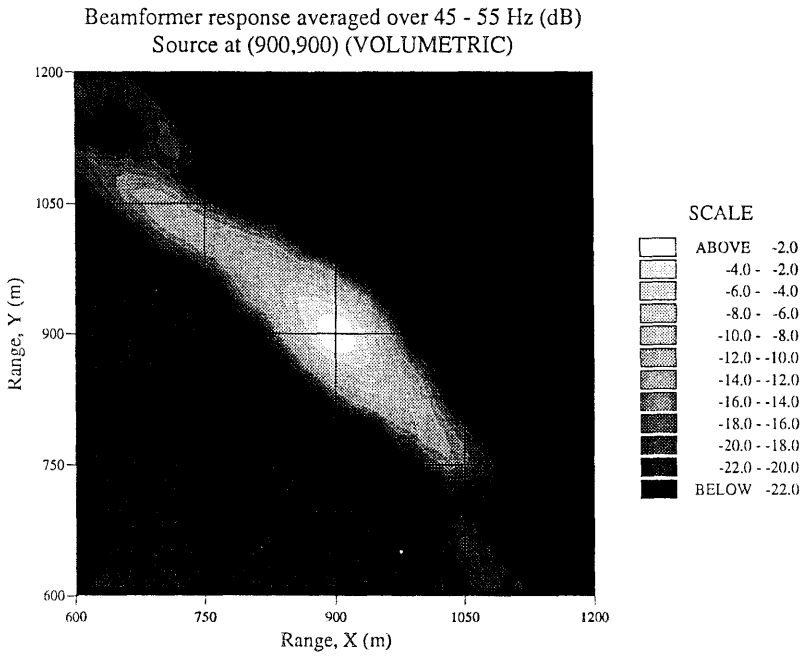

Figure 4-8: Contours of constant levels of output from the adaptive volumetric beamformer averaged over the frequency band $45 - 55Hz$.

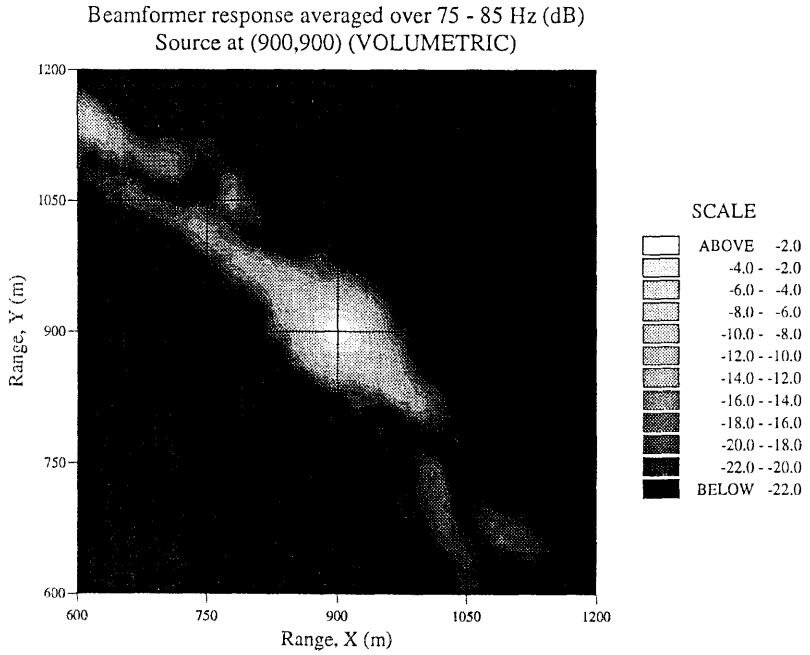

Figure 4-9: Contours of constant levels of output from the adaptive volumetric beamformer averaged over the frequency band $75 - 85Hz$.

Source Spectral Levels at 1.0 m							
f (Hz)	5.0	6.25	8.0	10.0	12.5	16.0	20.0
Level (dB)	198.79	200.30	203.03	205.86	207.59	209.61	211.65
f (Hz)	25.0	31.25	40.0	50.0	62.5	80.0	100.0
Level (dB)	213.78	215.51	217.14	218.37	217.00	212.53	211.76
f (Hz)	125.0	160.0	200.0	250.0	320.0	400.0	500.0
Level (dB)	207.09	208.31	205.35	202.28	200.80	198.83	197.27

Table 4.1: Source spectral levels at 1.0 m for 1.8 lb or 0.82 Kg SUS charges, with nominal detonation depths of 244 m.

thereby increasing resolution. Also note the significant improvement in the reduction of sidelobes levels.

4.5 Source Spectrum Estimation

Recently, Chapman [51] has presented some results from experimental data in which he estimated the spectral levels for 0.82 Kg Signal Underwater Sound (SUS) charges detonated at nominal depths of 244.0 m. The values presented by him are 1/3 octave band source levels in units of dB re 1 $erg/cm^2/Hz$ at 1 m. I corrected these to $dB\ \mu Pa$ at 1 m using the following conversion formula

$$L_s = L_s^0 + 90.0 + 10.0\log_{10}(\frac{\rho c^2}{4\pi}) - 10.0\log_{10}(BW) \quad . \tag{4.14}$$

Here L_s^0 are the levels reported by him in units of dB re 1 $erg/cm^2/Hz$ at 1 m, BW is the 1/3 octave band interval in Hz, and ρ is the density of water assumed to be 1025.0 Kg/m^3. c is the speed of sound in water assumed to have the constant value of 1460.0 ms^{-1}, and L_s is the source level in units of $dB\ \mu Pa$ at 1 m. These corrected values are shown in Table 4.1. The source levels at other frequencies of interest are easily computed by interpolation.

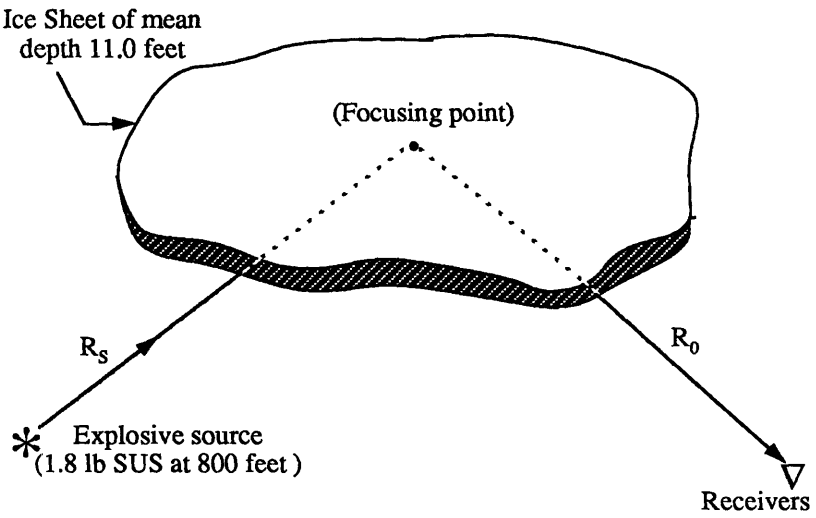

Figure 4-10: Scattering geometry showing the source, receiver and focusing point configuration. The source is 1.8 lb SUS with nominal detonation depth of 800 feet. The ice sheet is assumed to have a mean thickness of 11 feet.

4.6 Estimation of scattering strength

As mentioned earlier, the sources used in the experiments were 1.8 *lb* SUS charges, detonated at nominal depths of 800 *feet* or 244 *m*. The actual source depths were determined from the first bubble pulse periods. I shall analyze the short-range reverberation data from four different shots fired from approximately the same position. Fig. 4-10 shows the scattering geometry and the relative positions of source, receiver and ice, which is assumed to have a mean depth of 11 *feet*. The geometric paths from source to focusing points, and then on to receivers are determined using ray tracing. I shall focus onto a plane that coincides with the mean bottom level of the ice sheet.

The scattering strength calculations are based on the standard sonar equation

$$SS = L_{RL} + H_{S\to FP} + H_{FP\to R} - L_{SL} - 10\log_{10} A \quad \cdot \tag{4.15}$$

Here L_{RL} is the received pressure level at the receivers in units of dB, $H_{S\to FP}$ is the transmission loss from source to the focusing point, and $H_{FP\to R}$ is the transmission loss from the focusing point to the receiver in dB. L_{SL} is the source spectral level in

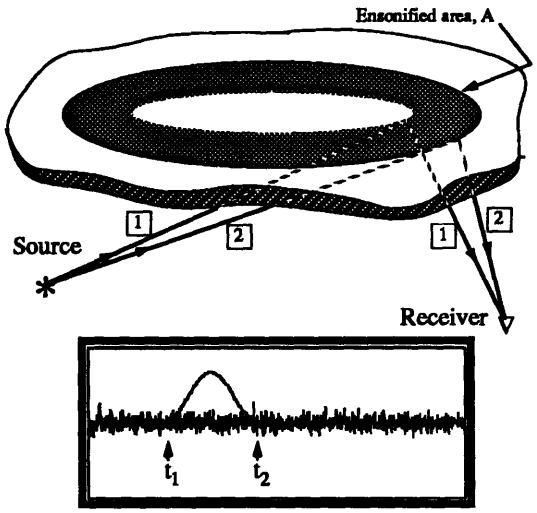

Figure 4-11: Ensonified area for the source, receiver and focusing point configuration. t_1 and t_2 are the two way travel times for paths 1 and 2

dB at a reference distance of 1 m, and A is the ensonified area. This equation yields an estimate of the scattering strength SS in units of dB/m^2.

The algorithm for computing the scattering strength of ice from the data received at all the hydrophone arrays is as follows. For each given sensor, I compute the two-way travel time from source to focusing point, and then on to the receiver using ray tracing. For a constant Sound Velocity Profile (SVP), the loci of points on the focusing plane for a fixed two-way travel time corresponds to an ellipse as shown in Fig. 4-11. This is also true for the varying SVP provided I determine the travel times from correct ray paths. I centered a small window around the two-way travel time corresponding to the focusing point of interest on each hydrophone. The area of intersection between the two ellipses, corresponding to the end points of the windowed reverberation time segment, is then the ensonified area.

Suppose the two-way travel time is t_c, and t_1 and t_2 are the end points of the window for a particular receiver as shown in the lower part of Fig. 4-11. In all my analysis, I used a Hamming window 101 samples long or 0.194 *secs* in length. The length of the window was decided upon by considering the two conflicting criteria - longer the window, higher the frequency resolution, and simultaneously, larger the

ensonified area. I need to choose a length of the window which suitably optimizes both the requirements. Coherent summation across channels of the suitably normalized, windowed outputs in the time-domain for each array separately yields the beamformer output as

$$\hat{P}^i = \sum_{j=1}^{N^i} \frac{1}{\sqrt{A_j^i}} W_j^i \mathcal{B}_j^i R_{j,s}^i R_{j,r}^i P_j^i(t_{1,j} : t_{2,j}) \cdot \tag{4.16}$$

Here $\hat{P}^i$ is the coherent beamformer output for the i^{th} array, N^i is the number of receivers in the i^{th} array, and W_j^i is the Hamming window for the j^{th} sensor in the i^{th} array. Also, $R_{j,s}^i$ is the path length from source to focusing point, and $R_{j,r}^i$ is the ray path length from the focusing point to the receiver. $P_j^i(t_{1,j} : t_{2,j})$ is the segment of data 101 samples long, centered at t_c for the j^{th} sensor in the i^{th} array, and A_j^i is the ensonified area for each sensor.

The sensor outputs have also been weighted by the suitably normalized assumed radiation pattern $\mathcal{B}_j^i$. My theoretical analysis in Chapter 5 will establish that the scatter from an isolated feature under the ice is symmetric with respect to the azimuthal coordinate φ. It will also be shown that the polar radiation pattern resembles that of a deformed quadrupole over the frequency regime of interest to us (see Figs. 5-8 - 5-11). This fact has also been corroborated by Fricke [13, 24] who considered scattering from 2D elastic keels. Motivated by these analyses, I approximated the radiation pattern from these "hot spots" as

$$B(\omega, \theta, \varphi) = \cos\varphi \ \sin 2\theta \quad , \tag{4.17}$$

where φ and θ are the azimuthal and polar radiation angles. In other words, my replica field for the matched field processing scheme is that due to a quadrupolar radiator. This radiation pattern must then be normalized to obtain $0dB$ at the MRA. This is done by defining

$$b_j^i = \frac{1}{B(\omega, \theta_j^i, \varphi_j^i)} = \frac{1}{\cos\varphi_j^i \sin 2\theta_j^i} \quad , \tag{4.18}$$

and therefore

$$\mathcal{B}_j^i = \frac{b_j^i}{\sum_{j=1}^{N} b_j^i} \quad . \tag{4.19}$$

As the beampattern is assumed to be the same over the frequency regime of interest, I can therefore do the matched field processing in the time domain. Note that in the special case of a monopolar radiation pattern, as we would expect, the weighting factor $\mathcal{B}_j^i$ reduces to $1/N^i$, i.e., that due to a uniformly weighted array.

Also, observe the different way in which the sonar equation is summed across sensors in the time domain. The beamformer output of the three arrays is then combined adaptively as -

$$P = \sum_{i=1}^{3} v_i \hat{P}^i \quad , \tag{4.20}$$

where v_i is relative weighting of the outputs from the three arrays with $\sum_{i=1}^{3} v_i = 1$. Finally, the scattering strength is found by transforming the beamformer output to the frequency domain, averaging the reverberation level in dB over 10 Hz frequency bands, and subtracting the source level at 1.0 m, i.e.

$$SS(f_c) = \left[\frac{1}{f_2 - f_1} \sum_{f=f_1}^{f_2} L_{RL}(f) \right] - L_{SL}(f_c) \quad . \tag{4.21}$$

Fig. 4-12 shows the relative geometry of the source, receiver arrays and beamforming patches. The shaded rectangular patch to the $North - East$ of the apex of the array is the area where I shall focus to estimate the scattering strength. Ideally, I would prefer to look broadside to the horizontal array, i.e., look vertically up. But this was not possible due to the limitation of the data set available for analysis. As pointed out before, the arrivals from features broadside to this array come in at times close to the direct path arrivals, and hence, are clipped. This means that I was forced to look at features at least 600 m from the apex of the array.

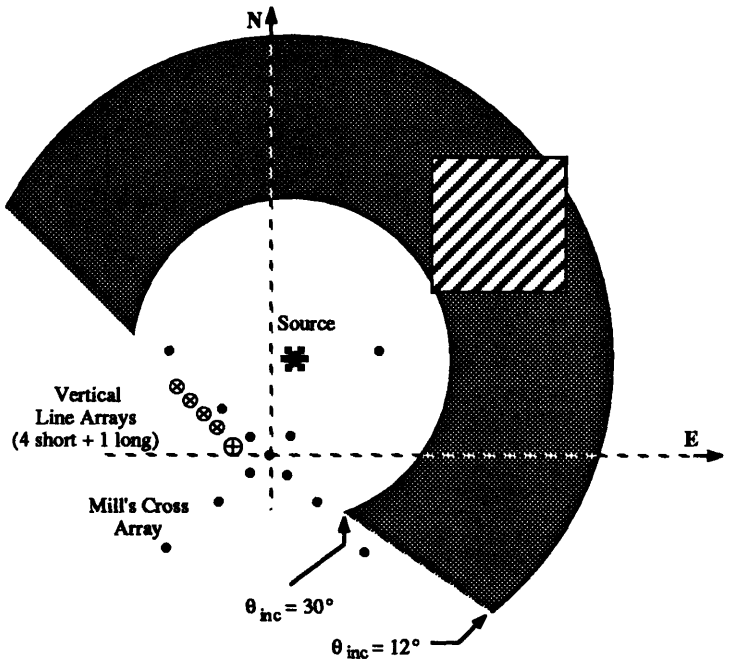

Figure 4-12: Relative geometry of source, receiver arrays and beamforming patches

4.6.1 Spatial Variation of Scattering Strength

In this section I shall use the matched field processing methodology set up in previous sections. As stated earlier, I shall assume the scatterers under the ice canopy radiate like point quadrupoles. With these assumptions, I computed the scattering strength of the rough features under the ice sheet. Recalling the phase error criterion in eqn. (4.12), we note that our time domain processing scheme is valid for frequencies $f_{max} < (1/4) \times 520$ or $f_{max} < 130Hz$ as the data is sampled at 520 Hz.

I focus on to an area that is located approximately 850 m N-E of the apex of the array as shown in Fig. 4-12. The patch of ice is 600 m square, and I have computed the scattering strength at uniform intervals of 10 m. Results for the frequency band 45 Hz - 55 Hz are shown in Fig. 4-13, where I have averaged the mean-square values of scattering strength from the four different shots. The horizontal and vertical axes correspond to range from the apex of the horizontal array. We can clearly observe the ambiguity pattern and sidelobes of our array processing scheme superposed in the plot (see Fig. 4-8). One has to view this figure bearing the response of the simulated

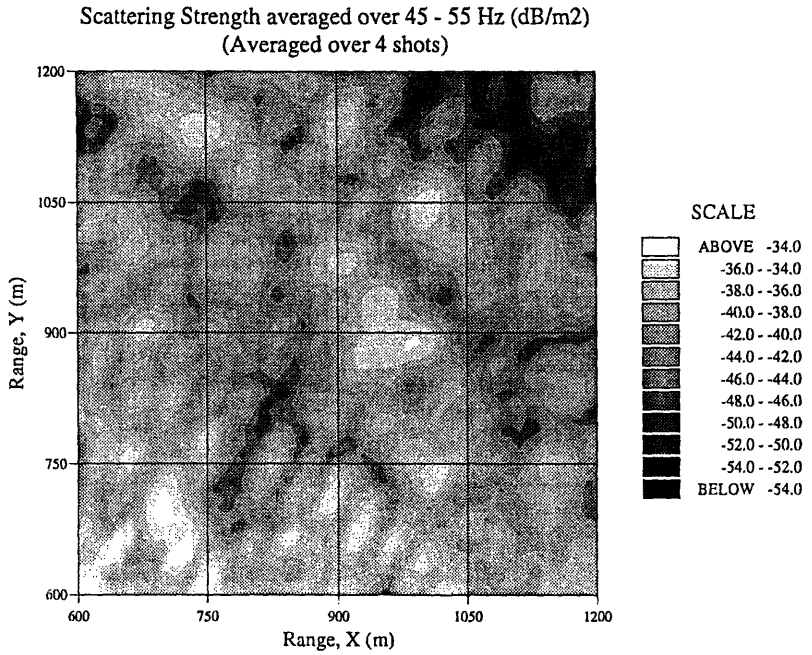

Figure 4-13: Contours of constant levels of mean scattering strength for the scattering patch located N-E of the apex of the horizontal array, and averaged over the frequency band 45 - 55 Hz.

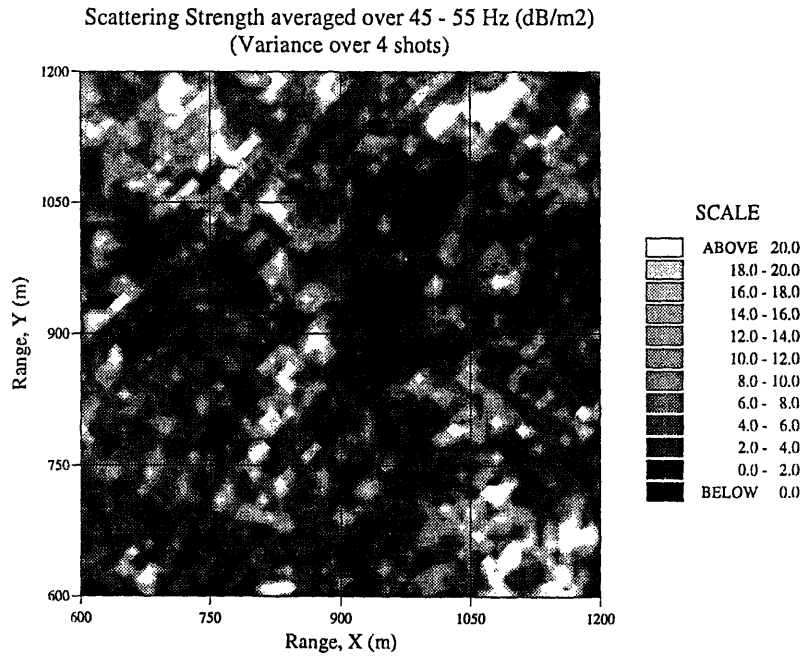

Figure 4-14: Contours of constant levels of variance of scattering strength for the scattering patch located N-E of the apex of the horizontal array, and averaged over the frequency band 45 - 55 Hz.

volumetric array in mind. We observe strong scatterers at approximate grid points of (980,890), (1000,1040), (750,1130), and (720,680). Our resolution of these features is limited by the performance of the simulated volumetric array. Therefore, it is not possible to deduce the length scales of the scatterers from this plot because of the wide beamwidth of the mainlobe. However, strong scatter in this frequency range would suggest length scales of L $\sim \lambda$, or L $\sim$ 30 m. Moreover, there could possibly be many small features within the mainlobe of this ambiguity pattern, and the ones whose sizes match the wavelengths of the acoustic field will be the ones that scatter with the highest magnitude. However, note the strong discrete scatterer at (980,890). I will return to this isolated scatterer later in my analysis, when I shall compute its scattering response as a function of grazing angle of scatter.

In Fig. 4-14, I have plotted the variance of my estimates resulting from averaging the results from the four different shots. This plot is consistent with Fig. 4-13 in the sense that regions of high scattering strength show lower variance. In other words, we have very high confidence in our processing scheme regarding the isolation of scatterers and estimation of their scattering strengths. The regions where we observe high variance are areas of low scattering strength, and corresponding lower SNR. Therefore, these tend to be closer to the noise floor should not be considered as reliable estimates.

It is instructive to evaluate the frequency dependence of the scattering strength as well. With this analysis, it will be possible to infer how strongly scatter depends on frequency. Fig. 4-15 shows the scattering strength for the same ice patch averaged over the four shots for a lower frequency band 25 - 35 Hz. Note that this plot is qualitatively similar to Fig. 4-13. Once again we observe the characteristic ambiguity pattern of the volumetric array. However, at this frequency, the resolution in range is approximately 50 m. Therefore, there is increased uncertainty regarding the size of the scatterers. Note that the scattering strength levels observed here are about 4 - 6 dB lower than those in the 45 - 55 Hz band. This is to be expected as we would, in general, predict scattering strength to increase with frequency.

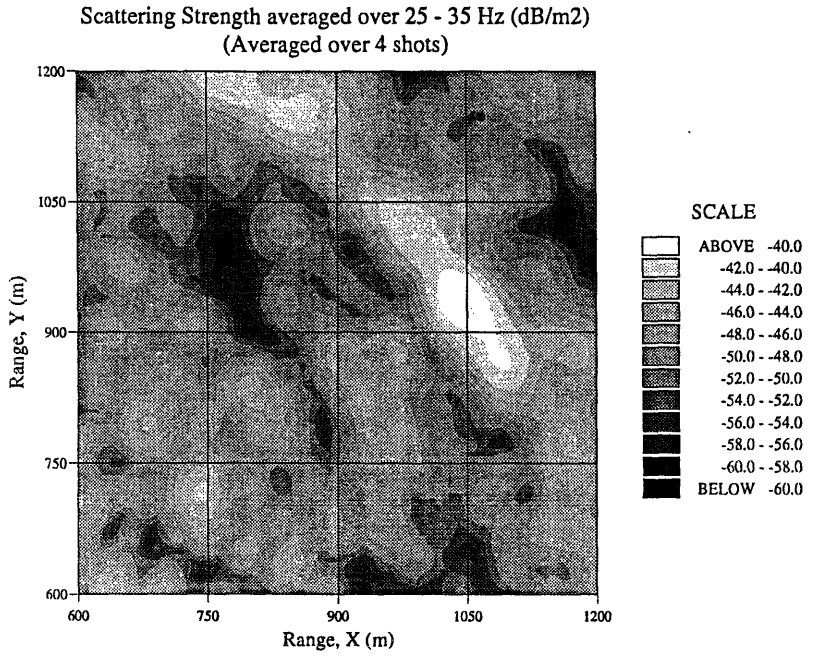

Figure 4-15: Contours of constant levels of mean scattering strength for the scattering patch located N-E of the apex of the horizontal array, and averaged over the frequency band 25 - 35 Hz.

However, the striking difference between the 30 Hz and 50 Hz results is that features at a given location do not scatter as strongly in different frequency bands. What this means is that the bright spots do not show up at exactly the same place in different frequency bands. Features that scatter strongly in the 50 Hz band do not scatter as strongly in the 30 Hz frequency band. This can also be explained by recalling that within the main lobe of the ambiguity function lie many features of varying sizes and orientation. At a given frequency of incidence of the acoustic wave, the features whose scattering characteristics match that of the incident acoustic field radiate most strongly. The important conclusion that we can draw from this result is that scattering from the under surface of the ice sheet is a frequency selective process.

Fig. 4-16 and Fig. 4-17 show the scattering strength for the same ice patch averaged over four shots for higher frequency bands 75 - 85 Hz and 95 - 105 Hz respectively. Once again we observe qualitative similarities with those presented for the lower frequency bands. Our previous deduction about frequency selectivity is reiterated by these results. In the 80 Hz results, we observe a strong scatterer at (880,740).

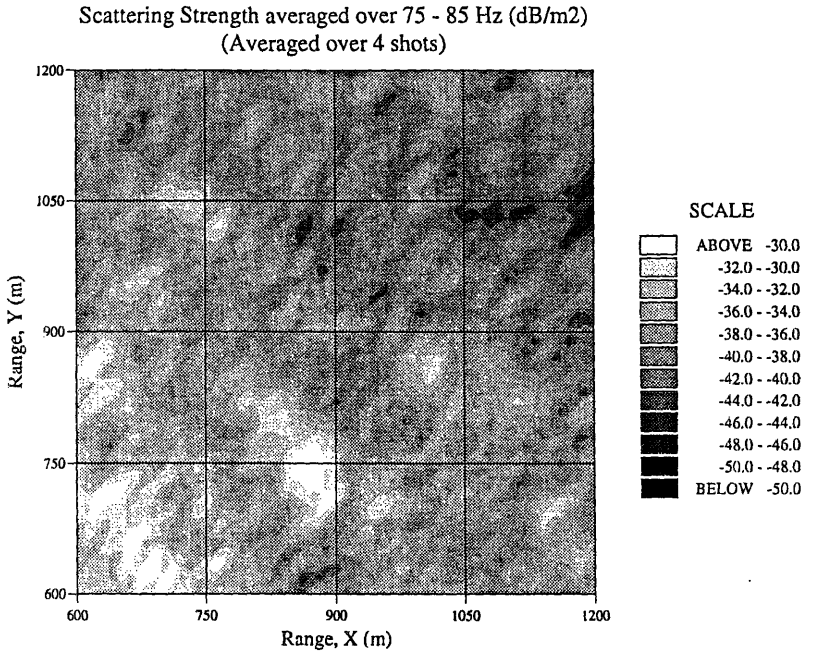

Figure 4-16: Contours of constant levels of mean scattering strength for the scattering patch located N-E of the apex of the horizontal array, and averaged over the frequency band 75 - 85 Hz.

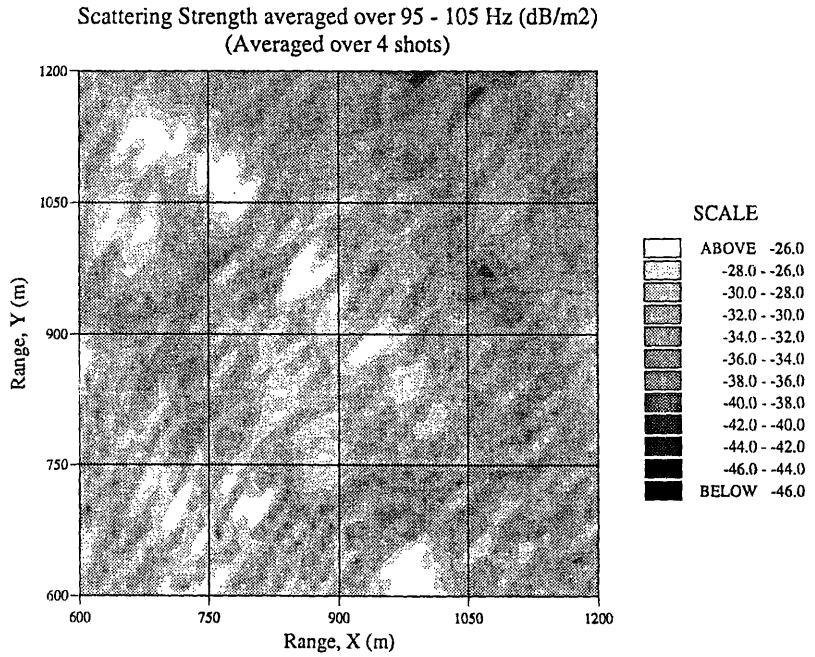

Figure 4-17: Contours of constant levels of mean scattering strength for the scattering patch located N-E of the apex of the horizontal array, and averaged over the frequency band 95 - 105 Hz.

This feature was not as striking in the 30 Hz and 50 Hz results, and shows up with a weaker magnitude in the 100 Hz band results. However, we continue to observe increasing levels of scatter with increasing frequency. Therefore, as postulated before, the results from these four frequency bands suggest a strong frequency dependence.

It is also informative to look at the scattering patterns from other patches under the ice canopy. This is essential to demonstrate that the conclusions we have arrived at for the patch N-E of the apex of the horizontal array, are also valid for other areas under the ice cover. Therefore, I decided to look at a patch of ice 850 m S-W of the apex of the array. This patch is diagonally opposite to N-E patch considered previously. The scattering patterns for two frequency bands centered at 30 Hz and 50 Hz are presented in Fig. 4-18 and Fig. 4-19 respectively. Once again we observe the circular ambiguity pattern of the volumetric array. Also, the qualitative differences about strong features that we mentioned for the N-E patch are seen here too. These results are a little deceptive in the sense that they show that features show up in the same place in both frequency bands. For example consider the bright feature in 50 Hz band at (-650,-850). It seems that it shows up at the same location in the 30 Hz results. However, in the 30 Hz frequency band we observe two peaks surrounding this location. Neither of these necessarily correspond to the feature observed in Fig. 4-19.

As another example, consider the feature at (-825,-900) in the 30 Hz band. There is no corresponding bright spot in the 50 Hz results. One can easily pick out other differences in the locations of these "hot spots" in the two plots. Therefore, we can decisively state that scatter is indeed a frequency selective process. Also, as was observed for the N-E patch, the scattering levels also increase with frequency.

4.6.2 Array localization - revisited

Before I conclude my analysis of the spatial variation of scattering strength, I need to point out some issues related to the sensor positions on the short vertical line arrays. The initial sensor positions for the short array I started out with, did not give me results that conformed to those obtained by using the horizontal array only. This

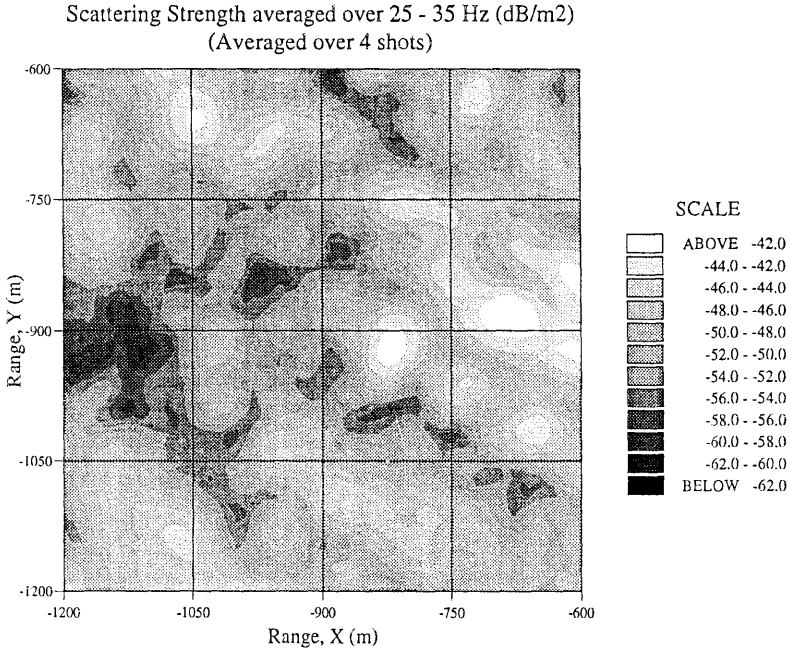

Figure 4-18: Contours of constant levels of mean scattering strength for the scattering patch located S-W of the apex of the horizontal array, and averaged over the frequency band 25 - 35 Hz.

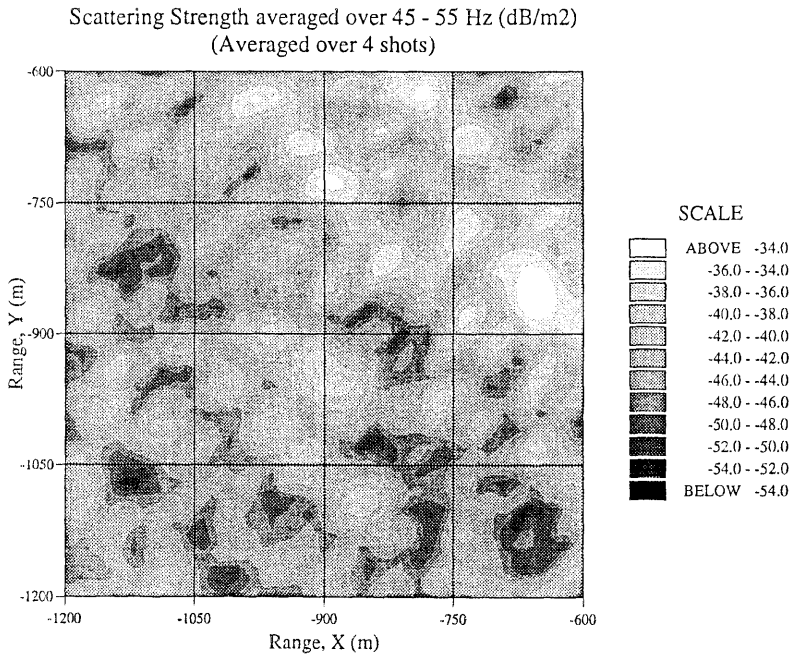

Figure 4-19: Contours of constant levels of mean scattering strength for the scattering patch located S-W of the apex of the horizontal array, and averaged over the frequency band 45 - 55 Hz.

implied that the sensor positions that I was using were not exactly correct. Therefore, I was faced with the formidable task of perturbing the geometry of the shorter vertical arrays until a good match was obtained with the focusing results from the horizontal array only.

My methodology of approaching this problem was as follows. I let the fixation points of the shorter arrays be variable within certain bounding values. Moreover, I also allowed the azimuthal orientation of the tilt of the arrays to be variable. Then, I used a simulated annealing algorithm to find these parameters for which a good match was obtained between the focusing results of the horizontal array and the shorter arrays, in particular with respect to the location of features in the same frequency bands. The shorter array geometry was allowed to vary with the constraint that the error between the source location obtained from the new sensor positions, and that from my analysis in Section 3.7 be minimized. By recursively using this algorithm, I found the parameters for which the best match was obtained. These were, then, the sensor positions for the shorter arrays that I used in all my analysis, and are listed in Table C.3 in Appendix C.

4.6.3 Scattering Strength vs. Grazing Angle of Incidence

In the final stage of my analysis in this Chapter, I compute the variation of the scattering strength as a function of the grazing angle of incidence and frequency. This is done by focusing at different points in the gray patch shown in Fig. 4-12. Each arc centered at the source defines the loci of constant grazing angle of incidence. The farther we move away from the source, the shallower the grazing angle of incidence. The segment of available reverberation data limited the range of grazing angles to 12^o to 30^o, and azimuth angles to -30^o to 145^o. For each arc centered at the source, I calculated the scattering strength at discrete points on the arc corresponding to a given grazing angle of incidence in steps of 10 m, followed by subsequent averaging of the results. This yields an estimate of the mean scattering strength as a function of grazing angle of incidence. Once again, I have averaged the results over the four shots,

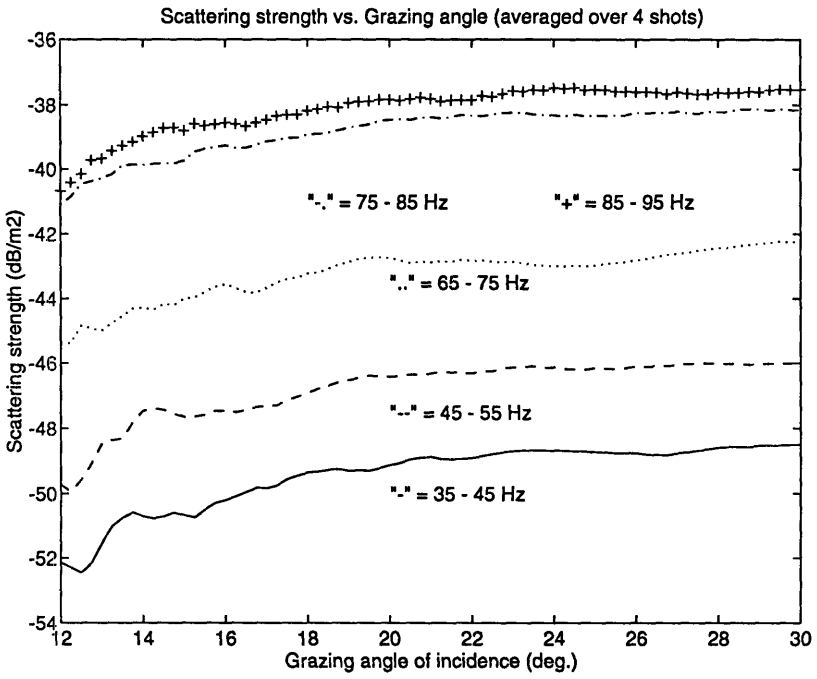

Figure 4-20: Scattering strength as a function of frequency and grazing angle of incidence.

and the results are shown in Fig. 4-20. We observe that in general, scattering strength increases with grazing angle of incidence. This is in agreement with Lambert's law according to which the scattering strength increases as $\sin\theta$, where θ is the grazing angle of incidence. Moreover, as we have previously seen, scattering strength also increases with frequency.

4.7 Summary

In this Chapter, I have formulated the methodology which I shall use to analyze the field experimental data. As discussed in the Introduction, I shall use Matched Field Processing methods to solve this complex multi-parameter estimation problem. As stated there, to make the analysis more manageable I divided the estimation problem into two parts - identification of feature, and subsequent evaluation of its scattering characteristics. In this Chapter, I investigated the first part of this problem. I used nearfield beamforming techniques to estimate the scattering behavior of rough ice, as

well as to identify and isolate prominent features.

The most outstanding contribution of this Chapter was to develop a methodology by which to adaptively combine the outputs of the horizontal array and the vertical arrays. The simulated volumetric array thus obtained had optimum properties in terms of resolution and sidelobe suppression. The results obtained using matched field processing are of higher resolution than those obtained previously using plane-wave beamforming [47]. My focusing results demonstrated that even with a simplified model of the scatterers, I was able to come up with very reasonable estimates of scattering strength. The levels observed here are consistent with those reported elsewhere in the literature. Secondly, I was also able to elucidate the scattering behavior of the protuberances under ice, which may be summarized as -

- In general, scattering levels increase with increasing frequency.
- Scattering levels increase with grazing angle of incidence, and seems to be consistent with Lambert's law.
- Most importantly, scattering is a frequency selective process, i.e., features respond strongly only at frequencies where their sizes and orientation match the characteristics of the incident acoustic field.

The main intent of this Chapter was to identify discrete protuberances or "hot spots" under the ice. These will now be used in the second stage of the MFP scheme, in Chapter 5, where I will evaluate its individual scattering behavior as a function of grazing of scatter. I will also compare the results from experimental data with those from an approximate model, whose formulation will be based on the results of the analysis of Chapter 2.

Chapter 5

Comparisons between analytical model and experimental data

5.1 Overview

The analysis in the previous Chapter involved the solution to the first part of my Matched Field parameter estimation methodology. In this Chapter, I devote my analysis to the second part of the problem, i.e., the evaluation of the spatial scattering characteristics of a single protuberance under the ice canopy. From my focusing plots in the previous Chapter, I was able to identify and isolate discrete scatterers in various frequency bands for patches of ice located both N-E and S-W relative to the apex of the arrays. For the purpose of illustration, I will focus my attention of the feature that was identified to scatter strongly at the grid point corresponding to (980,890) in the N-E patch in the 50 Hz frequency band.

The investigation in the Chapter consists of two main sections. In the first I develop an approximate analytical model for a typical three-dimensional protuberance under the ice. In the second, I shall use the experimental data to make some comparisons between theory and experiment. Using this dual analysis, I hope to develop an appreciation for the physics of three-dimensional scattering from any large-scale

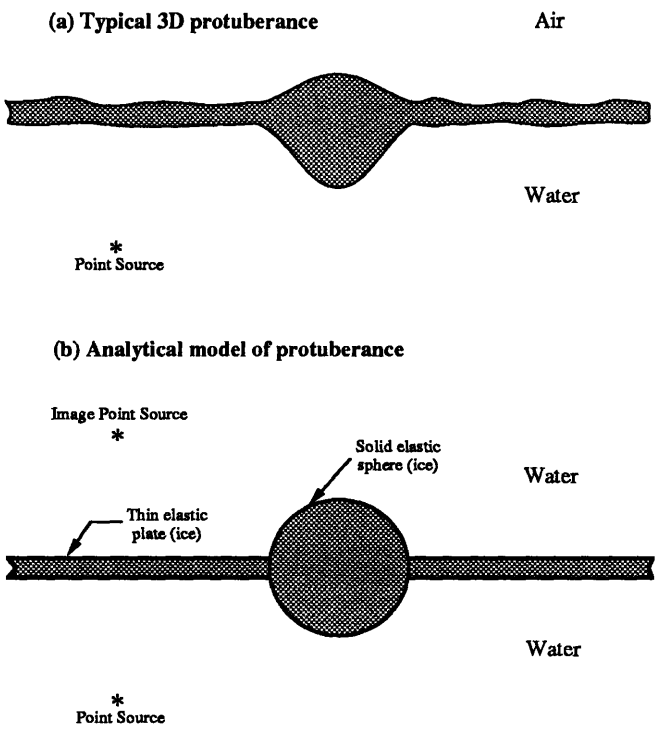

Figure 5-1: (a) Pictorial representation of a typical large three-dimensional feature under the ice sheet. (b) Analytical model of the protuberance. The pressure release surface at the ice-air interface is approximated by including an image point source.

feature under the Arctic ice sheet.

5.2 Analytical model of a three-dimensional protuberance under ice

In this section, I construct an approximate analytical model of scattering from a three-dimensional protuberance under the ice sheet. Previous analyses [8, 9] have modeled these, for example, as a hemispherical protuberance on an infinite plane. These analyses had the shortcomings of not accounting for the elasticity of the ice plate. As a significant improvement in modeling capabilities, my prototype of the feature is a solid elastic sphere attached to a thin elastic plate along its equatorial plane. Fig. 5-1(a) shows the pictorial representation of a typical large-scale feature, or "hot spot", under the Arctic ice canopy. Note that the ice plate is not of uniform thickness,

and may comprise of an abundance of such features, many close to one another. Any such large projection from the ice into the water will also have a substantial mass of ice, or sail, projecting out into the air as shown pictorially in Fig. 5-1. This is because these features are created by large sheets of ice colliding with each other. When two such blocks of ice collide, the sheets are forced together and the breaking blocks of ice create the protuberance and its projection into the air. It is also to be noted that this mass of ice does not necessarily comprise one single feature. In fact, it is not uncommon to see many smaller features cemented to the same general area giving the illusion of one large "hot spot".

In Fig. 5-1(b) I have shown one of the possible analytical ways of realizing the idealized environmental model which could possibly be used in my analysis to represent this protuberance. The details of the methodology for modeling scattering from the completely submerged coupled model were presented earlier in Chapter 2. However, now I need to modify the model presented there to account for the free-surface at the ice-air interface. It is well known in Acoustics that a free-surface can be modeled as a 'negative' reflector of sound [52], where we position a negative image source symmetrically about the surface ($z = 0$) to be simulated as a free surface. The total field Q_t is then synthesized from the contributions from both the real source Q_r located at (x, y, z), and the image source Q_i located at $(x, y, -z)$ as

$$Q_t = Q_r(x, y, z) - Q_i(x, y, -z) \quad .$$

Following this strategy, I assume I can approximate the air-ice interface as a free-surface modeled by including a negative image source, as shown in Fig. 5-1(b), with the total scattered field then being computed as

$$p_t = p_r - p_i \quad , \tag{5.1}$$

where p_t represents the total scattered field, p_r is the scatter from the plate-sphere coupled structure due to the real source located at $(r_0, \theta_0, \varphi_0)$, and p_i is the scattered

pressure due to the image source located at $(r_0, \pi - \theta_0, \varphi_0)$.

Evidently this is not an exact solution because of the excitation of elastic waves in the plate and sphere. Consider for example the shear waves. As these have an anti-symmetric and a symmetric component (with respect to θ), the anti-symmetric part does not cancel at the simulated pressure-release boundary. Recall that the total scattered pressure from the completely submerged coupled model depends on both the associated Legendre function $P_n^m(\cos\theta)$ and its derivatives. While P_n^m is symmetric with respect to θ, its derivatives are not. The expressions for stresses on the sphere involve both P_n^m and its higher order derivatives. Therefore, by including a negative image source the stresses at the upper hemispherical surface are not canceled out. A more exact analysis would require the application of a stress distribution on the entire upper surface of the plate-sphere coupled model such that all resulting stresses vanish there. This would involve an integral equation formulation and is a very involved procedure. The work required would be a thesis in its own right, and therefore I choose not to pursue this approach. However, the idealized environmental model that I have presented may be viewed as a first order approximation in representing the real scattering scenario. In the next section, I will also discuss some other alternate methods that could possibly be adapted to model the air-ice interface. Moreover, as my results will demonstrate, this model performs reasonably well in describing the qualitative nature of the three-dimensional scattered field. It also helps us elucidate the difference between two-dimensional and three-dimensional scatter as I will demonstrate in the section that follows.

5.2.1 Comparison with Boundary Element Method (BEM) results

As a first step in my analysis, I decided to compare the bistatic scattered field from my analytical model of a protuberance under the ice sheet (including the image source) with that from a Boundary Element (BEM) formulation of scattering from a half-cylindrical protuberance on an infinite elastic plate. I compare my results with

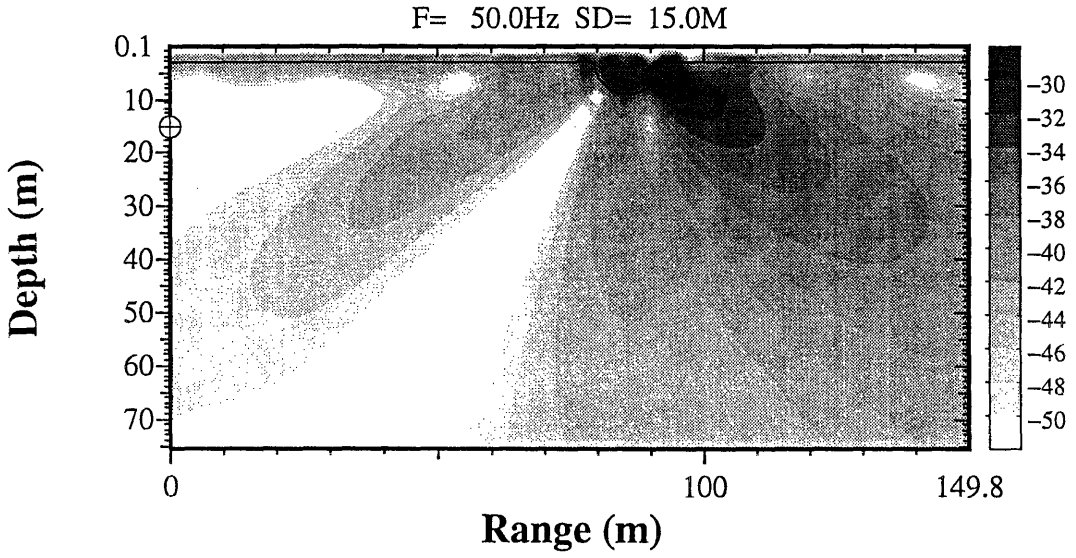

Figure 5-2: Contours of transmission loss for scattering from the two-dimensional protuberance using BEM for f = 50.0 Hz. The source is located at (0.0,-15.0). (Adapted from *Computational Ocean Acoustics* [53], Fig. 7.16, courtesy H. Schmidt.)

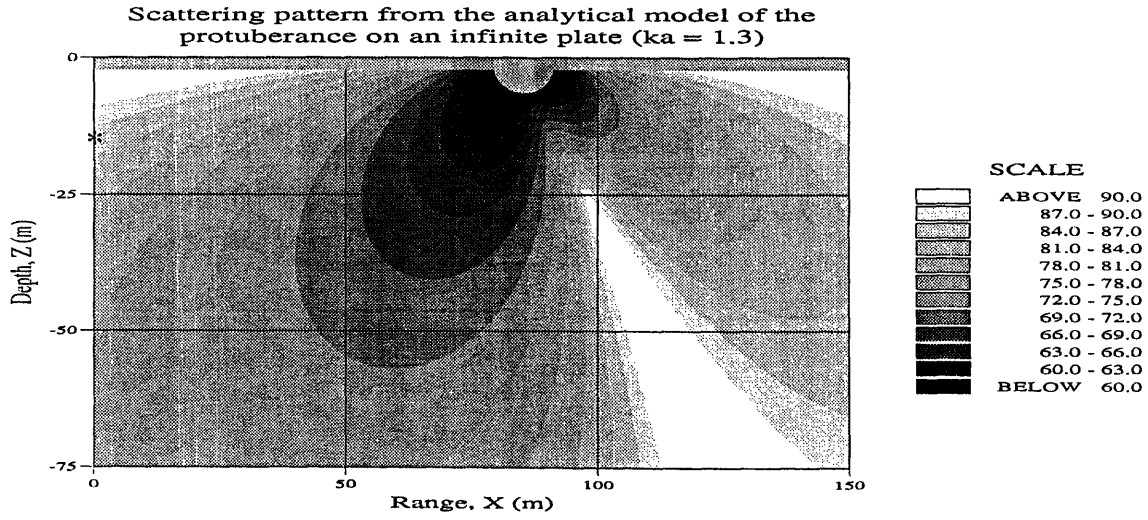

Figure 5-3: Contours of transmission loss for scattering from the three-dimensional protuberance using the analytical model for f = 50.0 Hz. The source is located at (0.0,-15.0).

those presented in Ref. [53]. However, it must be pointed out that the scattering scenario modeled there is two-dimensional in nature while my analytical model is three-dimensional. This comparison will also serve the purpose of delineating the difference between scattering in a two-dimensional scattering environment versus a three-dimensional one.

The results presented in Ref. [53] are a function of range and depth. Therefore, to make a meaningful comparison, I shall compute the scattered field from my theoretical model in a plane passing through the source, and the center of the sphere. The plate is assumed to be 3 m thick, while the protuberance is 6 m in radius. The source is located at a depth of 15 m, and horizontal range of 85.5 m corresponding to a grazing angle of incidence of 10^o. The material properties of the ice are the same as mentioned before, the only difference being that water is assumed to have a sound speed of 1430 m/s. Fig. 5-2 shows the bistatic scattering pattern from the BEM formulation for a frequency of 50 Hz or $ka = 1.3$. The plot shows contours of constant Transmission Loss (TL), i.e.,

$$TL = -20 \log \frac{|p_t(r,z)|}{|p_0|} \quad \text{[dB re 1 } m\text{]} \quad . \tag{5.2}$$

Transmission loss is the sum of the loss due to geometrical spreading and that due to attenuation, reflection and scattering [53]. Therefore, lower values of transmission loss correspond to higher levels of scatter. We observe the characteristic quadrupolar beampattern with higher scatter in the forward direction. The results from my 3D formulation, as shown in Fig. 5-3, display a similar quadrupolar behavior, but with one significant difference. The three-dimensional model predicts higher backscatter as opposed to the two-dimensional BEM formulation. Note that the difference in levels in transmission loss between the 2D and 3D results. While propagation loss in the 2D scenario is due to cylindrical spreading ($TL = 10 \log r$ dB re 1 m), in 3D it is due to spherical spreading ($TL = 20 \log r$ dB re 1 m).

One could therefore arrive at the conclusion that increasing the dimension of the problem changes the nature of scatter completely. However, one must not hastily settle on this deduction. There are many possible reasons for explaining this discrepancy.

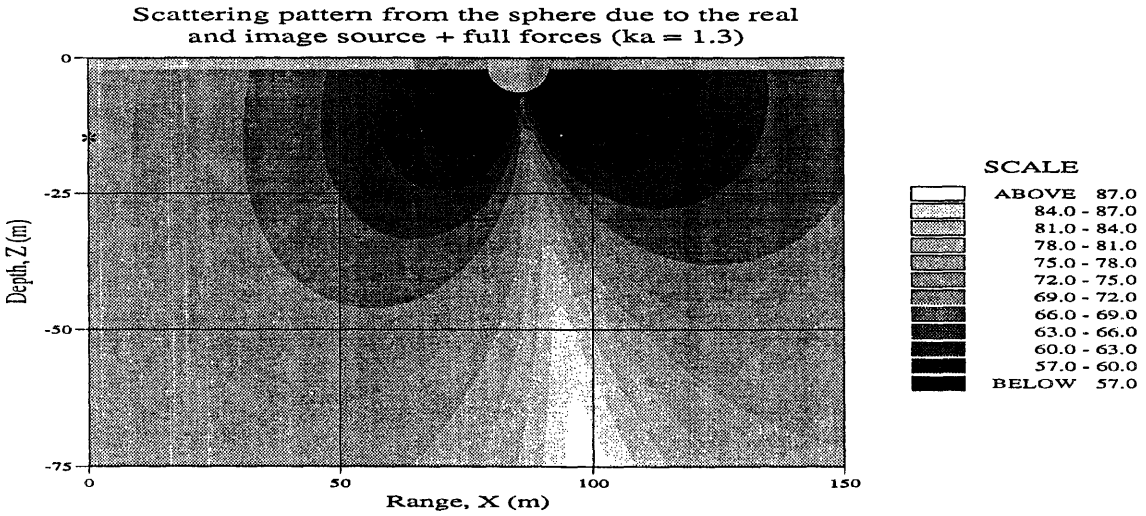

Figure 5-4: Contours of transmission loss for scattering from the three-dimensional protuberance using the analytical model with full contributions from the coupling forces for f = 50.0 Hz. The source is located at (0.0,-15.0).

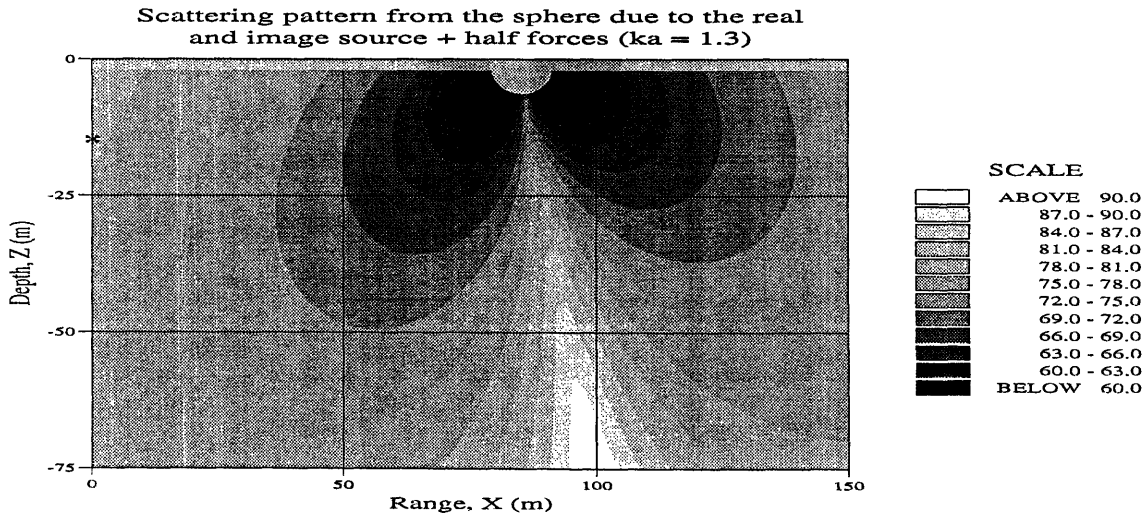

Figure 5-5: Contours of transmission loss for scattering from the three-dimensional protuberance using the analytical model with half the contributions from the coupling forces for f = 50.0 Hz. The source is located at (0.0,-15.0).

The first is that my approximate model which synthesizes the total scattered field from contributions due to the real and image sources is not exactly correct and may not necessarily predict the right qualitative behavior of the scattered field. At this point, it would be prudent to retract our steps and re-evaluate our analytical approximation. The inclusion of the negative image source significantly reduces the contributions from the coupling forces and bending moment. Therefore, one may argue that one should solve for the dynamics of the coupled problem exactly by submerging the whole structure in water, accounting for the scattered pressure from the free sphere only with the image source, and then adding the total contribution from the coupling forces. If I were do this, i.e., compute the total scattered pressure as

$$p_t = p_{s,a}|_{real} - p_{s,a}|_{image} + p_{s,c} \quad ,$$

we would obtain the result shown in Fig. 5-4, where the pressure components were previously described in eqn. (2.2). This result is different from that computed in Fig. 5-3 in the sense that now we observe more or less equal levels of scatter in both the forward and backward directions.

Another school of thought would be to reason that since only half the sphere is actually in contact with water, one should therefore include only half the contributions of the coupling forces and bending moment. In other words, the total scattered pressure should be computed as

$$p_t = p_{s,a}|_{real} - p_{s,a}|_{image} + 0.5p_{s,c} \quad ,$$

and the corresponding results are shown in Fig. 5-5. In comparison to the Fig. 5-4, the results here also predict almost equal scatter in the forward and backward directions too. The levels are about 3 dB lower than those obtained there, and are in fact closer to those observed in Fig. 5-3 for scatter in the backward direction.

In summary, the results from the three possible ways of empirically simulating the pressure-release surface that I have discussed above are not drastically different from

each other, and compare reasonably well in backscatter. As mentioned earlier, the experimental array geometry limits the span of grazing angles of scatter to primarily in the backward direction. And since all three approximations give more or less the same answers in this angular domain, I decided to choose the formulation with the image source for the total coupled problem, and will use that model for all subsequent analysis.

However, note that at this stage we are still in no position to draw any definite inferences regarding the distinction between three-dimensional and two-dimensional scatter. It is intuitive to expect that changing the dimensionality of the problem should completely alter the physical mechanisms of scatter. However, unless we are able to model the air-ice interface with more accuracy, it would be misleading to arrive at any such conclusion from this analysis. However, the theoretical analysis of Chapter 2 should convince us to believe that wave mechanisms involved in 3D scatter are different from those in a 2D formulation, especially with regard to the excitation of horizontally polarized shear (SH) modes. It must also be pointed out that, in general, a more intricate interference pattern would be observed in the spatial distribution of the scattered field if one were to include the contributions due to the radiation of the elastic modes traveling in the plate.

Fig. 5-6 shows the results from my analytical formulation with the image source for a higher frequency, i.e., f = 100 Hz. In this case, we begin to see higher levels of scatter in the forward direction. In fact, the scattering pattern here resembles more closely the 2D result obtained using BEM for $f = 50.0$ Hz. These results can also be explained by considering the scattering beampattern from the free submerged sphere alone as shown in Fig. 5-7. The beampattern has been computed in the plane of the source and the sphere. This figure clearly shows why we obtain the trends we observed in the range vs depth contour plots. At 50 Hz, the free sphere scatters primarily in the backward direction. Even after adding the contribution due to the image source, the dominant scatter is in the backward direction. However, at a frequency of 100 Hz, the free sphere has a dipolar-like scattering pattern, with higher scatter in the forward

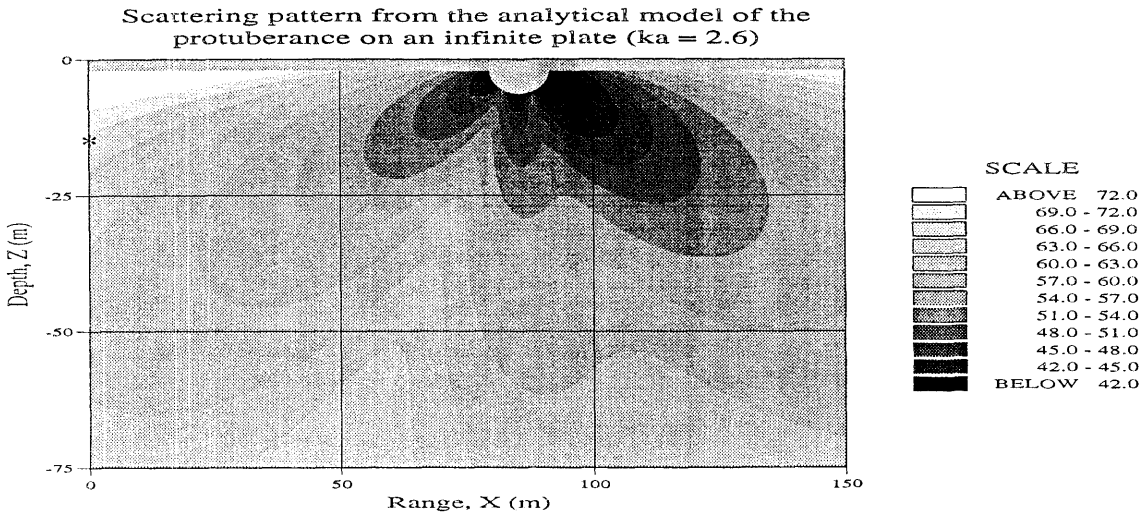

Figure 5-6: Contours of transmission loss for scattering from the three-dimensional protuberance using the analytical model for f = 100.0 Hz. The source is located at (0.0,-15.0).

direction. Therefore, on adding the image source, we still observe the dominance of the lobe from the image source in the forward direction resulting in higher forward scatter.

5.2.2 Analytical realizations of scatter from a single protuberance under Arctic ice

In this section, I present some simulations of the scattering pattern from my realization of the protuberance under ice for various frequencies. Therefore, the results presented in this section consist of the sum of the contributions from the real source and its negative image. In all my results, I assume the sphere to be of radius 10 m, and attached to a 3 m thick ice plate. The source is assumed to be positioned at (-1120,0) and at a depth of 250 m, while the sphere is located at the origin of the coordinate system. The receivers are located on a horizontal plane at a depth of 60 m below the ice cover. I chose this scenario as it closely resembles the geometry of the field experiments, in particular, that of the crossed horizontal hydrophone array. This is what the hydrophones on the crossed horizontal array would have seen if we were able

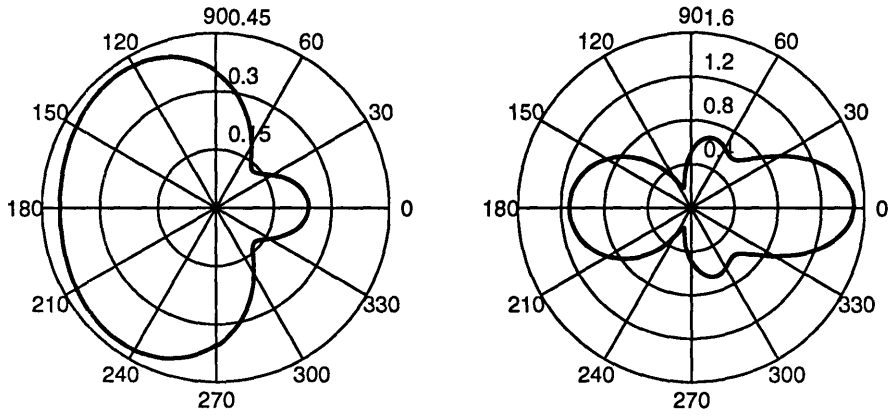

Figure 5-7: Scattering beampattern from the elastic sphere only for $ka = 1.3$ and 2.6. Backscatter is to the left and forward scatter to the right.

to steer the array vertically upwards.

I shall present the results for four frequencies, f = 30 Hz, 50 Hz, 80 Hz, and 100 Hz. This set of frequencies covers the whole frequency spectrum ($f < 100Hz$) which is of interest for propagation in the Arctic Ocean waveguide. Note that in the absence of the plate, the results would be dependent on the non-dimensional frequency parameter ka only. In other words, scatter from a 10 m sphere at 50 Hz would be identical to that of a 5 m sphere at 100 Hz. However, in the presence of the plate, this should not be the case as the dynamics of the attached plate is also frequency dependent ($\propto kh$).

Fig. 5-8 shows the bistatic scattering pattern as a function of range in the X and Y directions for $f = 30$ Hz. Note that as opposed to my previous results which plotted contours of constant transmission loss, here I have plotted the scattered field after removal the geometrical spreading term. It is more prudent to do this in this context as this will reveal the bistatic scattering pattern from the isolated feature. We observe the familiar deformed quadrupolar scattering pattern, and as discussed previously, at this frequency, the scatter is predominantly in the backward direction. The pattern resembles a deformed quadrupole due to the interference between the

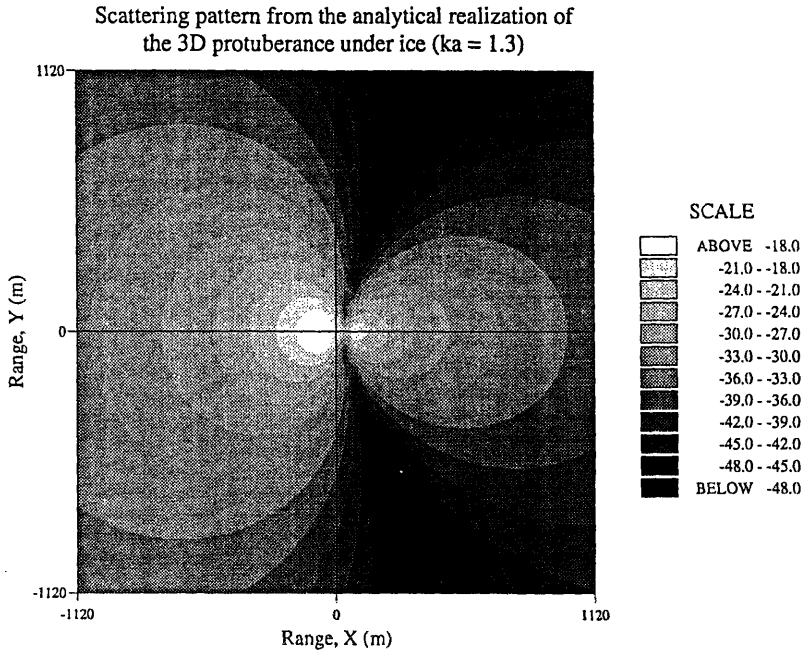

Figure 5-8: Bistatic scattering pattern from my simulation of the three-dimensional protuberance under ice for f = 30.0 Hz on a horizontal plane located 60 m below the ice canopy. The source is located at (-1120,0).

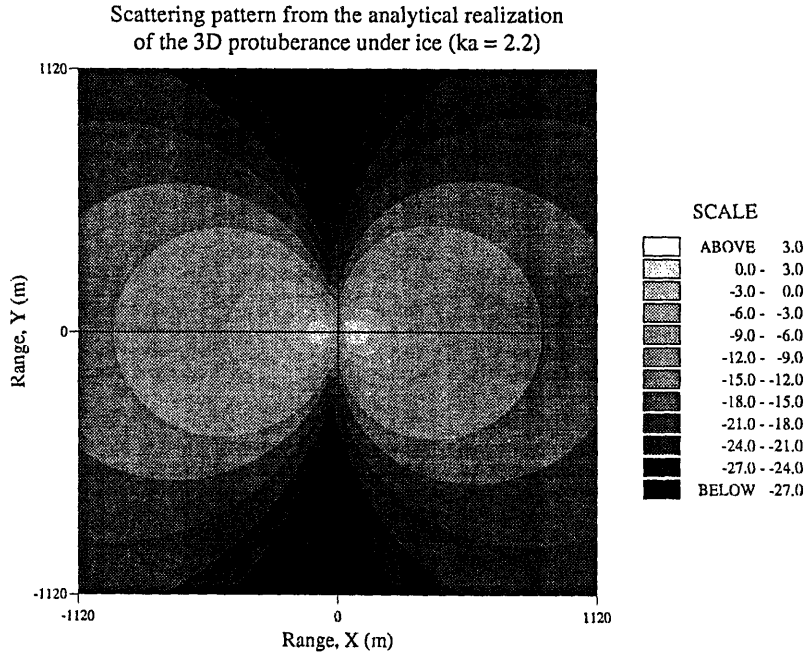

Figure 5-9: Bistatic scattering pattern from my simulation of the three-dimensional protuberance under ice for f = 50.0 Hz on a horizontal plane located 60 m below the ice canopy. The source is located at (-1120,0).

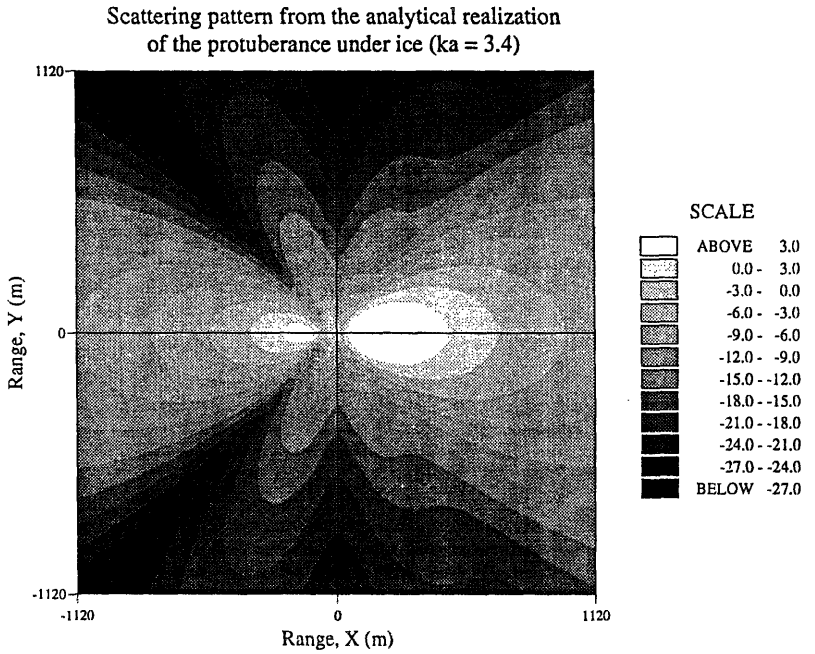

Figure 5-10: Bistatic scattering pattern from my simulation of the three-dimensional protuberance under ice for f = 80.0 Hz on a horizontal plane located 60 m below the ice canopy. The source is located at (-1120,0).

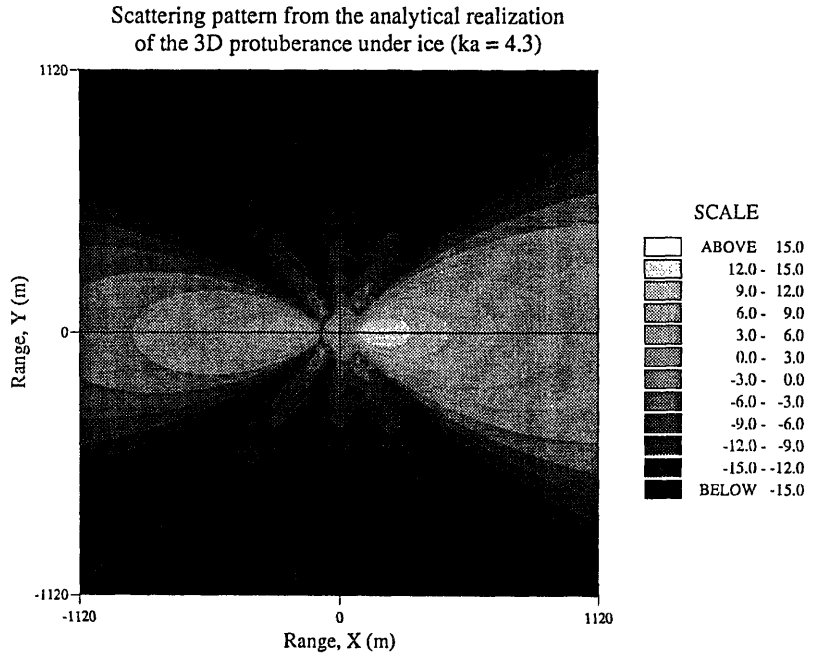

Figure 5-11: Bistatic scattering pattern from my simulation of the three-dimensional protuberance under ice for f = 100.0 Hz on a horizontal plane located 60 m below the ice canopy. The source is located at (-1120,0).

dipole and quadrupole components of the total scattered field. On increasing the frequency to 50 Hz, as shown in Fig. 5-9, the beampattern becomes symmetric with respect to forward and backscatter. The forward lobe, and the lobe in the backward direction, are more or less of the same magnitude. The beampattern almost resembles that of a true quadrupole. Stepping up in frequency to 80 Hz, we begin to observe a more intricate pattern in the scattered field. Scatter is predominantly in the forward direction, with some leakage of energy broadside to the source-sphere axis as shown in Fig. 5-10. Finally, I plot the scattered field at a frequency of 100 Hz, and we observe the incident acoustic energy being re-radiated primarily in the forward direction.

To recapitulate, these results demonstrate that in the mid-frequency regime ($ka \sim O(1)$), the scattering pattern from a three-dimensional protuberance is primarily quadrupolar in nature. This agrees with the observations of Fricke [13, 24] who analyzed scattering from two-dimensional features of various shapes and sizes using both numerical (Finite Difference) and experimental data. This then validates my model for the replica field in the Matched Field Processing I carried out in Chapter 4 to identify and isolate features under the Arctic ice canopy. A more exact MFP algorithm would incorporate the scattering pattern from my analytical model as the replica field. At low frequencies, the contributions from the dipole component may be significant enough to cause a modulation of the quadrupolar term as was evident from Fig. 5-8. It is hypothesized that higher resolution focusing results of the under-surface of the ice may be obtained using this more detailed analysis.

5.3 Experimental data analysis

In this section, I revert to the second stage in my Matched Field parameter estimation methodology and make estimates of the scattering characteristics of a single feature under the ice canopy from the reverberation data. Simultaneously, I shall make some comparisons between the data and the results from my analytical realization of the protuberance. As mentioned earlier, for the purpose of illustration, the focal point of

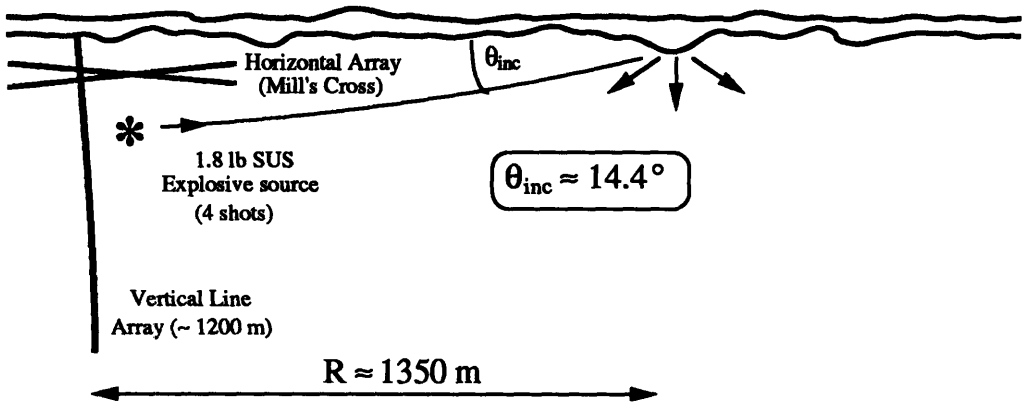

Figure 5-12: Experimental geometry of source, protuberance, and long vertical and crossed horizontal arrays.

this part of the analysis will be the discrete scatterer isolated earlier at the grid point (980,890). This feature is approximately located in a region N-E relative to the apex of the horizontal array.

5.3.1 Scattering pattern from an isolated feature

The reverberation data from the long vertical array was used to determine its polar (vertical) directivity while the data from the crossed horizontal array was used to compute its scattering pattern in the azimuthal (horizontal) direction. The vertical array has a limited aperture of 50^o in the vertical, and the azimuthal angles subtended at the receivers by the protuberance vary from 4.8^o to 7.2^o, or a mean angle of 6.0^o. Here, I have implicitly assumed the source to be located at the origin of the azimuthal coordinate system. The salient reason for choosing a scatterer in an region N-E relative to the apex of the arrays is that the plane of tilt of the long vertical array also lies in this direction. Therefore, the variation of the azimuthal angle at the sensors on the array will not be very significantly different. Also, the array is positioned such that it receives the scattered field in the backward direction at a distance of about 1350 m from the discrete feature as shown in Fig. 5-12. On the other hand the horizontal array spans an azimuthal angular region of about 60^o, i.e., from -20^o to 40^o. Also, since the sensors of the horizontal array are located at a mean depth of 60 m, the

polar angle of scatter at all the sensors is clustered around a very small angle, with a mean value of 5^o. The point source is located at a distance of 1150 m, and is incident on the scatterer at a grazing angle of 14.4^o.

The approach for estimating the scattered pressure from the reverberation data is similar to that outlined in Section 4.6. In this case, however, I do not normalize the scattered pressure with the ensonified area. Secondly, at each frequency, I use the replica fields generated from my analytical realization of the protuberance under ice using the real and image source. In other words, I make no simplifying assumptions about the scattering pattern, and use the radiation pattern from my theoretical model. Also, in the matched field estimation of the signal from the scatterer $s(t)$, I used each of the long vertical and horizontal arrays independently to evaluate the polar and azimuthal scattering patterns. Then, denoting the Fourier Transform of the signal from the scatterer by $S(f)$, the directivity of the scatterer as a function of the polar (θ) and azimuthal (φ) angles are then estimated as

$$B(f,\theta_i,\varphi_c) = \frac{X_i(f,\theta_i,\varphi_c)}{S(f)} \quad , \quad B(f,\theta_c,\varphi_i) = \frac{X_i(f,\theta_c,\varphi_i)}{S(f)} \quad , \tag{5.3}$$

and the normalized scattered intensity (I) is given by

$$I(f,\theta,\varphi) = 20\log|B(f,\theta,\varphi)| \quad [\text{dB re } 1\ m] \quad \cdot \tag{5.4}$$

Here θ_i and φ_i are the angles subtended by the scatterer at the i^{th} receiver on the vertical and horizontal arrays respectively. Also, φ_c and θ_c are the azimuthal and polar angles (assumed constant) subtended by the protuberance at the vertical and horizontal array respectively. Note that since the sensors are located at discrete points in the angular domain, it is not possible to obtain the beampattern as a continuous function of θ and φ.

There is a caveat in this processing scheme. I have inherently made the assumption that all the energy arriving within this two-way travel time window at the receivers is from this feature only. However, due to the geometry of the scattering scenario, there

will be multiple contributions from all such large features lying within the elliptical ensonified area as was discussed in Section 4.6. I reduce this ambiguity by using the beamformed signal instead of the source waveform directly. As the contributions from other scatterers will not add up coherently, we can expect to obtain a good estimate of the signal $s(t)$ from the feature, limited by the resolution of the array. However, $x_i(t)$ will still contain contributions from all scatterers within the ensonified area. This is a primary limitation of the experimental data. This point must be borne in mind when I compare the results from field data and the theoretical model.

However, if instead of an omni-directional source, the experiments had been conducted with an array of sources, it would have been possible to steer the source array directly at the feature of interest. This would have tremendously improved the quality of the data available for comparisons. Thus, when making comparisons with my analytical model, one should bear this limitation in mind. In spite of not being able to make quantitative comparisons with utmost confidence, we can still glean some insight into the scattering phenomena by making qualitative judgments.

The material properties for the analysis that follows are exactly the same as were stated earlier. I shall restrict my analysis once again to the four frequencies - 30 Hz, 50 Hz, 80 Hz, and 100 Hz - which cover the frequency regime of interest to us. Also, as in the case of scattering strength analysis, I shall average the results from experimental data over 10 Hz frequency bands.

Polar Directivity

I begin by first considering the polar (θ) directivity of the protuberance. As stated earlier, I use the received signal at the long vertical array for this part of the analysis. Fig. 5-13 shows the results from experimental data, and the analytical model for $f =$ 30 Hz. The experimental data values have been denoted by the symbol "+", and I have plotted the data from all four shots. Assuming the scattered field to consist of contributions from only the dipolar and quadrupolar terms, I model the data as

$$p_s = c_1 \sin\theta + c_2 \sin 2\theta \ ,$$

where θ is the grazing angle of scatter, and c_1 and c_2 are the relative amplitudes of the polar components. As was demonstrated earlier, this approximation is justified for low frequencies. The solid curve represents the least-squares best fit through the data points. Also, I have plotted the scattered field from my analytical realization of scattering from the approximate analytical model for two values of the radius of the sphere, $a = 10\ m$ (dashed line) and $20\ m$ (dashed-dotted line). At a frequency of 30 Hz, these two curves correspond to ka values of 1.3 and 2.6 respectively. The reason for plotting two curves is that since I have no information regarding the actual size of the feature, there is no reason to arbitrarily chose a value of a for making comparisons with the experimental values. Moreover, the two values of a at each frequency may be interpreted as two curves for different values of ka at that frequency. Therefore, these two curves will demonstrate how the scattered field varies with ka, and give us an indication regarding what the scattered field should be quantitatively, were the experimental data values from a single scatterer only.

However, even though the trends in the data and the analytical simulations are somewhat similar, there is no agreement in magnitudes. This could be attributed to the fact that at this frequency, this feature does not scatter quite as prominently as is evident from Fig. 4-15. The disagreement in magnitude can also be ascribed to the fact that the analytical model assumes a single scatterer, while the experimental values include contributions from all features located within the ensonified area or the region of ambiguity. Another possible explanation is that while the results from the experimental data have been averaged over 10 Hz frequency bands, the analytical estimates are essentially single frequency results. Moreover, observe the large standard deviations in the experimental values for a given angle of scatter. The variation at any given angle is due to the data from the four different shots. In contrast to the horizontal array data, as shown later, the vertical array data seems to have more fluctuations over shots. This would lead us to have less confidence in the values presented here. However, the discrepancy in magnitude is very large to be resolved by these arguments.

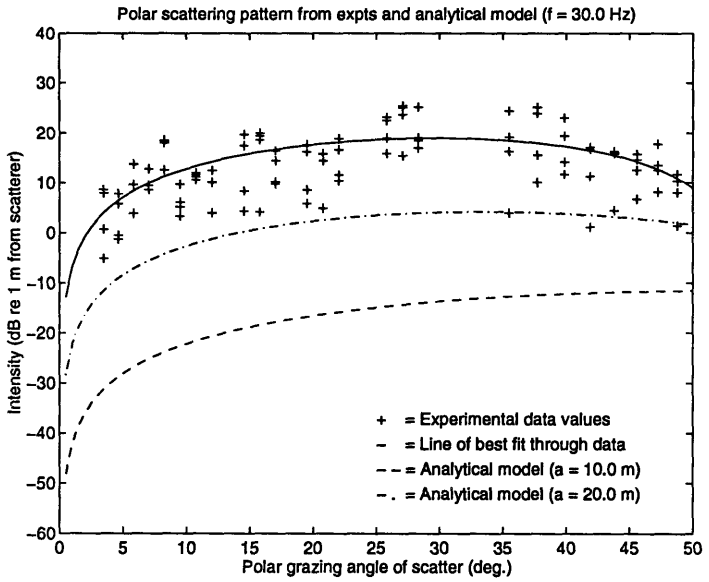

Figure 5-13: Polar (vertical) beampattern from experiments and analytical model for a frequency of $f = 30\ Hz$. The values from experiments are represented by (+), while the solid line (-) represents the best fit line through the data. The results from the analytical model are denoted by the dashed line (- -) for $a = 10.0\ m$ and by the dashed-dotted line (- .) for $a = 20.0\ m$.

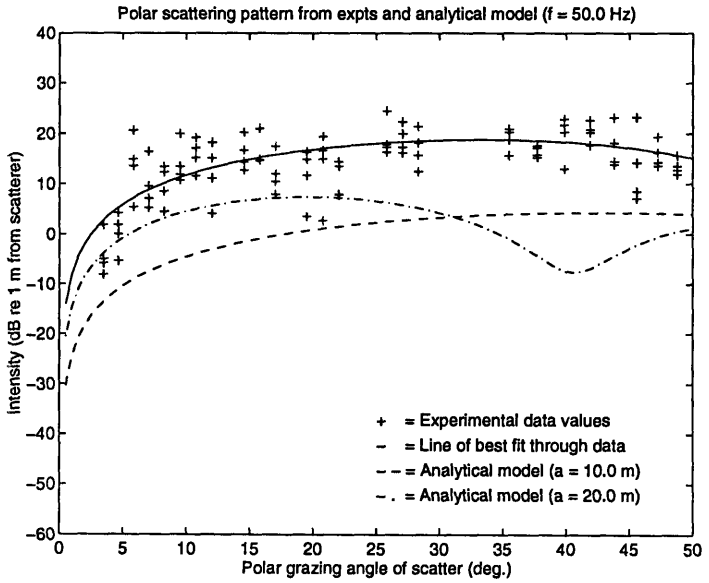

Figure 5-14: Polar (vertical) beampattern from experiments and analytical model for a frequency of $f = 50\ Hz$. The values from experiments are represented by (+), while the solid line (-) represents the best fit line through the data. The results from the analytical model are denoted by the dashed line (- -) for $a = 10.0\ m$ and by the dashed-dotted line (- .) for $a = 20.0\ m$.

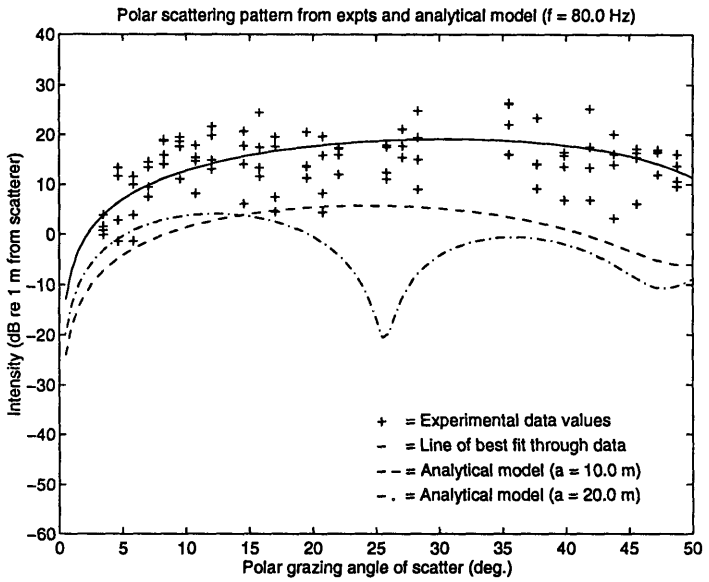

Figure 5-15: Polar (vertical) beampattern from experiments and analytical model for a frequency of $f = 80\ Hz$. The values from experiments are represented by (+), while the solid line (-) represents the best fit line through the data. The results from the analytical model are denoted by the dashed line (- -) for $a = 10.0\ m$ and by the dashed-dotted line (- .) for $a = 20.0\ m$.

Fig. 5-14 shows the data and the model for a frequency of 50 Hz. The dashed and dashed-dotted lines represent the analytical solutions with $a = 10\ m$ and 20 m respectively. We observe better qualitative agreement between data and model at this frequency. Referring back Fig. 4-13, this should not be astonishing. There we observed this feature to scatter most strongly in this frequency band. Therefore, the dominant contribution in the time window at each of the receivers must be from this scatterer. In other words, data values at this frequency more closely resemble the "true" values that would have been observed were this feature the only contributor. Therefore, we conclude that this is the best frequency to compare data with model. The figure shows excellent agreement in both trend and behavior of the scattered field, with the better match being obtained with the 10 m sphere. However, the analytical estimate is still about 15 dB below the the mean of the experimental values This is the best evidence available to us that my analytical realization of the protuberance does in fact model the attributes of the "real" scattering scenario moderately well, especially at small angles of scatter in the backward direction.

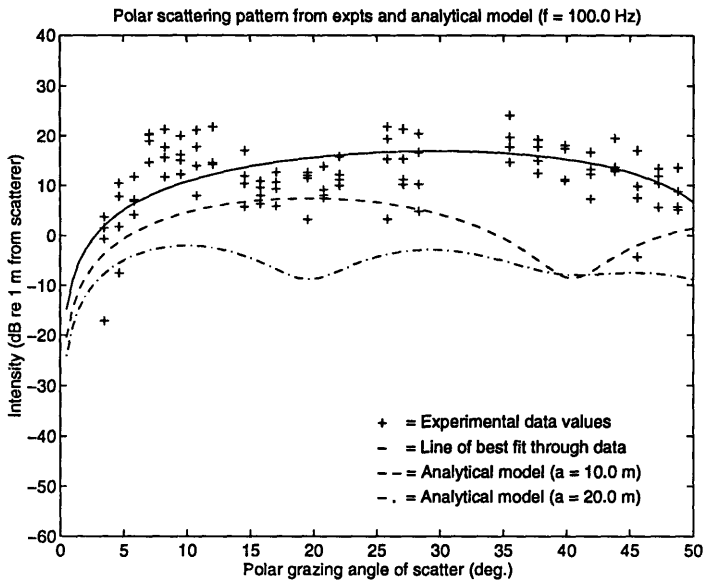

Figure 5-16: Polar (vertical) beampattern from experiments and analytical model for a frequency of $f = 100\ Hz$. The values from experiments are represented by (+), while the solid line (-) represents the best fit line through the data. The results from the analytical model are denoted by the dashed line (- -) for $a = 10.0\ m$ and by the dashed-dotted line (- .) for $a = 20.0\ m$.

Fig. 5-15 and Fig. 5-16 show the comparison between data and model for two higher frequencies, i.e., f = 80 Hz and 100 Hz. As in the case for the 30 Hz band, the 80 Hz results barely show some agreement, whereas the 100 Hz results seem to agree qualitatively with the analytical predictions. However, note the high variance exhibited by the experimental values. It must be pointed out that similar variances over the four different shots were reported by Hayward and Yang [47] in the estimates presented in their paper (see Ref. [47], Fig. 6.(a)). Due to this high variance in their reverberation spectral estimates, they averaged their results over all available incident angles. This is not what I intend to do in this thesis. My inference is that there seems to be some discrepancy in the data acquired by NRL on the vertical arrays. Therefore, at this stage, it is not conclusive to say whether my model predicts the right levels until I can make comparisons with more reliable reverberation data. One possible way to rectify this shortcoming in the vertical array data would be to compare the reverberation estimates from the horizontal and vertical arrays separately, shot by shot. Subsequently, I should have the most confidence in the vertical array data for

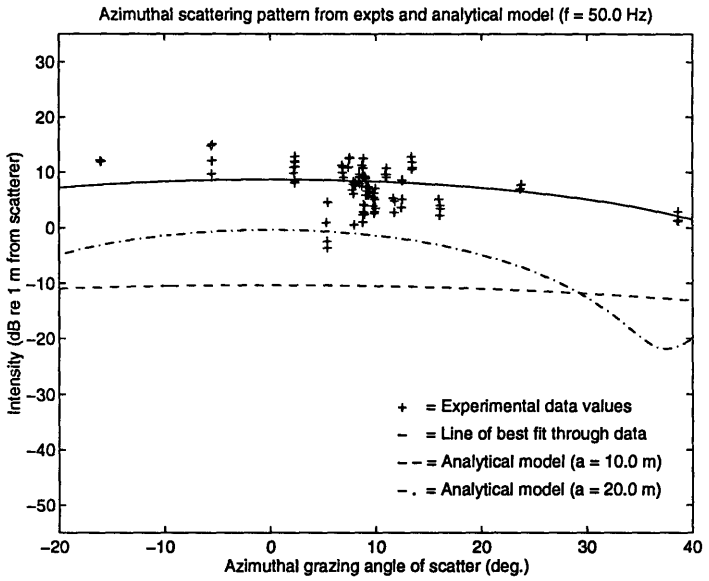

Figure 5-17: Azimuthal (horizontal) directivity from experiments and analytical model for $f = 50\ Hz$. The values from experiments are represented by (+), the solid line (-) represents the best fit line through the data. The results from the analytical model are denoted by the dashed line (- -) for $a = 10.0\ m$, and the dashed-dotted line (- .) for $a = 20.0\ m$.

that shot which most closely matches the estimates from the horizontal array. This will be done in a future work.

Azimuthal Directivity

Finally, the azimuthal (φ) directivity from the experimental data is estimated from the received signal at the horizontal array. However, this array does not sample the field uniformly in azimuth. As the data will show, the receivers are clustered around small angles of azimuth, in particular around 9^o. This is primarily due to the receivers on the N-E leg of the crossed horizontal array, which make small angles ($7^o - 10^0$) with the protuberance. Therefore, this is not very reliable for making comparisons over a wide range of angles since the data points available at larger angles are relatively few. However, for the sake of completeness, I shall present my results for the horizontal directivity too.

Fig. 5-17 shows the results from experimental data and the analytical model for $f = 50\ Hz$. Once again, the experimental data values have been denoted by the symbol

"+". Retaining only the first two terms in the modal summation representation of the scattered field, I assume the azimuthal variation of the scattered field to be given by

$$p_s = c_3 \cos\varphi + c_4 \cos 2\varphi \ ,$$

where φ is the azimuthal angle of scatter, and c_3 and c_3 are the relative amplitudes of the modal components. As in the case of polar directivity, the solid curve represents the least-squares best fit through the data points. Also, plotted is the analytical scattered field for two values of the radius of the sphere, $a = 10\ m$ (dashed line) and $20\ m$ (dashed-dotted line). The plot clearly shows the severe limitations of the experimental data, with most values being clustered around 9^o azimuth, and only a couple of points for the higher angles. Note that in contrast to the values at high azimuthal angles which have very low variance, the values at smaller angles have large deviations from the mean. The main reason behind this large divergence, as mentioned before, is due to the N-E leg of the crossed horizontal array. Another reason is that I have selected equal segments of the reverberation data from each channel with the same length of time window, i.e., the same number of time samples. Depending on the relative locations of the source, protuberance and receivers, each sensor will receive energy from a different ensonified region. The different ensonified regions may contain different scatterers, both in number and type. This inconsistency may also be explained by noting that the feature is not necessarily azimuthally symmetric. Therefore, for each source-protuberance-receiver orientation, the azimuthal angle of incidence for each receiver will also vary. This will in turn result in an amplitude modulation of the received scattered field.

Fig. 5-18 shows the results for a higher frequency band $f = 100\ Hz$. The plot reveals that once again, there are large discrepancies between model and data. Once again, the discrepancies may be explained by following a reasoning similar to that for the 50 Hz frequency band. However, it is instructive to compare the scattered pressures observed on the horizontal and vertical arrays to see if the estimates made from these two different measurement systems are consistent. I did this by including

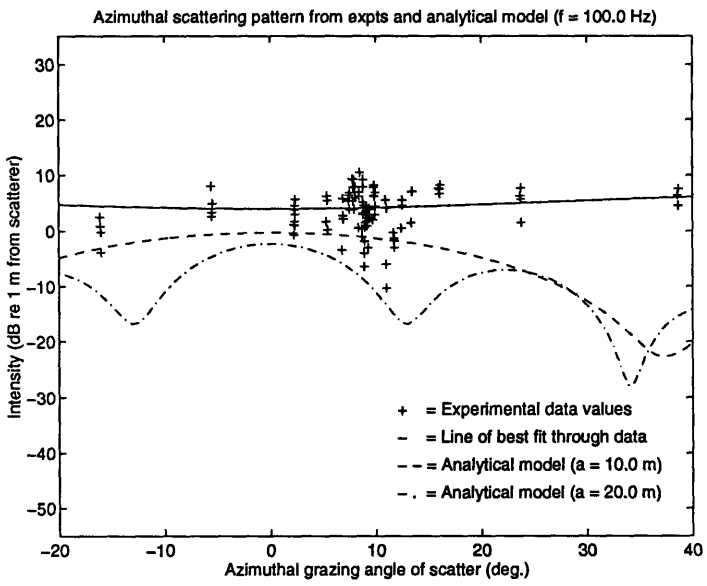

Figure 5-18: Azimuthal (horizontal) directivity from experiments and analytical model for $f = 100\ Hz$. The values from experiments are represented by (+), the solid line (-) represents the best fit line through the data. The results from the analytical model are denoted by the dashed line (- -) for $a = 10.0\ m$, and the dashed-dotted line (- .) for $a = 20.0\ m$.

receivers on the two arrays that were within the following range of scattering angles -

$$4.5^o < \varphi < 7.5^o \quad , \quad 3.5^o < \theta < 6.5^o \quad .$$

Averaging the values estimated from the two arrays separately, I obtain the results shown in Table 5.1. The table shows the mean values for the angles φ and θ at the sensors selected for the averaging process, along with the corresponding statistics of

Statistics of Horizontal and Vertical array estimates					
f (Hz)	Array	$\bar{\varphi}_o$	θ_o	Mean (dB)	SD (dB)
50.0	Horizontal	6.4	5.0	6.4	6.1
	Vertical	7.1	5.2	6.9	8.7
100.0	Horizontal	6.4	5.0	3.2	3.2
	Vertical	7.1	5.2	5.2	6.1

Table 5.1: Mean and Standard Deviation (SD) of the scattered pressure levels observed at the horizontal and vertical array receiver systems.

the scattered pressure for two frequency bands $f = 50.0\ Hz$, $100.0\ Hz$. The results indicate that the mean values of the scattered pressure obtained on the two arrays compare extremely well.

5.3.2 Total intensity from multiple scatterers

The comparison between data and model that was conducted in the previous section is not really meaningful since the experimental values are due to multiple scatterers, while the analytical model computes the scattered intensity from a single feature. In this section, I present an example demonstrating how one could possibly attempt to make some better comparisons, especially with respect to the intensity levels.

For the discrete scatterer analyzed in the previous section, the typical values of ensonified areas for the receivers are approximately $A \sim 1.2 \times 10^6\, m^2$. From Fig. 4-13 and Fig. 4-19, we observe that the average number of strong features in a $600m \times 600m$ area in the 50 Hz frequency band is about 12. Therefore, the number of strong scatterers N within the typical ensonified area is given by

$$N = \frac{1.2 \times 10^6}{600 \times 600} \times 12 \sim 40 \quad .$$

Then, assuming incoherent addition of energy, the total scattered intensity from the whole ensonified area is given by

$$\begin{aligned} I_{total} &= I_{single} + 10 \log 40 \\ &= I_{single} + 16dB \quad . \end{aligned} \tag{5.5}$$

This value of 16 dB compares extremely well with the observed difference between the data values and the theoretical model with $a = 10.0\ m$ in Fig. 5-14. A more exact analysis would require the statistics of the distribution of three-dimensional protuberances under the ice. However, there is a caveat to be noted here. All features within the ensonified area do not subtend the same angle of scatter at the receiver.

Therefore, the results obtained with this approach would also be approximate.

5.4 Summary

In this Chapter, I presented an approximate model for an analytical realization of a three-dimensional protuberance under the ice, and compared my results with those obtained independently via a BEM formulation. Next I presented some results for the bistatic scattering pattern from an isolated protuberance using my approximate solution. In the final stage of the analysis, I made comparisons between my analytical realization and results from field experimental data. The salient results of this Chapter are summarized below -

- The analytical realization using the image source displays the right qualitative behavior, especially at low grazing angles of scatter. In fact, the spatial pattern of the scattered field clearly depicts the quadrupolar nature of the beampattern. The relative strengths of forward scatter to scatter in the backward direction seems to increase with increasing frequency.

- It was not possible to draw definite inferences regarding the distinction between 2D and 3D scatter. A more exact representation of the free-surface may bring us a step closer to making this delineation. However, the 3D formulation allows the inclusion of SH waves as opposed to a 2D analysis.

- Comparisons with experimental data provided no definite conclusions regarding how well our analytical model compared with experiments. This was primarily due to the severe limitations of the available data. However, we obtained encouraging results in the vertical directivity in the 50 Hz frequency band.

- It was also demonstrated how the intensity levels due to multiple scatterers from the experimental data may be compared with those from the analytical model of a single feature.

In a nutshell, the analytical realization seems to predict the right scattering characteristics as it models all the relevant physics of the idealized problem where simplifications were made with respect to the continuously rough interface, distribution of protuberances, and the porosity of ice. However, to demonstrate that the right levels of the scattered field are obtained, I need to compare my model with data from a more controlled environment. This will then allow us to emphatically state our confidence in the validity of the analytical model.

Chapter 6

Conclusions and Future Work

6.1 Overview

In this final chapter, I begin by recapitulating all the results I have obtained so far and discuss their implications on our understanding of three-dimensional scattering. Next, I dwell on the significant contributions made by this thesis in the context of the theoretical modeling, and development of some of the data analysis techniques I have implemented. Then I move on to a brief discussion on some possible applications of the work reported in this thesis. Finally, I make some recommendations for future work in the context of analytical modeling, as well as the conducting of appropriate field and laboratory experiments for generating data suitable for comparison with my analytical model.

6.2 Discussion and Summary

In this thesis, I have carried out a theoretical and experimental investigation of three-dimensional scattering. The theoretical analysis provided an understanding into the underlying physical mechanisms of the scattering phenomena. I discussed the dynamics of the interaction between the plate and the sphere, and demonstrated the impor-

tance of the elastic waves in the re-radiated field. In particular, the three-dimensional analytical modeling included the horizontally polarized shear (SH) modes which can exist only in a 3D scenario. It was also shown that the dominant contribution to the scattered field arises from the in-plane coupling forces as the attached elastic plate primarily constrains the lateral motions of the sphere in the horizontal plane. I also investigated the relative importance of compressional, shear and flexural waves in influencing scatter. It was shown that the excitation of flexural waves in the plate depends on both frequency and grazing angle of incidence of the acoustic field.

However, the most significant result from my theoretical analysis is the frequency selective nature of the scattering phenomenon. In other words the acoustic scatter from protuberances, or "hot spots", depends on the non-dimensional frequency parameter ka, where k is the acoustic wavenumber in water. This was made evident from my analysis in Chapter 2, where the scattered field from the plate-sphere coupled structure was shown to be a modulation of that from the free submerged sphere. Other than the contributions to the radiated field by the interaction forces and bending moment at selective frequencies, the total scattered field resembles that due to the free sphere only. In other words, the effects of the attachment of the plate to the sphere are manifested in a frequency selective manner. This result was reinforced from my matched field analysis of the experimental data in Chapter 4, where my focusing plots clearly showed the frequency selectivity of the scattered field. Features that scattered strongly in some frequency bands, did not do so at others.

This leads me to answer the issue I started to address at the beginning of this thesis - what is the importance of the attachment of the plate to the protuberance. In other words do the elastic waves, in particular the in-plane waves, in the ice play a decisive role in defining the spatial scattering patterns. As was repeatedly evident from the results of my theoretical formulation, the most dominant contribution to the scattered field was due to the in-plane radial force and thus, the excitation of compressional and shear waves in the plate. Flexural waves play an important role predominantly at low frequencies ($f < 35Hz$), and angles of incidence close to beam

incidence. With increasing frequency, the bending impedance of the plate increases, and therefore the energy injected into the flexural modes at the attachment also rolls-off. Previous analysis by Lepage [7] also demonstrated similar results. On another note, it can be speculated that when the protuberance deviates from the axisymmetric geometry, shear wave excitation will become the dominant phenomena in defining the characteristics of the scattered field. However, this still remains to be seen.

Most importantly, within the enclaves of the available field experimental data, I was unable to conclusively corroborate my theoretical solutions. This was due to the severe limitations of the data available for processing. Even though I estimated the horizontal and vertical directivities of scatter from an individual scatterer, there was no quantitative comparison in magnitude between data and model. This was primarily due to the fact that while the analytical results were computed for a single scatterer scenario, the experimental results were due to a multitude of such features. The qualitative nature of the results demonstrated that the field resembles a quadrupolar pattern. This was also observed by Fricke [13] who used a 2D version of Finite Differences to model scattering from features of various shapes and sizes. He also demonstrated the validity of his observations by conducting laboratory experiments using an aggregation of polypropylene chips to build a half cylinder [24].

Finally, comparisons of my analytical solutions with those obtained independently via a BEM formulation showed that the right qualitative behavior is duplicated in my theoretical analysis. The significant difference between the two analyses was that while the BEM results predict high scatter in the forward direction, even at moderate frequencies, my results showed that the relative strength of forward scatter to scatter in the backward direction is frequency dependent. However, it must be borne in mind that this difference could also be attributed to my approach of simulating the pressure-release boundary condition at the ice-air interface which has its own associated limitations.

6.3 Contributions

The overall contribution of this thesis to the study of Acoustics has been to provide a fundamental understanding of the physics of three-dimensional seismo-acoustic (fluid-elastic) scatter. The exact analysis can be addressed using numerical methods. However, as these are computationally expensive, I developed an approximate theoretical model which contained all the physics pertinent to 3D scatter. Simultaneously, I analyzed field experimental data to elucidate the nature of scatter in real environments. I was also able to compare and contrast the results from these two independent investigations. The prominent contributions of this thesis are outlined below -

- Development of a complete theoretical solution to the three-dimensional modeling of scatter with all the relevant physics.
- Formulation of a two step Matched Field parameter estimation methodology to identify and isolate discrete features, and estimate the spatial scattering characteristics of individual protuberances.
- I devised an adaptive array processing technique to combine the outputs from the horizontal and vertical arrays. The resulting volumetric array had optimum properties in terms of resolution and sidelobe suppression.
- I demonstrated that there is some evidence for frequency selectivity in three-dimensional scatter. This was corroborated by independent investigations of experimental data and an analytical model.

6.4 Applications

One can think of many applications where the analysis carried out in this thesis could be of use. One particularly interesting application that comes to mind, is in the area of Medical Imaging. Presently, the methodology to identify tumors or cancerous growths

is to use ultrasound and look at initial returns, This technique yields very low Signal-to-Noise Ratios (SNR). An interesting approach would be to perhaps model the tumor as a protuberance on an otherwise smooth surface. This model could then be used in a matched field approach to significantly increase the SNR. The details of the matched field approach were discussed in Chapter 4 of this thesis.

6.5 Recommendations for future work

How can a thesis end without having recommendations. A thesis is like an interim report of an ongoing project, and there is always room for improvements. I can identify three areas in the context of the work reported in this thesis that definitely warrant some additional work in the future. The first is with respect to theoretical analysis, while the second deals with improvements in the Matched Field estimation procedure. The third pertains to the conducting of field and laboratory experiments.

6.5.1 Analytical model

There is definitely some room for improving my theoretical model of three-dimensional scatter. The first is in regard to the propagation of elastic waves in the plate. The exact analysis requires the excitation of the plate modes by the incident acoustic field, especially the flexural and compressional waves. These waves would then travel towards the plate-sphere junction, while simultaneously radiating back into the fluid by phase-matching, and scatter into the fluid. Their inclusion follows an approach exactly similar to the one I developed for sphere modes coupling into the plate. The flexural waves will still be evanescent in this frequency regime, and therefore, the only significant radiation would be due to the compressional waves. My analysis in Chapter showed that the displacements at the ring due to these plate waves is significantly smaller compared to those due to the sphere. Hence, these will not alter the plate-sphere interaction dynamics at the attachment ring. However, the elastic modes excited in the plate due to the coupling forces would cause additional radiation

into the fluid as these propagate away from the junction. These would also make the scattered beampattern more rich, and we should begin to see some interference between the contributions from the coupling forces and these plate waves, which will leak energy into the fluid as they propagate in the plate.

Secondly, it would also be interesting to demonstrate if the shape of the three-dimensional feature plays any significant role in characterizing scatter. My strong suspicion is that any deviation from a regular geometry will strongly excite shear waves in the plate. Finally, it would be rewarding to be able to come up with a better method of approximating the free-surface at the ice-air interface. I suggested three empirical ways of doing this in Chapter 5. All three approximations gave the same results in backscatter but strong qualitative discrepancies in forward scatter. Even though the image source method provides the right qualitative description, I suspect that the levels are not quite correct.

6.5.2 Matched field analysis of scattering strength

The MFP algorithm that I used in Chapter 4 to evaluate scattering strength under ice assumed that the features radiate like quadrupoles. A more exact analysis would mandate the use of the exact replica fields from my analytical model at each frequency. This would make the processing more time consuming as I would no longer be able to take advantage of time-domain processing as the replica fields would be frequency dependent. However, this would yield higher resolution estimates of scattering strength and the locations of discrete features under the ice canopy.

6.5.3 Field and laboratory experiments

The ultimate validation of my analysis will come from conducting true bistatic experiments either in the field or in a laboratory. The other alternative is to generate numerical data using three-dimensional FD or BEM. If conducting experiments in the laboratory, with a uniform plate, use of a larger aperture is recommended so that the

array samples both forward and backscatter. This is the only way of making true comparisons of scattering patterns.

Finally, in all my analysis I was truly handicapped lacking any information on the size of the protuberances. It would be especially helpful to conduct these experiments in a controlled environment where both the thickness of the plate and the size of the protuberance are known. In collecting data in field experiments, it would be appropriate to have an image of the under side of the ice, perhaps by deploying an Autonomous Underwater Vehicle (AUV). Also, instead of using one omni-directional source, the analysis would be significantly improved by firing an array of sources, which could then be steered to any possible look direction under the Arctic ice cover.

Appendix A

Spherical Coordinate Greens Functions for Ring Tractions in a solid unbounded medium

A.1 Introduction

Excitation of a solid elastic medium by a ring load or traction is a problem of interest when dealing with forced excitation of structures in spherical coordinates. This becomes even more pertinent when analyzing problems involving forcings without axisymmetry. Examples where one needs to consider excitation of structures by ring loads include the acoustic scattering from a plate attached externally to a sphere as shown in Chapter 2, or scattering from a spherical shell with an internal deck plating or a ring stiffener. The need for explicit solutions to the Green's function problem arises especially when using full three-dimensional elastodynamic modeling of the interaction between coupled structures. Ring force solutions are also useful since the stresses and displacements due to a point force excitation may be readily synthesized by summing the appropriately phased ring force solutions.

Green's functions in spherical coordinates have been previously derived for a simple

point source positioned in a spherically stratified environment [33], and for axisymmetric (azimuthal order $m = 0$, $\theta = 0$) point loads pushing in various directions in Cartesian coordinates [54]. These solutions are not useful for the analysis of contact problems where two structures are coupled along attachment rings. In such cases, explicit solutions for ring traction loads pushing in various directions are required, and we need to solve the ring force problem directly by explicitly retaining the dependence on the azimuthal coordinate φ. Recently, expressions for admittances for a *zero* azimuthal order ($m = 0$) radial ring force on a spherical shell were presented in [55]. In this Appendix, I shall derive closed form solutions for excitation by ring traction loads of any azimuthal order m.

I begin by formulating the Green's function problem in Section A.2. Retaining the dependence on the azimuthal coordinate (φ) increases the complexity of the problem since, as I will show in Section A.3, the stresses and displacements contain a mixed dependence on the order of the associated Legendre functions $P_n^m(\cos\theta)$ and $P_{n-1}^m(\cos\theta)$, where n is the index of summation over the polar angle (θ) and m is the corresponding index of summation for the azimuthal angle (φ). I will employ a linear transformation of the tangential components of stress and displacements to derive explicit analytical solutions.

A.2 Formulation

The equations governing the motions of a homogeneous isotropic elastic solid are given by [36, 37]

$$(\lambda + 2\mu)\nabla\nabla\cdot\vec{u} - \mu\nabla\times\nabla\times\vec{u} + \rho\vec{f} = \rho\frac{\partial^2\vec{u}}{\partial t^2} \quad , \tag{A.1}$$

where $\vec{u}$ is the displacement vector and $\vec{f}$ is the body force per unit mass of material. Following [34], I write the displacement potential in terms of three scalar fields, ϕ, ψ and $\check{\chi}$, i.e.,

$$\vec{u} = \nabla\phi + \nabla\times(\hat{e}_r r\psi) + \nabla\times\nabla\times(\hat{e}_r r\check{\chi}) \quad , \tag{A.2}$$

where the first term is the longitudinal part of the solution, and the other two are the transverse parts. The three potentials may then be shown to satisfy the following scalar wave equations

$$\begin{aligned} \nabla^2\phi &= \frac{1}{c_\alpha^2}\frac{\partial^2\phi}{\partial t^2} \quad , \\ \nabla^2\psi &= \frac{1}{c_\beta^2}\frac{\partial^2\psi}{\partial t^2} \quad , \\ \nabla^2\check{\chi} &= \frac{1}{c_\beta^2}\frac{\partial^2\check{\chi}}{\partial t^2} \quad , \end{aligned} \tag{A.3}$$

where c_α and c_β are compressional and shear wave speeds respectively, and are given by

$$c_\alpha = \sqrt{\frac{\lambda+2\mu}{\rho}} \, , \; c_\beta = \sqrt{\frac{\mu}{\rho}} \quad .$$

Assuming an $\exp(-i\omega t)$ harmonic time dependence (suppressed henceforth), the potentials then also satisfy the following Helmholtz equations

$$\begin{aligned} \left(\nabla^2+\alpha^2\right)\phi &= 0 \quad , \\ \left(\nabla^2+\beta^2\right)\psi &= 0 \quad , \\ \left(\nabla^2+\beta^2\right)\chi &= 0 \quad , \end{aligned} \tag{A.4}$$

where $\alpha = \omega/c_\alpha$ and $\beta = \omega/c_\beta$ denote the wavenumbers for the compressional and shear waves respectively. Also, I have normalized the potential $\check{\chi}$ by the shear wavenumber β as $\chi = \beta\check{\chi}$ so that the dimensions of ϕ, $r\psi$ and $r\chi$ are the same. The Laplacian operator ∇^2 in spherical coordinates is given by

$$\nabla^2 = \frac{1}{r^2}\frac{\partial}{\partial r}\left(r^2\frac{\partial}{\partial r}\right) + \frac{1}{r^2\sin\theta}\frac{\partial}{\partial\theta}\left(\sin\theta\frac{\partial}{\partial\theta}\right) + \frac{1}{r^2\sin^2\theta}\frac{\partial^2}{\partial\varphi^2} \quad .$$

When the Helmholtz equations are separated in spherical coordinates as $R(r)\Theta(\theta)\Phi(\varphi)$, the radial equation has the form

$$\frac{1}{r^2}\frac{d}{dr}\left(r^2\frac{dR}{dr}\right)+\left(\left\{\begin{array}{c}\alpha^2\\ \beta^2\end{array}\right\}-\frac{n(n+1)}{r^2}\right)R=0 \quad ,$$

and its solutions are the spherical Bessel functions (j_n, n_n) [29]. The solutions with respect to the spatial variables θ and φ are obtained by expanding the potentials in terms of Spherical Harmonic Waves (SHW) as [56, 57]

$$\begin{aligned}\tilde{f}(n,m) &= \int_{-\pi}^{\pi} e^{-im\varphi}d\varphi\int_0^{\pi} f(\theta,\varphi)P_n^m(\cos\theta)\sin\theta d\theta \quad ,\\ f(\theta,\varphi) &= \frac{1}{2\pi}\sum_{m=-\infty}^{\infty} e^{im\varphi}\sum_{n=|m|}^{\infty} a_{mn}\tilde{f}(n,m)P_n^m(\cos\theta) \quad ,\end{aligned} \tag{A.5}$$

where

$$a_{mn}=\frac{(2n+1)}{2}\frac{(n-m)!}{(n+m)!} \quad ,$$

and

$$P_n^{-m}(\cos\theta)=(-1)^m\frac{(n-m)!}{(n+m)!}P_n^m(\cos\theta) \quad .$$

Note that I have interchanged the summations over the n and m orders as I shall be computing the Green's functions due to excitation by ring traction loads of arbitrary azimuthal order m, followed by subsequent summation to synthesize the Green's functions due to point force excitation. Correspondingly, I define the Fourier Transform (FT) pair with respect to the spatial variable φ as

$$\begin{aligned}\hat{f}(m) &= \int_0^{2\pi} f(\varphi)e^{-im\varphi}d\varphi \quad ,\\ f(\varphi) &= \frac{1}{2\pi}\sum_{m=-\infty}^{\infty}\hat{f}(m)\,e^{im\varphi} \quad .\end{aligned}$$

Assuming the traction load to be located at the ring defined by ($r=r_0$, $\theta=\theta_0$, $-\pi<\varphi<\pi$) as shown in Fig. A-1, I then need three potentials to represent the displacement field $\vec{u}$, with components (u_r, u_θ, u_φ), inside the ring and three to represent $\vec{u}$ outside,

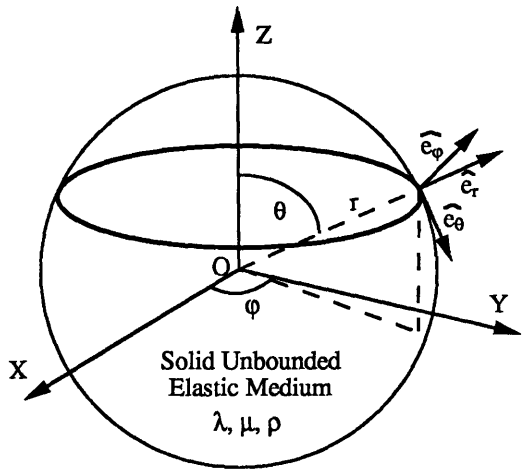

Figure A-1: Geometry for ring force excitation of a solid unbounded elastic medium of material properties λ, μ and ρ.

i.e.,

$$\begin{aligned}
\vec{u} &= \nabla\phi_I + \nabla\times(\hat{e}_r r\psi_I) + \frac{1}{\beta}\nabla\times\nabla\times(\hat{e}_r r\chi_I) \\
&\quad \cdots 0 \le r < r_0 \quad , \\
&= \nabla\phi_E + \nabla\times(\hat{e}_r r\psi_E) + \frac{1}{\beta}\nabla\times\nabla\times(\hat{e}_r r\chi_E) \\
&\quad \cdots r_0 < r < \infty \quad ,
\end{aligned} \tag{A.6}$$

where the subscripts I and E denote the interior and exterior regions. I therefore need six equations to constrain these potentials at $r = r_0$, $\theta = \theta_0$. The first three are obtained from continuity of displacement, while the other three are obtained by accounting for the jump in stresses at $r = r_0$, $\theta = \theta_0$.

The normal and shear stresses involved in the boundary conditions are given by Hooke's law as [36, 37]

$$\begin{aligned}
\tau_{rr}(r,\theta,\varphi) &= \lambda\nabla\cdot\vec{u} + 2\mu\frac{\partial u_r}{\partial r} \quad , \\
\tau_{r\theta}(r,\theta,\varphi) &= \mu\left(\frac{1}{r}\frac{\partial u_r}{\partial\theta} - \frac{u_\theta}{r} + \frac{\partial u_\theta}{\partial r}\right) \quad , \\
\tau_{r\varphi}(r,\theta,\varphi) &= \mu\left(\frac{1}{r\sin\theta}\frac{\partial u_r}{\partial\varphi} - \frac{u_\varphi}{r} + \frac{\partial u_\varphi}{\partial r}\right) \quad ,
\end{aligned} \tag{A.7}$$

and the corresponding displacement components u_r, u_θ and u_φ are given by

$$\begin{aligned}
u_r(r,\theta,\varphi) &= \frac{\partial\phi}{\partial r} + \frac{1}{\beta}\left[\frac{\partial^2(r\chi)}{\partial r^2} - r\nabla^2\chi\right] \\
&= \frac{\partial\phi}{\partial r} + \frac{n(n+1)}{\beta r}\chi \quad , \\
u_\theta(r,\theta,\varphi) &= \frac{1}{r}\frac{\partial\phi}{\partial\theta} + \frac{1}{\sin\theta}\frac{\partial\psi}{\partial\varphi} + \frac{1}{\beta r}\frac{\partial^2(r\chi)}{\partial\theta\partial r} \quad , \\
u_\varphi(r,\theta,\varphi) &= \frac{1}{r\sin\theta}\frac{\partial\phi}{\partial\varphi} - \frac{\partial\psi}{\partial\theta} + \frac{1}{\beta r\sin\theta}\frac{\partial^2(r\chi)}{\partial\varphi\partial r} \quad . \qquad \text{(A.8)}
\end{aligned}$$

Substituting eqn. (A.8) into eqn. (A.7) yields expressions for the stresses in terms of the potentials ϕ, ψ and χ. Note that these expressions for stresses and displacements contain terms which depend on both the associated Legendre function $P_n^m(\cos\theta)$ and its derivative $dP_n^m(\cos\theta)/d\theta$. Recalling the property of associated Legendre functions [58],

$$\frac{d}{d\theta}P_n^m(\cos\theta) = n\cot\theta P_n^m(\cos\theta) - \frac{n+m}{\sin\theta}P_{n-1}^m(\cos\theta) \quad ,$$

we observe that the stresses and displacements therefore have a mixed dependence on the order n of the associated Legendre function. However, if I eliminate this mixed dependence, I can satisfy the boundary conditions more elegantly since the associated Legendre function dependence will drop out and then I will need to satisfy the boundary conditions at each order n only. This is done by employing a linear transformation of the tangential displacements and stresses [59]

$$\begin{aligned}
U &= u_r \quad , \\
V &= -\left[\tfrac{\partial}{\partial\theta}(u_\theta\sin\theta) + \tfrac{\partial u_\varphi}{\partial\varphi}\right]\tfrac{1}{\sin\theta} \quad , \\
W &= \left[\tfrac{\partial}{\partial\theta}(u_\varphi\sin\theta) - \tfrac{\partial u_\theta}{\partial\varphi}\right]\tfrac{1}{\sin\theta} \quad , \\
R &= \tau_{rr} \quad , \\
S &= -\left[\tfrac{\partial}{\partial\theta}(\tau_{r\theta}\sin\theta) + \tfrac{\partial\tau_{r\varphi}}{\partial\varphi}\right]\tfrac{1}{\sin\theta} \quad , \\
T &= \left[\tfrac{\partial}{\partial\theta}(\tau_{r\varphi}\sin\theta) - \tfrac{\partial\tau_{r\theta}}{\partial\varphi}\right]\tfrac{1}{\sin\theta} \quad . \qquad \text{(A.9)}
\end{aligned}$$

As this is a linear transformation of the linearly independent tangential (θ, φ) components, the resulting displacement and stress components are also linearly independent.

Insertion of eqn. (A.9) into eqns. (A.7) and (A.8) yields expressions containing the associated Legendre function $P_n^m(\cos\theta)$ of order n only. Expanding the Helmholtz potentials in terms of Spherical Harmonic Waves (SHW) as

$$\tilde{\phi} = A_{mn} z_n(\alpha r) \ , \ \tilde{\psi} = B_{mn} z_n(\beta r) \ , \ \tilde{\chi} = C_{mn} z_n(\beta r) \quad ,$$

the transformed displacements of order n and m may then be written as

$$\begin{aligned} U &= A_{mn} \frac{d}{dr} z_n(\alpha r) + C_{mn} \frac{n(n+1)}{\beta r} z_n(\beta r) \quad , \\ V &= n(n+1) \left[A_{mn} \frac{z_n(\alpha r)}{r} + \frac{C_{mn}}{\beta} \left\{ \frac{d}{dr} z_n(\beta r) + \frac{z_n(\beta r)}{r} \right\} \right] \quad , \\ W &= n(n+1) B_{mn} z_n(\beta r) \quad , \end{aligned} \tag{A.10}$$

and the three transformed stresses of order n and m may be expressed as

$$\begin{aligned} R &= \frac{2\mu}{r} \left[A_{mn} T_{11} + C_{mn} \frac{T_{12}}{\beta} \right] \quad , \\ S &= \frac{2\mu}{r} n(n+1) \left[A_{mn} T_{21} + C_{mn} \frac{T_{22}}{\beta} \right] \quad , \\ T &= \mu n(n+1) B_{mn} T_3 \quad , \end{aligned} \tag{A.11}$$

where

$$\begin{aligned} T_{11} &= (n^2 + n - \frac{1}{2}\beta^2 r^2) \frac{z_n(\alpha r)}{r} - 2 \frac{d}{dr} z_n(\alpha r) \quad , \\ T_{12} &= n(n+1) \left\{ \frac{d}{dr} z_n(\beta r) - \frac{z_n(\beta r)}{r} \right\} \quad , \\ T_{21} &= \frac{d}{dr} z_n(\alpha r) - \frac{z_n(\alpha r)}{r} \quad , \\ T_{22} &= (n^2 + n - 1 - \frac{1}{2}\beta^2 r^2) \frac{z_n(\beta r)}{r} - \frac{d}{dr} z_n(\beta r) \quad , \\ T_3 &= \frac{d}{dr} z_n(\beta r) - \frac{z_n(\beta r)}{r} \quad . \end{aligned} \tag{A.12}$$

z_n is represented by the spherical Bessel function (j_n) for the interior potentials, and by the spherical Hankel function of the first kind ($h_n^{(1)} \equiv h_n$) for the exterior potentials.

Henceforth, I will carry out our analysis with the transformed displacement and stress components.

A.3 Ring Traction Excitations

In the following sections I shall evaluate the closed form solutions for the Helmholtz potentials due to various ring force and ring bending moment excitations. Denoting the potentials of order n and m by $\tilde{g}(r,m,n)$, where $g = \{\phi, \psi, \chi\}$, the Green's functions for ring excitations of any arbitrary azimuthal order m are computed by summing over the polar order n as

$$\hat{g}(r,m,\theta) = \sum_{n=|m|}^{\infty} a_{mn}\tilde{g}(r,m,n)P_n^m(\cos\theta) \quad , \tag{A.13}$$

where $\hat{g}(r,m,\theta)$ is evaluated at the location of the ring traction load $\theta = \theta_0$. The potentials due to a point load located at (θ_0, φ_0) can then be readily synthesized by summing the appropriately phased ring traction load solutions as

$$g(r,\theta,\varphi) = \frac{1}{2\pi}\sum_{m=-\infty}^{\infty} \hat{g}(r,m,\theta)e^{im\varphi} \quad , \tag{A.14}$$

where $g(r,\theta,\varphi)$ is evaluated at the location of the point load $(\theta = \theta_0, \varphi = \varphi_0)$.

Following Ref. [35], six equations of continuity need to be satisfied at the boundary where the ring traction load is applied - three involving displacements and the other three involving stresses. Continuity of displacements across the ring load at $r = r_0$, $\theta = \theta_0$, yields

$$\begin{aligned}
\lim_{\epsilon\to 0}[U]_{r_0+\epsilon} &= \lim_{\epsilon\to 0}[U]_{r_0-\epsilon} \quad , \\
\lim_{\epsilon\to 0}[V]_{r_0+\epsilon} &= \lim_{\epsilon\to 0}[V]_{r_0-\epsilon} \quad , \\
\lim_{\epsilon\to 0}[W]_{r_0+\epsilon} &= \lim_{\epsilon\to 0}[W]_{r_0-\epsilon} \quad .
\end{aligned}$$

Representing the interior and exterior potentials of order n and m as

$$\tilde{\phi}_I = \tilde{A}_I j_n(\alpha r) \ , \ \tilde{\psi}_I = \tilde{B}_I j_n(\beta r) \ , \ \tilde{\chi}_I = \tilde{C}_I j_n(\beta r) \ ,$$

$$\tilde{\phi}_E = \tilde{A}_E h_n(\alpha r) \ , \ \tilde{\psi}_E = \tilde{B}_E h_n(\beta r) \ , \ \tilde{\chi}_E = \tilde{C}_E h_n(\beta r) \ ,$$

I obtain the first set of three equations between the interior and exterior potentials in the SHW domain as

$$\tilde{A}_I \left[\frac{d}{dr} j_n(\alpha r)\right]_{r=r_0} + \tilde{C}_I \frac{n(n+1)}{\beta r_0} j_n(\beta r_0) = \tilde{A}_E \left[\frac{d}{dr} h_n(\alpha r)\right]_{r=r_0} + \tilde{C}_E \frac{n(n+1)}{\beta r_0} h_n(\beta r_0) \ ,$$

$$\tilde{A}_I \frac{j_n(\alpha r_0)}{r_0} + \tilde{C}_I \frac{1}{\beta} \left\{ \left[\frac{d}{dr} j_n(\beta r)\right]_{r=r_0} + \frac{j_n(\beta r_0)}{r_0} \right\} =$$
$$\tilde{A}_E \frac{h_n(\alpha r_0)}{r_0} + \tilde{C}_E \frac{1}{\beta} \left\{ \left[\frac{d}{dr} h_n(\beta r)\right]_{r=r_0} + \frac{h_n(\beta r_0)}{r_0} \right\} \ ,$$

$$\tilde{B}_I j_n(\beta r_0) = \tilde{B}_E h_n(\beta r_0) \ . \tag{A.15}$$

Note that eqn. (A.15), which represents continuity of displacement, must be satisfied for all traction loads. In the sections that follow, I compute the explicit solutions for the displacement potentials for each ring traction load individually.

A.3.1 Radial (r) direction

I begin by expressing the ring traction load in the radial direction as

$$\tau_r^0(r_0, \theta, \varphi) = T_r \frac{\delta(\theta - \theta_0)}{2\pi r_0^2 \sin\theta} \ , \tag{A.16}$$

where T_r is the total force (N) at the ring, τ_r^0 is the corresponding stress (Nm^{-2}) in the radial direction, and its decomposition into SHW may be shown to be

$$\tilde{\tau}_r^0 \ = \ \int_{-\pi}^{\pi} e^{-im\varphi} d\varphi \int_0^{\pi} T_r(\varphi) \frac{\delta(\theta - \gamma)}{2\pi a^2 \sin\theta} P_n^m(\cos\theta) \sin\theta \, d\theta$$

$$= \hat{T}_r \frac{P_n^m(\cos\gamma)}{2\pi a^2} \quad ,$$

where $\hat{T}_r$ is the Fourier Transform (FT) of T_r with respect to the spatial coordinate φ. This traction load in the radial direction introduces a discontinuity in the radial stress component while the tangential stresses, which are orthogonal to this loading, remain continuous across the ring. Therefore, balancing tractions in the radial direction I obtain $R_E - R_I = R^0$, or

$$\begin{aligned}
\tilde{A}_I T_{11,I} + \tilde{C}_I \frac{1}{\beta} T_{12,I} - \tilde{A}_E T_{11,E} - \tilde{C}_E \frac{1}{\beta} T_{12,E} &= -\hat{T}_r \frac{P_n^m(\cos\theta_0)}{4\pi\mu} \quad , \\
\tilde{A}_I T_{21,I} + \tilde{C}_I \frac{1}{\beta} T_{22,I} - \tilde{A}_E T_{21,E} - \tilde{C}_E \frac{1}{\beta} T_{22,E} &= 0 \quad , \\
\tilde{B}_I T_{3,I} - \tilde{B}_E T_{3,E} &= 0 \quad , \qquad \text{(A.17)}
\end{aligned}$$

where the additional subscripts I and E have been used to mean that the traction-like quantities T_{ij} need to be evaluated in the interior and exterior regions respectively. From eqns. (A.15) and (A.17) we observe that the equations for $\tilde{B}$ are decoupled from those for $\tilde{A}$ and $\tilde{C}$.

Solution Strategy

I begin by noting a very useful Wronskian relationship that can be used in determining the explicit solutions to the Green's function problem, i.e.,

$$j_n(\kappa r_0)\left[\frac{d}{dr}h_n(\kappa r)\right]_{r=r_0} - h_n(\kappa r_0)\left[\frac{d}{dr}j_n(\kappa r)\right]_{r=r_0} = \frac{i}{\kappa r_0^2} \cdot \qquad \text{(A.18)}$$

The solutions for $\tilde{B}$ are found in a relative straight forward manner since their equations are decoupled. Eliminating $\tilde{B}_E$ by substituting the third equation in (A.15) in the third equation in (A.17), I obtain

$$\tilde{B}_I \left\{ h_n(\beta r_0)\left[\frac{d}{dr}j_n(\beta r)\right]_{r=r_0} - j_n(\beta r_0)\left[\frac{d}{dr}h_n(\beta r)\right]_{r=r_0} \right\} = 0 \quad ,$$

or

$$\tilde{B}_I \left\{ \frac{-i}{\beta r_0^2} \right\} = 0 \ .$$

Since $(-i/\beta r_0^2) \neq 0$, therefore,

$$\tilde{B}_I = \tilde{B}_E = 0 \ . \tag{A.19}$$

The solutions to the remaining four simultaneous equations in $\tilde{A}$ and $\tilde{C}$, may be conveniently found by speculating that the solutions will be of the form such that it would be possible to exploit the Wronskian relationship in eqn. (A.18). With this consideration, I assume the solutions to have the following forms

$$\begin{aligned}
\tilde{A}_I &= \tilde{A}_1 \left[\frac{d}{dr} h_n(\alpha r) \right]_{r=r_0} + \tilde{A}_2 h_n(\alpha r_0) \ , \\
\tilde{A}_E &= \tilde{A}_1 \left[\frac{d}{dr} j_n(\alpha r) \right]_{r=r_0} + \tilde{A}_2 j_n(\alpha r_0) \ , \\
\tilde{C}_I &= \tilde{C}_1 \left[\frac{d}{dr} h_n(\beta r) \right]_{r=r_0} + \tilde{C}_2 h_n(\beta r_0) \ , \\
\tilde{C}_E &= \tilde{C}_1 \left[\frac{d}{dr} j_n(\alpha r) \right]_{r=r_0} + \tilde{C}_2 j_n(\alpha r_0) \ ,
\end{aligned} \tag{A.20}$$

where $\tilde{A}_1$, $\tilde{A}_2$, $\tilde{C}_1$ and $\tilde{C}_2$ are the new unknown constants yet to be determined. The reasoning behind this assumption is as follows. Consider the internal potential $\tilde{\phi}_I = \tilde{A}_I j_n(\alpha r)$ which contains the explicit dependence on the spherical Bessel function. If we assume that the $\tilde{A}_I$ is composed of terms with spherical Hankel functions ($h_n(\alpha r)$) and/or their derivatives, we can easily see that each equation in (A.17) will yield terms some of which will drop out and others that will simplify after some algebraic manipulation with the Wronskian. Substituting these assumed forms for the unknown potentials in eqns. (A.20) into the four simultaneous equations in $\tilde{A}_I$, $\tilde{A}_E$, $\tilde{C}_I$ and $\tilde{C}_E$, yields a system of equations whose solutions may be found with relative ease. After some algebraic manipulation, and on recursively using the Wronskian relationship, I obtain the following result for the potentials for a radial ring force of azimuthal order

m

$$
\begin{aligned}
\tilde{\phi}_I &= \frac{i\alpha\hat{T}_r}{2\pi\rho\omega^2}\left[\frac{d}{dr}h_n(\alpha r)\right]_{r=r_0} P_n^m(\cos\theta_0)j_n(\alpha r) \quad , \\
\tilde{\phi}_E &= \frac{i\alpha\hat{T}_r}{2\pi\rho\omega^2}\left[\frac{d}{dr}j_n(\alpha r)\right]_{r=r_0} P_n^m(\cos\theta_0)h_n(\alpha r) \quad , \\
\tilde{\psi}_I &= 0 \quad , \\
\tilde{\psi}_E &= 0 \quad , \\
\tilde{\chi}_I &= \frac{i\beta^2\hat{T}_r}{2\pi r_0\rho\omega^2}h_n(\beta r_0)P_n^m(\cos\theta_0)j_n(\beta r) \quad , \\
\tilde{\chi}_E &= \frac{i\beta^2\hat{T}_r}{2\pi r_0\rho\omega^2}j_n(\beta r_0)P_n^m(\cos\theta_0)h_n(\beta r) \quad . \qquad \text{(A.21)}
\end{aligned}
$$

A.3.2 Polar (θ) direction

Following my analysis in the previous section, I write the ring traction load pushing in the positive θ direction as

$$
\tau_\theta^0(r_0,\theta,\varphi) = T_\theta\frac{\delta(\theta-\theta_0)}{2\pi r_0^2\sin\theta_0} \quad , \qquad \text{(A.22)}
$$

and the corresponding stress components in the transformed domain are found to be

$$
S^0 = -\left[\frac{\partial}{\partial\theta}\left(\tau_\theta^0\sin\theta\right)\right]\frac{1}{\sin\theta} = -T_\theta\frac{\delta'(\theta-\theta_0)}{2\pi r_0^2\sin\theta} \quad ,
$$

$$
T^0 = -\left[\frac{\partial}{\partial\varphi}\left(\tau_\theta^0\right)\right]\frac{1}{\sin\theta} = -\left[\frac{dT_\theta}{d\varphi}\right]\frac{\delta(\theta-\theta_0)}{2\pi r_0^2\sin^2\theta} \quad .
$$

Expressing S^0 and T^0 in terms of SHW, I obtain

$$
\begin{aligned}
\tilde{S}^0 &= -\frac{\hat{T}_\theta}{2\pi r_0^2}\left[-\frac{d}{d\theta}P_n^m(\cos\theta)\right]_{\theta=\theta_0} \quad , \\
\tilde{T}^0 &= -\frac{im\hat{T}_\theta}{2\pi r_0^2}\left[\frac{P_n^m(\cos\theta_0)}{\sin\theta_0}\right] \quad . \qquad \text{(A.23)}
\end{aligned}
$$

Continuity of displacement yields exactly the same set of equations as in (A.15). Balancing tractions,

$$\begin{aligned}
\tilde{A}_I T_{11,I} + \tilde{C}_I \frac{1}{\beta} T_{12,I} - \tilde{A}_E T_{11,E} - \tilde{C}_E \frac{1}{\beta} T_{12,E} &= 0 \ , \\
\tilde{A}_I T_{21,I} + \tilde{C}_I \frac{1}{\beta} T_{22,I} - \tilde{A}_E T_{21,E} - \tilde{C}_E \frac{1}{\beta} T_{22,E} &= \frac{\hat{T}_\theta}{4\pi\mu n(n+1)} \left[\frac{d}{d\theta} P_n^m(\cos\theta) \right]_{\theta=\theta_0} \ , \\
\tilde{B}_I T_{3,I} - \tilde{B}_E T_{3,E} &= \frac{-im\hat{T}_\theta}{2\pi\mu n(n+1) r_0^2} \left[\frac{P_n^m(\cos\theta_0)}{\sin\theta_0} \right] \ .
\end{aligned} \tag{A.24}$$

Assuming the same form of the solutions as in eqn. (A.20), and on carrying out the algebra, aided by the Wronskian relationship in eqn. (A.18), I obtain the potentials for the ring force pushing in the polar θ direction as

$$\begin{aligned}
\tilde{\phi}_I &= -\frac{i\alpha\hat{T}_\theta}{\pi r_0 \rho\omega^2} \left\{ \frac{1}{\beta^2 r_0} \left[\frac{d}{dr} h_n(\alpha r) \right]_{r=r_0} - \frac{1}{2} h_n(\alpha r_0) \right\} \left[\frac{d}{d\theta} P_n^m(\cos\theta) \right]_{\theta=\theta_0} j_n(\alpha r) \ , \\
\tilde{\phi}_E &= -\frac{i\alpha\hat{T}_\theta}{\pi r_0 \rho\omega^2} \left\{ \frac{1}{\beta^2 r_0} \left[\frac{d}{dr} j_n(\alpha r) \right]_{r=r_0} - \frac{1}{2} j_n(\alpha r_0) \right\} \left[\frac{d}{d\theta} P_n^m(\cos\theta) \right]_{\theta=\theta_0} h_n(\alpha r) \ , \\
\tilde{\psi}_I &= \frac{m\beta^3\hat{T}_\theta}{2\pi n(n+1)\rho\omega^2} h_n(\beta r_0) \left[\frac{P_n^m(\cos\theta_0)}{\sin\theta_0} \right] j_n(\beta r) \ , \\
\tilde{\psi}_E &= \frac{m\beta^3\hat{T}_\theta}{2\pi n(n+1)\rho\omega^2} j_n(\beta r_0) \left[\frac{P_n^m(\cos\theta_0)}{\sin\theta_0} \right] h_n(\beta r) \ , \\
\tilde{\chi}_I &= -\frac{i\beta^2\hat{T}_\theta}{\pi n(n+1)\rho\omega^2} \left\{ -\frac{1}{2} \left[\frac{d}{dr} h_n(\beta r) \right]_{r=r_0} + \frac{(n^2+n-\beta^2 r_0^2/2)}{\beta^2 r_0^3} h_n(\beta r_0) \right\} \times \\
&\qquad \times \left[\frac{d}{d\theta} P_n^m(\cos\theta) \right]_{\theta=\theta_0} j_n(\beta r) \ , \\
\tilde{\chi}_E &= -\frac{i\beta^2\hat{T}_\theta}{\pi n(n+1)\rho\omega^2} \left\{ -\frac{1}{2} \left[\frac{d}{dr} j_n(\beta r) \right]_{r=r_0} + \frac{(n^2+n-\beta^2 r_0^2/2)}{\beta^2 r_0^3} j_n(\beta r_0) \right\} \times \\
&\qquad \times \left[\frac{d}{d\theta} P_n^m(\cos\theta) \right]_{\theta=\theta_0} h_n(\beta r) \ .
\end{aligned} \tag{A.25}$$

A.3.3 Azimuthal (φ) direction

The ring traction load pushing in the positive φ direction is expressed as

$$\tau_\varphi^0(r_0,\theta,\varphi) = T_\varphi \frac{\delta(\theta-\theta_0)}{2\pi r_0^2 \sin\theta_0} \quad , \tag{A.26}$$

and the corresponding stress components in the transformed domain are given by

$$S^0 = -\frac{d}{d\varphi}\left(\tau_\varphi^0\right)\frac{1}{\sin\theta} = -\left[\frac{dT_\varphi}{d\varphi}\right]\frac{\delta(\theta-\theta_0)}{2\pi r_0^2\sin^2\theta} \quad ,$$

$$T^0 = \left[\frac{d}{d\theta}\left(\tau_\varphi^0 \sin\theta\right)\right]\frac{1}{\sin\theta} = T_\varphi \frac{\delta'(\theta-\theta_0)}{2\pi r_0^2 \sin\theta} \quad .$$

Expanding S^0 and T^0 in terms of SHW, I have

$$\begin{aligned} \tilde{S}^0 &= -\frac{im\hat{T}_\varphi}{2\pi r_0^2}\left[\frac{P_n^m(\cos\theta_0)}{\sin\theta_0}\right] \quad , \\ \tilde{T}^0 &= -\frac{\hat{T}_\varphi}{2\pi r_0^2}\left[\frac{d}{d\theta}P_n^m(\cos\theta)\right]_{\theta=\theta_0} \quad . \end{aligned} \tag{A.27}$$

Proceeding with the algebra in a manner similar to that in the previous section, I obtain the solutions for the potentials for a ring force in the azimuthal φ direction as

$$\begin{aligned} \tilde{\phi}_I &= -\frac{m\alpha\hat{T}_\varphi}{\pi r_0\rho\omega^2}\left\{\frac{1}{\beta^2 r_0}\left[\frac{d}{dr}h_n(\alpha r)\right]_{r=r_0} - \frac{1}{2}h_n(\alpha r_0)\right\}\left[\frac{P_n^m(\cos\theta)}{\sin\theta_0}\right] j_n(\alpha r) \quad , \\ \tilde{\phi}_E &= -\frac{m\alpha\hat{T}_\varphi}{\pi r_0\rho\omega^2}\left\{\frac{1}{\beta^2 r_0}\left[\frac{d}{dr}j_n(\alpha r)\right]_{r=r_0} - \frac{1}{2}j_n(\alpha r_0)\right\}\left[\frac{P_n^m(\cos\theta)}{\sin\theta_0}\right] h_n(\alpha r) \quad , \\ \tilde{\psi}_I &= -\frac{i\beta^3\hat{T}_\varphi}{2\pi n(n+1)\rho\omega^2}h_n(\beta r_0)\left[\frac{d}{d\theta}P_n^m(\cos\theta)\right]_{\theta=\theta_0} j_n(\beta r) \quad , \\ \tilde{\psi}_E &= -\frac{i\beta^3\hat{T}_\varphi}{2\pi n(n+1)\rho\omega^2}j_n(\beta r_0)\left[\frac{d}{d\theta}P_n^m(\cos\theta)\right]_{\theta=\theta_0} h_n(\beta r) \quad , \\ \tilde{\chi}_I &= \frac{m\beta^2\hat{T}_\varphi}{\pi n(n+1)\rho\omega^2}\left\{\frac{1}{2}\left[\frac{d}{dr}h_n(\beta r)\right]_{r=r_0} - \frac{(n^2+n-\beta^2 r_0^2/2)}{\beta^2 r_0^3}h_n(\beta r_0)\right\}\times \\ &\qquad \times\left[\frac{P_n^m(\cos\theta_0)}{\sin\theta_0}\right] j_n(\beta r) \quad , \end{aligned}$$

$$\tilde{\chi}_E = \frac{m\beta^2\hat{T}_\varphi}{\pi n(n+1)\rho\omega^2}\left\{\frac{1}{2}\left[\frac{d}{dr}j_n(\beta r)\right]_{r=r_0} - \frac{(n^2+n-\beta^2 r_0^2/2)}{\beta^2 r_0^3}j_n(\beta r_0)\right\}\times$$
$$\times\left[\frac{P_n^m(\cos\theta_0)}{\sin_{\theta_0}}\right]h_n(\beta r)\ . \qquad \text{(A.28)}$$

A.3.4 Ring Bending Moment

I apply a ring bending moment with a radial ring force couple with magnitude $M_b = F_r r\Delta\theta$, where $\Delta\theta$ is the vanishingly small angle in the polar direction as shown in Fig. A-2. The direction of the forces in the couple is chosen such that the couple applies

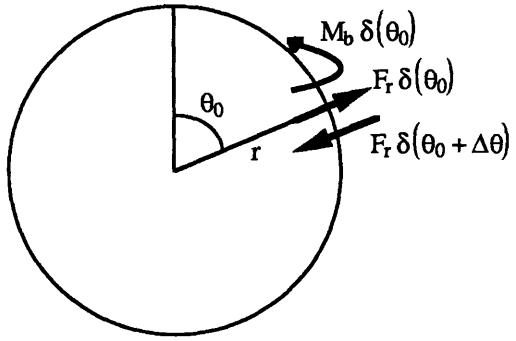

Figure A-2: Model for applying a ring bending moment along the positive φ direction on the sphere. We use a couple constituted of two radial ring forces located at (r,θ_0) and $(r,\theta_0+\Delta\theta)$.

a positive bending moment in the azimuthal (φ) direction. Then, the corresponding traction load which applies this bending moment is given by

$$F_r = M_b\left[\frac{-\delta(\theta_0+\Delta\theta)+\delta(\theta_0)}{r\Delta\theta}\right] = -M_b\frac{\delta'(\theta-\theta_0)}{r}\ .$$

I represent the ring traction load in the radial direction due to the bending moment as

$$\bar{\tau}_r^0(r_0,\theta,\varphi) = -M_b\frac{\delta'(\theta-\theta_0)}{2\pi r_0^3\sin\theta}\ , \qquad \text{(A.29)}$$

and correspondingly

$$\tilde{\bar{\tau}}_r^0 = \hat{M}_b \frac{1}{2\pi r_0^3} \left[\frac{d}{d\theta} P_n^m(\cos\theta) \right]_{\theta=\theta_0} \quad .$$

Then, using my results for the radial ring traction, we can easily show that the potentials for a ring bending moment take the form

$$\begin{aligned}
\tilde{\phi}_I &= \frac{i\alpha \hat{M}_b}{2\pi r_0 \rho \omega^2} \left[\frac{d}{dr} h_n(\alpha r) \right]_{r=r_0} \left[\frac{d}{d\theta} P_n^m(\cos\theta) \right]_{\theta=\theta_0} j_n(\alpha r) \quad , \\
\tilde{\phi}_E &= \frac{i\alpha \hat{M}_b}{2\pi r_0 \rho \omega^2} \left[\frac{d}{dr} j_n(\alpha r) \right]_{r=r_0} \left[\frac{d}{d\theta} P_n^m(\cos\theta) \right]_{\theta=\theta_0} h_n(\alpha r) \quad , \\
\tilde{\psi}_I &= 0 \quad , \\
\tilde{\psi}_E &= 0 \quad , \\
\tilde{\chi}_I &= \frac{i\beta^2 \hat{M}_b}{2\pi r_0^2 \rho \omega^2} h_n(\beta r_0) \left[\frac{d}{d\theta} P_n^m(\cos\theta) \right]_{\theta=\theta_0} j_n(\beta r) \quad , \\
\tilde{\chi}_E &= \frac{i\beta^2 \hat{M}_b}{2\pi r_0^2 \rho \omega^2} j_n(\beta r_0) \left[\frac{d}{d\theta} P_n^m(\cos\theta) \right]_{\theta=\theta_0} h_n(\beta r) \quad . \qquad \text{(A.30)}
\end{aligned}$$

A.4 Summary

In this Appendix, I derived explicit analytical solutions for Green's functions for ring traction loads in a solid unbounded elastic medium using spherical coordinates. Solutions were obtained for ring forces pushing in the radial, polar and azimuthal directions, and for a ring bending moment acting along the positive azimuthal (φ) coordinate. As an aside, it is worthwhile to note that similar expressions were obtained by Ricks [60] who derived the Green's functions for ring tractions in cylindrical coordinates. For non-axisymmetric loadings, I employed a linear transformation of the tangential components of stresses and displacements to satisfy the boundary conditions. This facilitated the derivation of closed form solutions for the interior and exterior potentials. Having obtained the solutions due to ring traction excitations, the Green's functions for excitation by a point source in any arbitrary direction in an unbounded medium may be readily synthesized. As pointed out in the Introduction, these explicit solutions are required to model the scattering of sound from coupled

structures. In Chapter 2, I draw upon my analyses here, where I model the acoustic scattering from a spherical protuberance on an infinite submerged plate.

Appendix B

Influence Matrices for sphere and plate

B.1 Overview

In this Appendix, I present the details and the significant results of the decoupled constituent problems from my coupling formulation in Chapter 2. I begin by computing the free sphere displacement components and the scattered pressure from the free sphere in Section B.2. Section B.3 contains the analysis of the influence coefficients for the thin elastic plate, while Section B.4 contains the influence coefficients for the elastic sphere excited by ring forces and bending moment.

B.2 The free submerged elastic sphere

As stated in subsection 2.4.1, I need to satisfy four boundary conditions at the fluid-elastic interface. The expressions for the transformed components of displacements and stresses were given in Appendix A. The boundary conditions are

- Continuity of radial or normal displacement, $U_i + U_s = U_r$, or

$$-A_{mn}\Pi_{11} + B_{mn}\Pi_{12} + D_{mn}\Pi_{13} = \delta_1 \quad , \tag{B.1}$$

- Continuity of normal stress (pressure), $R_i + R_s = R_r$, or

$$-A_{mn}\Pi_{21} + B_{mn}\Pi_{22} + D_{mn}\Pi_{23} = \delta_2 \quad , \tag{B.2}$$

- Vanishing of the transformed tangential shear stress, $S_r = 0$, or

$$B_{mn}\Pi_{32} + D_{mn}\Pi_{33} = 0 \quad , \tag{B.3}$$

- Vanishing of the transformed tangential shear stress, $T_r = 0$, or

$$C_{mn} = 0 \quad . \tag{B.4}$$

Expressing these boundary conditions in matrix form, the amplitudes of the potentials for excitation by the incident acoustic field for the the free submerged sphere are given by

$$A_{mn} = \frac{\Theta_1}{\Delta_0} \; , \; B_{mn} = \frac{\Theta_2}{\Delta_0} \; , \; C_{mn} = 0 \; , \; D_{mn} = \frac{\Theta_3}{\Delta_0} \quad , \tag{B.5}$$

where

$$\begin{aligned}
\Delta_0 &= \Pi_{11}\Pi_{22}\Pi_{33} - \Pi_{11}\Pi_{32}\Pi_{23} + \Pi_{21}\Pi_{32}\Pi_{13} - \Pi_{21}\Pi_{12}\Pi_{33} \quad , \\
\Theta_1 &= \delta_1\Pi_{22}\Pi_{33} - \delta_1\Pi_{32}\Pi_{23} + \delta_2\Pi_{32}\Pi_{13} - \delta_2\Pi_{12}\Pi_{33} \quad , \\
\Theta_2 &= \delta_2\Pi_{11}\Pi_{33} - \delta_1\Pi_{21}\Pi_{33} \quad , \\
\Theta_3 &= -\delta_2\Pi_{11}\Pi_{32} + \delta_1\Pi_{21}\Pi_{32} \quad .
\end{aligned}$$

Also,

$$\Pi_{11} = -h_n'(\alpha_0 a) \quad , \quad \Pi_{12} = j_n'(\alpha_1 a) \quad ,$$

$$
\begin{aligned}
\Pi_{13} &= \frac{n(n+1)}{\beta_1 a} j_n(\beta_1 a) \ , \ \Pi_{21} = \frac{\lambda_0}{2}\alpha_0^2 a h_n(\alpha_0 a) \ , \\
\Pi_{22} &= \mu_1 \left[\chi j_n(\alpha_1 a) + 2\alpha_1 j_{n+1}(\alpha_1 a)\right] \ , \\
\Pi_{23} &= \mu_1 \frac{n(n+1)}{\beta_1} \left[a j_n'(\beta_1 a) - j_n(\beta_1 a)\right] \ , \\
\Pi_{31} &= 0 \ , \ \Pi_{32} = \mu_1 \left[j_n'(\alpha_1 a) - \frac{1}{a} j_n(\alpha_1 a)\right] \ , \\
\Pi_{33} &= \frac{\mu_1}{\beta_1} \left[\chi j_n(\beta_1 a) + \beta_1 j_{n+1}(\beta_1 a)\right] \ , \\
\delta_1 &= j_n'(\alpha_0 a) \ , \ \delta_2 = -\frac{\lambda_0}{2}\alpha_0^2 a j_n(\alpha_0 a) \ , \ \delta_3 = 0 \ ,
\end{aligned} \tag{B.6}
$$

where $\chi = (n^2 - n - \frac{1}{2}\beta_1^2 a^2)/a$, and I have used the concise notation

$$
z_n'(ka) = \left[\frac{d}{dr} z_n(kr)\right]_{r=a} = \frac{n}{a} z_n(ka) - k z_{n+1}(ka)
$$

($z = j, h$). Setting $\Delta_0 = 0$ at each polar order n yields the resonances of the solid sphere immersed in fluid.

B.3 The thin elastic plate

B.3.1 In-plane Motions

As discussed in Section 2.4.2, the boundary conditions that need to be satisfied at the inner annulus of the plate for in-plane motions are

$$
\begin{aligned}
-\frac{f_R}{2\pi b h} &= (\lambda_2 + 2\mu_2)\frac{\partial v_R}{\partial R} + \frac{\lambda_2}{R}\left[v_R + \frac{\partial v_\varphi}{\partial \varphi}\right] \ , \\
-\frac{f_\varphi}{2\pi b h} &= \mu_2 \left[\frac{\partial v_\varphi}{\partial R} - \frac{v_\varphi}{R} + \frac{1}{R}\frac{\partial v_R}{\partial \varphi}\right] \ .
\end{aligned} \tag{B.7}
$$

Substituting for v_R and v_φ from eqns. (2.21) and (2.22)

$$
\begin{aligned}
-\frac{f_R}{2\pi b h} &= \lambda_2 \nabla^2 \Gamma + 2\mu_2 \left[\frac{\partial^2 \Gamma}{\partial R^2} + \frac{\partial}{\partial R}\left(\frac{1}{R}\frac{\partial \Omega}{\partial \varphi}\right)\right] \ , \\
-\frac{f_\varphi}{2\pi b h} &= \mu_2 \left[2\left(\frac{1}{R}\frac{\partial^2 \Gamma}{\partial \varphi \partial R} - \frac{1}{R^2}\frac{\partial \Gamma}{\partial \varphi}\right) + \left(\frac{1}{R^2}\frac{\partial^2 \Omega}{\partial \varphi^2} - R\frac{\partial}{\partial R}\left(\frac{1}{R}\frac{\partial \Omega}{\partial R}\right)\right)\right] \ .
\end{aligned}
$$

Taking the Fourier transform, i.e. setting $\partial/\partial\varphi \to im$, dividing both sides by $2\mu_2$, and using $\lambda/2\mu_2 = (\eta^2/2\kappa^2 - 1)$, we obtain

$$\begin{aligned} -\frac{\hat{f}_R}{4\pi\mu_2 bh} &= \left[(\kappa^2 - \frac{\eta^2}{2})\hat{\Gamma} + \frac{\partial^2\hat{\Gamma}}{\partial R^2}\right] + \frac{im}{R}\left[\frac{\partial\hat{\Omega}}{\partial R} - \frac{\hat{\Omega}}{R}\right]\Big|_{R=b} \quad , \\ -\frac{\hat{f}_\varphi}{4\pi\mu_2 bh} &= \frac{im}{R}\left[\frac{\partial\hat{\Gamma}}{\partial R} - \frac{\hat{\Gamma}}{R}\right] - \frac{1}{2}\left[\frac{\partial^2\hat{\Omega}}{\partial R^2} - \frac{1}{R}\frac{\partial\hat{\Omega}}{\partial R} + \frac{m^2}{R^2}\hat{\Omega}\right]\Big|_{R=b} \quad . \end{aligned} \tag{B.8}$$

Finally, the entries $\hat{P}_{ij}$ $(i,j = 1,2)$ of the plate influence matrix for the in-plane motion are given by

$$\begin{aligned} \hat{P}_{11} &= M_1\left\{G_{22}H'_m(\kappa b) - G_{21}\frac{im}{b}H_m(\eta b)\right\} \quad , \\ \hat{P}_{12} &= M_1\left\{-G_{12}H'_m(\kappa b) + G_{11}\frac{im}{b}H_m(\eta b)\right\} \quad , \\ \hat{P}_{21} &= M_1\left\{G_{22}\frac{im}{b}H_m(\kappa b) + G_{21}H'_m(\eta b)\right\} \quad , \\ \hat{P}_{22} &= M_1\left\{-G_{12}\frac{im}{b}H_m(\kappa b) - G_{11}H'_m(\eta b)\right\} \quad , \end{aligned} \tag{B.9}$$

where

$$\begin{aligned} G_{11} &= \frac{1}{b}\left[\frac{(m^2 - \eta^2 b^2/2)}{b}H_m(\kappa b) - H'_m(\kappa b)\right] \quad , \\ G_{12} &= \frac{im}{b}\left[H'_m(\eta b) - \frac{1}{b}H_m(\eta b)\right] \quad , \\ G_{21} &= \frac{im}{b}\left[H'_m(\kappa b) - \frac{1}{b}H_m(\kappa b)\right] \quad , \\ G_{22} &= -\frac{1}{b}\left[\frac{(m^2 - \eta^2 b^2/2)}{b}H_m(\eta b) - H'_m(\eta b)\right] \quad , \end{aligned} \tag{B.10}$$

and

$$M_1 = -\frac{1}{4\pi\mu_1 bh\Delta_1} \quad , \quad \Delta_1 = G_{11}G_{22} - G_{12}G_{21} \quad . \tag{B.11}$$

B.3.2 Out-of-plane Motions

As discussed in Section 2.4.3, the boundary conditions that need to be satisfied at the inner annulus of the plate for the out-of-plane motions are

$$\begin{aligned} -\frac{M_b}{2\pi b} &= -D\left[\frac{\partial^2 w}{\partial R^2}+\nu\left(\frac{1}{R}\frac{\partial w}{\partial R}+\frac{1}{R^2}\frac{\partial^2 w}{\partial \varphi^2}\right)\right]_{R=b} , \\ -\frac{f_z}{2\pi b} &= -D\left[\frac{\partial(\nabla^2 w)}{\partial R}+\frac{(1-\nu)}{R^2}\frac{\partial^2}{\partial \varphi^2}\left(\frac{\partial w}{\partial R}-\frac{w}{R}\right)\right]_{R=b} . \end{aligned} \tag{B.12}$$

Note that M_b and f_z are total bending moment and shear force respectively. I use a mathematical trick to simplify the first term of eqn. B.12. Factoring the biharmonic equation as, we have

$$(\nabla^2+\xi_f^2)(\nabla^2-\xi_f^2)=0 \quad ,$$

with the solution to the first and second components being given by $H_m(\xi_f R)$ and $K_m(\xi_f R)$ respectively. In other words,

$$\nabla^2 w = \begin{cases} -\xi_f^2 w & \text{for } w = H_m(\xi_f R) \\ +\xi_f^2 w & \text{for } w = K_m(\xi_f R) \end{cases} .$$

Taking the Fourier transform on both sides of eqn. (B.12) wrt φ, and replacing $\partial/\partial\varphi$ with im, we get

$$\begin{aligned} \frac{\hat{M}_b}{2\pi b D} &= \frac{\partial^2 \hat{w}}{\partial R^2}+\frac{\nu(im)^2}{R^2}\hat{w}+\frac{\nu}{R}\frac{\partial \hat{w}}{\partial R}\bigg|_{R=b} , \\ \frac{\hat{f}_z}{2\pi b D} &= \mp\xi_f^2\frac{\partial \hat{w}}{\partial R}+\frac{(1-\nu)(im)^2}{R^2}\left(\frac{\partial \hat{w}}{\partial R}-\frac{\hat{w}}{R}\right)\bigg|_{R=b} , \end{aligned} \tag{B.13}$$

where I have used the compact notation $\mp$ to represent the use of $(-)$ for $w = H_m(\xi_f R)$ and $(+)$ for $w = K_m(\xi_f R)$. This set of equations can then be solved for the constants $\hat{C}_3$ and $\hat{C}_4$, and finally the entries $\hat{P}_{ij}$ $(i,j = 3,4)$ of the plate influence matrix for the out-of-plane motion are obtained as

$$\hat{P}_{33} = M_2\left\{O_{22}H_m(\xi_f b)-O_{21}K_m(\xi_f b)\right\} ,$$

$$
\begin{aligned}
\hat{P}_{34} &= M_2\left\{-O_{12}H_m(\xi_f b)+O_{11}K_m(\xi_f b)\right\} \ , \\
\hat{P}_{43} &= M_2\left\{O_{22}H'_m(\xi_f b)-O_{21}K'_m(\xi_f b)\right\} \ , \\
\hat{P}_{44} &= M_2\left\{-O_{12}H'_m(\xi_f b)+O_{11}K'_m(\xi_f b)\right\} \ ,
\end{aligned} \tag{B.14}
$$

where

$$
\begin{aligned}
O_{11} &= -\left[\frac{(1-\nu)m^2}{b^2}+\xi_f^2\right]H'_m(\xi_f b)+\frac{(1-\nu)m^2}{b^3}H_m(\xi_f b) \ , \\
O_{12} &= -\left[\frac{(1-\nu)m^2}{b^2}-\xi_f^2\right]K'_m(\xi_f b)+\frac{(1-\nu)m^2}{b^3}K_m(\xi_f b) \ , \\
O_{21} &= \left[\frac{(1-\nu)m^2}{b^2}-\xi_f^2\right]H_m(\xi_f b)-\frac{(1-\nu)}{b}H'_m(\xi_f b) \ , \\
O_{22} &= \left[\frac{(1-\nu)m^2}{b^2}+\xi_f^2\right]K_m(\xi_f b)-\frac{(1-\nu)}{b}K'_m(\xi_f b) \ ,
\end{aligned} \tag{B.15}
$$

and

$$
M_2=\frac{1}{2\pi b D\Delta_2} \ , \quad \Delta_2=O_{11}O_{22}-O_{12}O_{21} \ .
$$

I have used the concise notation $(Z=H,K)$

$$
Z'_m(kb)=\left[\frac{d}{dR}Z_m(kR)\right]_{R=b}=\frac{m}{b}Z_m(kb)-kZ_{m+1}(kb) \ .
$$

B.4 The submerged elastic sphere excited by coupling forces

The entries $\tilde{S}_{ij}$ (i,j $=1,\ldots,4$) of the sphere influence matrix are found by proceeding in a manner similar to that of the free submerged by replacing $(A_{mn},B_{mn},C_{mn},D_{mn})$ with $(I_{mn},J_{mn},K_{mn},L_{mn})$, respectively.

B.4.1 Radial (r) Ring Traction

The ring traction load load in the radial direction is expressed as

$$\tau_r^0(a,\theta,\varphi) = f_r(\varphi)\frac{\delta(\theta-\gamma)}{2\pi a^2 \sin\theta} \ ,$$

and its expansion in terms of Spherical Harmonic Waves is given by

$$\begin{aligned} \tilde{\tau}_r^0(a,m,n) \equiv R^0 &= \int_{-\pi}^{\pi} e^{-im\varphi} d\varphi \int_0^{\pi} f_r(\varphi)\frac{\delta(\theta-\gamma)}{2\pi a^2 \sin\theta} P_n^m(\cos\theta)\sin\theta d\theta \\ &= \frac{\hat{f}_r}{2\pi a^2} P_n^m(\cos\gamma) \ , \end{aligned}$$

where the 'tilde' notation is used to denote dependence on both the polar order n and the azimuthal order m, and the 'hat' denotes dependence on the Fourier or azimuthal order order m only. Balancing tractions, and referring to the quantities defined in eqn. (B.6), the potentials for the ring force acting in the radial (r) direction are given by

$$\begin{aligned} I_{mn} &= \frac{\hat{f}_r}{4\pi} P_n^m(\cos\gamma)\left[\frac{\Pi_{32}\Pi_{13} - \Pi_{12}\Pi_{33}}{\Delta_0}\right] \ , \\ J_{mn} &= \frac{\hat{f}_r}{4\pi} P_n^m(\cos\gamma)\left[\frac{\Pi_{11}\Pi_{33}}{\Delta_0}\right] \ , \\ K_{mn} &= 0 \ , \\ L_{mn} &= -\frac{\hat{f}_r}{4\pi} P_n^m(\cos\gamma)\left[\frac{\Pi_{11}\Pi_{32}}{\Delta_0}\right] \ . \end{aligned} \tag{B.16}$$

B.4.2 Polar (θ) Ring Traction

The ring traction load load in the polar (θ) direction is expressed as

$$\tau_\theta^0(a,\theta,\varphi) = f_\theta(\varphi)\frac{\delta(\theta-\gamma)}{2\pi a^2 \sin\theta} \ .$$

Transforming this component of stress, we obtain the corresponding stress components S^0 and T^0 as

$$\begin{aligned} S^0 &= -\left[\frac{\partial}{\partial\theta}(\tau_\theta^0)\sin\theta\right]\frac{1}{\sin\theta} = -f_\theta(\varphi)\frac{\delta'(\theta-\gamma)}{2\pi a^2\sin\theta} \quad , \\ T^0 &= -\left[\frac{\partial}{\partial\varphi}(\tau_\theta^0)\right]\frac{1}{\sin\theta} = -\left[\frac{df_\theta(\varphi)}{d\varphi}\right]\frac{\delta(\theta-\gamma)}{2\pi a^2\sin\theta} \quad . \end{aligned}$$

The expansion of these transformed stress components in terms of SHW may then be shown to be given by

$$\hat{S}^0 = \frac{\hat{f}_\theta}{2\pi a^2}\left[\frac{d}{d\theta}P_n^m(\cos\theta)\right]_{\theta=\gamma} \quad , \quad \hat{T}^0 = -\frac{im\hat{f}_\theta}{2\pi a^2\sin\gamma}P_n^m(\cos\gamma) \quad .$$

Balancing tractions in a manner similar to the radial traction, the potentials for the ring force acting in the polar (θ) direction, are found to be

$$\begin{aligned} I_{mn} &= \frac{\hat{f}_\theta}{4\pi n(n+1)}\left[\frac{d}{d\theta}P_n^m(\cos\theta)\right]_{\theta=\gamma}\left[\frac{\Pi_{12}\Pi_{23}-\Pi_{13}\Pi_{22}}{\Delta_0}\right] \quad , \\ J_{mn} &= \frac{\hat{f}_\theta}{4\pi n(n+1)}\left[\frac{d}{d\theta}P_n^m(\cos\theta)\right]_{\theta=\gamma}\left[\frac{\Pi_{21}\Pi_{13}-\Pi_{11}\Pi_{23}}{\Delta_0}\right] \quad , \\ K_{mn} &= -\frac{im\hat{f}_\theta}{2\pi\mu an(n+1)}\left[\frac{P_n^m(\cos\gamma)}{\sin\gamma}\right]\left[\frac{1}{aj_n'(\beta_1 a)-j_n(\beta_1 a)}\right] \quad , \\ L_{mn} &= \frac{\hat{f}_\theta}{4\pi n(n+1)}\left[\frac{d}{d\theta}P_n^m(\cos\theta)\right]_{\theta=\gamma}\left[\frac{\Pi_{11}\Pi_{22}-\Pi_{21}\Pi_{12}}{\Delta_0}\right] \quad . \end{aligned} \tag{B.17}$$

B.4.3 Azimuthal (φ) Ring Traction

The ring traction load load in the azimuthal (φ) direction is expressed as

$$\tau_\varphi^0(a,\theta,\varphi) = f_\varphi(\varphi)\frac{\delta(\theta-\gamma)}{2\pi a^2\sin\theta} \quad .$$

Transforming this tangential stress into the two components S^0 and T^0, and then expanding these in terms of SHW, we obtain

$$\hat{S}^0 = -\frac{im\hat{f}_\varphi}{2\pi a^2 \sin\gamma} P_n^m(\cos\gamma) \ , \ \hat{T}^0 = -\frac{\hat{f}_\varphi}{2\pi a^2}\left[\frac{d}{d\theta}P_n^m(\cos\theta)\right]_{\theta=\gamma} \ .$$

Balancing tractions yields the following expressions for the potentials for the ring force acting in the azimuthal (φ) direction

$$\begin{aligned}
I_{mn} &= -\frac{im\hat{f}_\varphi}{4\pi n(n+1)}\left[\frac{P_n^m(\cos\gamma)}{\sin\gamma}\right]\left[\frac{\Pi_{12}\Pi_{23}-\Pi_{13}\Pi_{22}}{\Delta_0}\right] \ , \\
J_{mn} &= -\frac{im\hat{f}_\varphi}{4\pi n(n+1)}\left[\frac{P_n^m(\cos\gamma)}{\sin\gamma}\right]\left[\frac{\Pi_{21}\Pi_{13}-\Pi_{11}\Pi_{23}}{\Delta_0}\right] \ , \\
K_{mn} &= -\frac{\hat{f}_\varphi}{2\pi\mu a n(n+1)}\left[\frac{dP_n^m(\cos\theta)}{d\theta}\right]_{\theta=\gamma}\left[\frac{1}{aj_n'(\beta_1 a)-j_n(\beta_1 a)}\right] \ , \\
L_{mn} &= -\frac{im\hat{f}_\varphi}{4\pi n(n+1)}\left[\frac{P_n^m(\cos\gamma)}{\sin\gamma}\right]\left[\frac{\Pi_{11}\Pi_{22}-\Pi_{21}\Pi_{12}}{\Delta_0}\right] \ . \qquad \text{(B.18)}
\end{aligned}$$

B.4.4 Ring Bending Moment

As shown in Appendix A, I apply a ring bending moment via a force couple, and represent the ring traction load in the radial direction due to the bending moment as

$$\bar{\tau}_r^0(a,\theta,\varphi) = -M_b(\varphi)\frac{\delta'(\theta-\gamma)}{2\pi a^3 \sin\theta} \ ,$$

and correspondingly, its expansion in terms of SHW is obtained as

$$\tilde{\bar{\tau}}_r^0(a,m,n) = \frac{\hat{M}_b}{2\pi a^3}\left[\frac{d}{d\theta}P_n^m(\cos\theta)\right]_{\theta=\gamma} \ .$$

Finally, the solutions for the ring bending moment are found to be

$$\begin{aligned}
I_{mn} &= \frac{\hat{M}_b}{4\pi a}\left[\frac{d}{d\theta}P_n^m(\cos\gamma)\right]_{\theta=\gamma}\left[\frac{\Pi_{32}\Pi_{13}-\Pi_{12}\Pi_{33}}{\Delta_0}\right] \ , \\
J_{mn} &= \frac{\hat{M}_b}{4\pi a}\left[\frac{d}{d\theta}P_n^m(\cos\gamma)\right]_{\theta=\gamma}\left[\frac{\Pi_{11}\Pi_{33}}{\Delta_0}\right] \ ,
\end{aligned}$$

$$
\begin{aligned}
K_{mn} &= 0 \ , \\
L_{mn} &= -\frac{\hat{M}_b}{4\pi a}\left[\frac{d}{d\theta}P_n^m(\cos\gamma)\right]_{\theta=\gamma}\left[\frac{\Pi_{11}\Pi_{32}}{\Delta_0}\right] \ . \qquad \text{(B.19)}
\end{aligned}
$$

Appendix C

Horizontal and Vertical Array Sensor Positions

In this Appendix, I list the sensor positions for the three arrays used in my analysis. The positions for horizontal array sensors are essentially the same as those given in Ref. [42]. The arrival times of the direct pulse demonstrated the consistency of these positions. The sensor positions for 16 channels of the long vertical array and the fixation points of the shorter arrays were provided by Tom Hayward of NRL [44]. These were given with respect to a coordinate system aligned with the N-E axis of the horizontal array, and had to be transformed to the universal coordinate system. The missing positions were interpolated using the analysis in Section 3.3.2. That analysis methodolgy was also extended to estimate the sensor positions of the shorter vertical arrays. Moreover, by repeated iteration I improved on the estimates of the shorter array positions by comparing the nearfield beamforming results obtained by independent processing of the horizontal and short vertical array reverberation data.

HORIZONTAL ARRAY POSITIONS			
Hydrophone #	$X_s(m)$	$Y_s(m)$	$Z_s(m)$
1	14.0834	17.537	60.0
2	51.0266	62.375	60.0
3	-34.8596	30.741	60.0
4	23.3318	-9.845	60.0
5	0.0	0.0	60.0
6	28.6041	30.965	60.0
7	-21.6686	12.825	60.0
8	-10.28	-13.397	60.0
9	-27.8904	-34.931	60.0
10	37.2584	-29.693	60.0
11	64.7682	-50.206	60.0
12	129.213	-99.734	60.0
13	-59.3577	55.013	60.0
14	-49.2728	-62.052	60.0
15	103.035	121.974	60.0
16	-96.0213	-122.533	60.0
17	-117.35	99.552	60.0
18	-272.318	222.216	60.0
19	170.479	197.15	60.0
20	-187.487	-289.897	60.0
21	263.392	-211.6	60.0
22	547.593	-432.586	60.0
23	-372.394	-568.349	60.0
24	-499.854	415.074	60.0
25	402.652	489.644	60.0

Table C.1: Horizontal array hydrophone positions

LONG VERTICAL ARRAY POSITIONS			
Hydrophone #	$X_s(m)$	$Y_s(m)$	$Z_s(m)$
1	-58.162	-4.860	27.702
2	-50.728	3.491	55.454
3	-43.353	1.174	83.259
4	-36.073	19.905	111.115
5	-28.911	28.005	139.024
6	-21.881	36.046	166.988
7	-14.991	44.027	195.006
8	-8.242	51.944	223.079
9	-2.730	58.474	252.562
10	4.131	66.563	280.625
11	10.866	74.733	308.694
12	17.442	82.971	336.781
13	23.714	90.633	365.100
14	30.066	98.225	393.420
15	36.536	105.718	421.739
16	42.887	113.312	450.059
17	47.086	118.517	478.368
18	52.731	125.178	507.040
19	58.277	131.658	535.774
20	63.720	137.953	564.573
21	69.050	144.058	593.437
22	79.329	155.691	651.360
23	89.011	166.547	709.545
24	97.977	176.616	767.992
25	106.566	186.718	827.995
26	113.368	194.348	887.118
27	119.312	201.452	946.399
28	124.177	207.653	1005.879
29	128.301	213.263	1065.473
30	131.454	217.845	1125.215
31	132.924	220.064	1185.156

Table C.2: Long vertical line array hydrophone positions

SHORT VERTICAL ARRAY POSITIONS			
Hydrophone #	$X_s(m)$	$Y_s(m)$	$Z_s(m)$
1	-88.337	10.041	29.602
2	-82.646	16.486	88.979
3	-80.191	19.265	118.749
4	-78.014	21.730	148.567
5	-76.126	23.868	178.431
6	-74.542	25.661	208.335
7	-72.343	28.151	268.240
8	-71.539	29.062	328.225
9	-109.527	31.227	29.602
10	-103.836	37.671	88.979
11	-101.381	40.451	118.749
12	-99.204	42.916	148.749
13	-97.316	45.052	178.431
14	-95.732	46.847	208.335
15	-93.533	49.339	268.240
16	-92.729	50.248	328.225
17	-139.652	44.148	29.602
18	-133.961	50.591	88.979
19	-131.506	53.371	118.749
20	-129.329	55.836	148.749
21	-127.441	57.974	178.431
22	-125.858	59.767	208.335
23	-123.658	62.257	268.240
24	-122.854	63.168	328.225
25	-204.606	105.000	29.602
26	-198.914	111.445	88.979
27	-196.460	114.224	118.749
28	-194.282	116.689	148.749
29	-192.394	118.826	178.431
30	-190.811	120.620	208.335
31	-188.612	123.110	268.240
32	-187.807	124.021	328.225

Table C.3: Estimated short vertical line arrays hydrophone positions

Bibliography

[1] P. Mikhalevsky, "Feasibility of acoustic thermometry of Arctic Ocean climate change", *J. Acoust. Soc. America*, **94**, 1760 (A), 1993.

[2] H. Schmidt and B. Tracey, "Trans-Arctic effects of changes in ice morphology", *J. Acoust. Soc. America*, **96**, 3353 (A), 1994.

[3] J. A. Ogilvy, "Wave scattering from rough surfaces", *Rep. Prog. Phys.*, **50**, 1553 - 1608, 1987.

[4] W. A. Kuperman and H. Schmidt, "Rough surface elastic wave scattering in a horizontally stratified ocean", *J. Acoust. Soc. America*, **79**(6), 1767 - 1777, 1986.

[5] W. A. Kuperman and H. Schmidt, "Self-consistent perturbation approach to rough surface scattering in stratified elastic media", *J. Acoust. Soc. America*, **86**(4), 1511 - 1522, 1989.

[6] L. M. Brekovskikh and Y. P. Lysanov, *Fundamentals of Ocean Acoustics*, Springer Verlag, pp 182 - 215, 1990.

[7] Kevin D. LePage, "Elastic scattering in oceanic waveguides" Ph.D. thesis, MIT, May 1992.

[8] V. Twersky, "On scattering and reflection of sound by rough surfaces", *J. Acoust. Soc. America*, **29**, 209 - 255, October 1957.

[9] J. E. Burke and V. Twersky, "On scattering and reflection by elliptically straited surfaces", *J. Acoust. Soc. America*, **40**(4), 883 - 895, 1966.

[10] D. Chu and T. K. Stanton, "Application of Twersky's boss scattering theory to laboratory measurements of sound scattered by a rough surface", *J. Acoust. Soc. America*, **87**(4), 1557 - 1568, 1990.

[11] P. Gerstoft and H. Schmidt, "A boundary element approach to ocean seismoacoustic facet reverberation", *J. Acoust. Soc. America*, **89**(4), 1629 - 1642, 1991.

[12] J. R. Fricke, "Quasi-linear elastodynamic equations for finite difference solutions in discontinuous media", *J. Comp. Acoust.*, **1**(3), 303 - 320, 1993.

[13] J. R. Fricke, "Acoustic scattering from elemental Arctic ice features: Numerical modeling results", *J. Acoust. Soc. America*, **93**(4), 1784 - 1796, 1993.

[14] D. R. Burns and R. A. Stephens, "Three-dimensional modeling of geoacoustic scattering from seafloor topography", *J. Acoust. Soc. America*, **88**(5), 2338 - 2345, 1990.

[15] T. W. Dawson, "Acoustic scattering in a three-dimensional oceanic waveguide using boundary integral equation methods", *J. Acoust. Soc. America*, **90**(5), 2609 - 2622, 1991.

[16] L. M. Lyamshev, "Reflection of Sound from a moving thin plate", *Sov. Phys. Acoust*, **6**(2), 505 - 507, 1961.

[17] L. M. Brekhovskikh, *Waves in layered media*, Second edition, Academic Press, pp 76 - 80, 1980.

[18] A. J. Langley, "The sound fields of an infinite, fluid-loaded plate excited by a point force", *J. Acoust. Soc. America*, **83**(4), 1360 - 1365, 1988.

[19] D. G. Crighton, "The 1988 Rayleigh Medal Lecture : fluid loading - the interaction between sound and vibration", *J. Sound and Vibration*, **133**(1), 1 - 27, 1989.

[20] Miguel C. Junger and David Feit, *Sound, Structures, and their interaction*, Published by the Acous. Soc. Am. through the Am. Inst. Phy., pp 237 - 239, 1993.

[21] G. Maidanik, A. J. Tucker and W. H. Vogel, "Transmission of free waves across a rib on a panel", *J. Sound and Vibration*, **49**, 445 - 452, 1976.

[22] D. G. Crighton and G. Maidanik, "Acoustic and vibration fields generated by ribs on a fluid-loaded panel, I: Plane-wave problems for a single rib", *J. Sound and Vibration*, **75**, 437 - 452, 1981.

[23] Y. P. Guo, "Effects of structural joints on sound scattering", *J. Acoust. Soc. America*, **93**(2), 857 - 863, 1993.

[24] J. R. Fricke and G. L. Unger, "Acoustic scattering from elemental Arctic ice features: Experimental results", *J. Acoust. Soc America*, **97**(1), 192 - 198, 1995.

[25] T. Kapoor and L. B. Felsen, "Hybrid ray-mode analysis of scattering from a finite, fluid-loaded plate", To be published in *Wave Motion*, June 1995.

[26] Y. P. Guo, "Sound scattering by bulkheads in cylindrical shells", *J. Acoust. Soc. America*, **95**(5), 2550 - 2559, 1993.

[27] Y. P. Guo, "Sound scattering from cylindrical shells with internal elastic plates", *J. Acoust. Soc. America*, **93**(3), 1936 - 1946, 1992.

[28] J. D. Achenbach, J. Bjarnason and T. Igusa "Effect of vibrating sub-structure on acoustic radiation from a cylindrical shell", *Journal of Vibration and Acoustics*, 1990.

[29] Philip M. Morse and K. Uno Ingard, *Theoretical Acoustics*, Princeton University Press, pp 418 - 440, 1986.

[30] James J. Faran, Jr "Sound scattering by solid cylinders and spheres", *J. Acoust. Soc. America*, **23**(4), 405 - 418, 1951.

[31] Robert Hickling, "Analysis of echoes from a solid elastic sphere in water", *J. Acoust. Soc. America*, **34**(10), 1582 - 1591, 1962.

[32] Yih-Hsing Pao and C. C. Mow, "Scattering of plane compressional waves by a spherical obstacle", *J. Appl. Phys.*, **34**(3), 493 - 499, 1963.

[33] H. Schmidt, "Numerically stable global matrix approach to radiation and scattering from spherically stratified shells", *J. Acoust. Soc. America*, **94**(4), 2420 - 2430, 1993.

[34] Philip M. Morse and Herman Feshbach, *Methods of Theoretical Physics*, McGraw-hill Book Company, Inc., (i) pp 1762 - 1766, (ii) 1462 - 1466, 1953.

[35] H. Schmidt. *SAFARI : User's Guide*, SR 113, SACLANT ASW Research Center, La Spezia, Italy, 1987.

[36] Karl. F. Graff, *Wave Motion in Elastic Solids*, Dover Publications, Inc., New York, 1991.

[37] J. D. Achenbach, *Wave Propagation in Elastic Media*, Noth-Holland Publishing Company, 1984.

[38] Arthur L. Leissa, *Vibration of Plates*, NASA SP-160, Washington, D.C., pp 1 - 2 , 1969.

[39] L. Cremer and M. Heckl, *Structure-Borne Sound*, Springer-Verlag, Second Edition, pp 502 - 505, 1988.

[40] Clarence S. Clay and Herman Medwin, *Acoustical Oceanography*, John Wiley & Sons, pp 184 - 194, 1977.

[41] A. Ben-Menahem and S. J. Singh, *Seismic Waves and Sources*, Springer-Verlag, New York, pp 347, 1981.

[42] K. von der Heydt, N. R. Galbraith, A. B. Baggeroer, R. Muench, P. S. Guest and K. L. Davidson, "CEAREX A - Camp : Navigation, Bathymetry, CTD, Meteorlogy, and LOFAR Data Report", WHOI technical memorandum, January 24, 1991.

[43] John J. Polcari, "Acoustic Mode Coherence in the Arctic Ocean", Ph.D. thesis, WHOI-MIT Joint Program, May 1986.

[44] Private communication with Tom Hayward of NRL, Washington DC., June 1993.

[45] J. Wakeley, Jr., "Coherent ray tracing - measured and predicted shallow-water frequency spectrum", *J. Acoust. Soc. America*, **63**(6), pp. 1820 - 1823, 1978.

[46] Alan V. Openheim and Ronald W. Schafer, *Discrete-Time Signal Processing*, Prentice-Hall, pp 101 - 112, 1989.

[47] T. J. Hayward, T. C. Yang, "Low-frequency Arctic reverberation. I: Measurement of under-ice backscattering strengths from short-range direct returns", *J. Acoust. Soc. America*, **93**(5), 2517 - 2523, 1993.

[48] T. Kapoor and H. Schmidt, "Matched field estimation of scattering from arctic Ice - analysis of the CEAREX 89 field experiments", *J. Acoust. Soc. America*, **93**, 2419 (A), 1993.

[49] A. B. Baggeroer, W. A. Kuperman and H. Schmidt, "Matched field processing : Source localization in correlated noise as an optimum parameter estimation problem", *J. Acoust. Soc. America*, **83**(2), 571 - 587, 1988.

[50] A. B. Baggeroer, Geophysical and Oceanographic Signal Processing II, Class notes, MIT, Spring 1993.

[51] N. R. Chapman, "Source levels of shallow explosive charges", *J. Acoust. Soc. America*, **84**(2), 697 - 702, 1988.

[52] A. P. Dowling and J. E. Ffowcs Williams, *Sound and Sources of Sound*, John Wiley & Sons, pp 171 - 173, 1983.

[53] Finn B. Jensen, William A. Kuperman, Michael B. Porter, and Henrik Schmidt, *Computational Ocean Acoustics*, American Institute of Physics, pp 465 - 470, 1994.

[54] Chil Sung Park, "Three-dimensional acoustic radiation fields from a spherically layered shell submerged in an infinite fluid medium", Ph.D. thesis, MIT, September 1989.

[55] A. G. Pathak and P. R. Stepanishen, "Acoustic harmonic radiation from fluid-loaded spherical shells using elasticity theory", *J. Acoust. Soc. America*, **96**(4), 2564 - 2575, 1994.

[56] George Arfken, *Mathematical Methods for Physicists*, Academic Press, Inc., pp 666 - 683, 1985.

[57] Henry Margenau and George M. Murphy, *The Mathematics of Physics and Chemistry*, D. Van Nostrand Co., Inc., pp 109 - 113, 1964.

[58] M. Abramowitz and I. A. Stegun, *Handbook of Mathematical Functions*, Dover Publications, Inc., New York, 1970.

[59] A. Cemal Eringen and E. S. Suhubi, *Elastodynamics : Linear Theory*, Volume II, Academic Press, pp 804 - 836, 1975.

[60] David C. Ricks, "Elastodynamic modeling of fluid-loaded cylindrical shells with multiple layers and internal attachments", Ph.D. thesis, MIT, May 1994.